UNIVERSITY OF SOUTHAMPTON

FACULTY OF PHYSICAL AND APPLIED SCIENCES

Physics

Interactions in optically imprinted polariton lattices

by

Matteo Silva

Supervisor: Prof. Pavlos G. Lagoudakis

Thesis for the degree of Doctor of Philosophy

October 2017

Declaration of Authorship

I, Matteo Silva, declare that the thesis entitled *Interactions in optically imprinted polariton lattices* and the work presented in the thesis are both my own, and have been generated by me as the result of my own original research. I confirm that:

- this work was done wholly or mainly while in candidature for a research degree at this University;
- where any part of this thesis has previously been submitted for a degree or any other qualification at this University or any other institution, this has been clearly stated;
- where I have consulted the published work of others, this is always clearly attributed;
- where I have quoted from the work of others, the source is always given. With the exception of such quotations, this thesis is entirely my own work;
- I have acknowledged all main sources of help;
- where the thesis is based on work done by myself jointly with others, I have made clear exactly what was done by others and what I have contributed myself;
- parts of this work have been published as: [1], [2], [3], [4] and [5]

Signed:.....

Date:.....

Publications

- Polariton Condensation in a Strain-Compensated Planar Microcavity with InGaAs Quantum Wells.
  P. Cilibrizzi, A. Askitopoulos, M.Silva, F. Bastiman, E. Clarke, J.M. Zajac, W. Langbein and P.G. Lagoudakis - *Applied Physics Letter* **105**, 191118 (2014)

- Realizing the Classical XY Hamiltonian in Polariton Simulators.
  N.G. Berloff, M. Silva, K. Kalinin, A. Askitopoulos, J.D. Töpfer, P. Cilibrizzi, W. Langbein and P.G. Lagoudakis - *Nature Materials* accepted (2017)

- Heisenber Exchange Coupling in a Polariton Dyad.
  M. Silva, K. Kalinin, P. Cilibrizzi, A. Askitopoulos, W. Langbein, N.G. Berloff and P.G. Lagoudakis - in preparation

- Giant Vortex of Controlled Multiplicity in Polariton Lattices.
  K. Kalinin, M. Silva, J.D. Töpfer, W. Langbein, N.G. Berloff and P.G. Lagoudakis - *Nature Communications* under review

- Spin Coupling in a Polariton Dyad.
  J.D. Töpfer, M. Silva, K. Kalinin, W. Langbein, N.G. Berloff and P.G. Lagoudakis - in preparation

"If you think you understand quantum mechanics,
you don't understand quantum mechanics."

Richard P. Feynman

UNIVERSITY OF SOUTHAMPTON

ABSTRACT

FACULTY OF PHYSICAL AND APPLIED SCIENCES
Physics

Doctor of Philosophy

INTERACTIONS IN OPTICALLY IMPRINTED POLARITON LATTICES

by Matteo Silva

Microcavity exciton-polaritons results from the admixture of cavity photons and excitons in the strong coupling regime. Due to their hybrid nature, polaritons are a promising solid-state platform for both fundamental studies on light-matter interaction and applications in quantum and opto-electronics technologies. In this thesis, optically imprinted graphs of interacting polariton condensates are proposed and demonstrated to simulate universal spin models whose ground state brings about the solution of a bespoken optimisation task. The establishment, control and tailoring of a complex network of interactions across the graphs' nodes is an essential ingredient to map complex optimisation tasks to a polariton graph. Here, a method is proposed to quantify and measure coupling strength between a pair of polariton condensates as a function of their physical separation. Furthermore, this thesis also outlines how the coupling is influenced by optically injecting a non-homogeneously polarised polariton graph.

Acknowledgements

First, thanks to Pavlos who gave me the possibility to join his group enabling to study the fascinating world of polaritons. As a supervisor, he encouraged and supported my research activity.

Thanks to Paco who taught me how to be a good experimentalist with its patience, help and its favourite rule:*"use as less optical components as you can"*, a sort of Occam razor for experimental physicist. Thanks to Alexis who taught me how to master Ti:Sapphire lasers and helped with fruitful discussions. Thanks to Lucy for reading my thesis finding too many typos. A special thanks to Julian and Giacomo with whom I shared most of my best coffee breaks. In particular, thanks Giacomo just to be around while I was writing my thesis and thanks to Julian who shared one year with me in the lab always being very motivated, deeply interested in our joint research project and an immense source of discussion and further understanding. Thank to my colleagues and all people I met in Southampton with whom I shared my PhD time. Thanks to Tom and Justin for running and keeping alive the helium liquefier until my last measurements, essential for any result I achieved. A special mention to Francesco for all the time we spent together playing chess in the office and to Elena for the support and help during the hardest time of my PhD and not only.

A big thank to Viviana who brightened up my life and supported during the hardest time of my PhD.

Lastly, a big thanks to my family who supported me throughout my journey.

Contents

List of Figures

List of Tables

List of Abbrevations

MC	Micro-Cavity
QW	Quantum well
DBR	Distributed Bragg reflector
GaAs	Gallium Arsenide
AlAs	Aluminium Arsenide
AlGaAs	Aluminium Gallium Arsenide
InGaAs	Indium Gallium Arsenide
LP	Lower Polariton
UP	Upper Polariton
C	Cavity photon
X	Exciton
NA	Numerical Aperture
FSR	Free Spectral Range
BP	BandPass
R	Reflectivity
FWHM	Full-Width Half Maximum
PL	PhotoLuminescence
FP	Fabry-Perot
SLM	Spatial Light Modulator
LC	Liquid Crystal
TN	Twisted Nematic
PAN	Parallel Alignment Nematic
IFTA	Iterative Fourier Transform Algorithm
GS	Gerchburg-Saxton
MRAF	Mixed Region Amplitude Freedom
BEC	Bose Einstein Condensation
LRO	Long-Range Order
ODLRO	Off-Diagonal Long-Range Order
QV	Quantised Vortex
DVS	Discrete Vortex Soliton
cGLE	Complex Ginzburg-Landau Equation

Chapter 1

Introduction

In the last decades, the development of semiconductor technologies has begun a worldwide revolution encompassing almost every aspect of life, i.e. medicine, sustainable energy and telecommunication. The success of semiconductors lies in the flexibility of their properties and the development of unprecedented sophisticated growth techniques which determines the establishment of silicon as the most widely spread material for electronics components and the development of new compact, efficient and tunable light sources and detectors based on III-V semiconductor alloys. In particular, vertical-cavity surface emitting lasers (VCSELs) has been demonstrated to offer a cheap and low-consumption single-mode laser source for photonics application [6].

Afterwards, the crossover from the weak to the strong coupling regime has been observed in VCSEL-like devices due to the subsequent improvement of growth techniques [7]. In a strong coupled microcavity, the light and matter eigenstates hybridises forming a new bosonic quasi-particles named polaritons [8]. Due to their mixed nature, i.e. half-light half-matter, polaritons inherit their properties from their components. In particular, from the photonic component they inherit a very light mass which is about 10^{-5} times the mass of the free electron and a finite lifetime in the range of $1 \div 100\,ps$, while from the excitonic component the tendency to interact each other at high densities. In particular, polaritons are expected to exhibit macroscopic quantum phenomena at elevated temperature due to their large De Broglie wavelength. Therefore, a much effort has been put into research polariton systems culminated in several striking achievements as, among others, polariton condensation at cryogenic [9] and up to room temperature [10], electrically injected invertion-less polariton laser [11], Josephson oscillations [12] and superfluidity [13].

Recently, a new coupling mechanism has been introduced to described the phase correlation between spatially separated and freely expanding polariton condensates, hereafter referred to as polariton graphs [14]. In this context, polariton condensation is driven into the phase configuration with the highest occupancy due to the bosonic character

of the condensation phenomenon. In the work presented in this thesis, polariton graphs are proposed and demonstrated as a platform for simulating universal spin models [2]. It is known that many intractable optimisation tasks can be mapped to analogue spin systems with a bespoken and sufficiently complex coupling network across spins. Previous works on optically imprinted polariton graphs have demonstrated how the coupling sign can be tuned by means of the graph geometry and/or excitation power but only in regular structure [14, 15]. On this basis, this work also aims to present several methods to engineer complex coupling network.

Chapter 2 begins with an introduction of the physics of microcavity exciton-polaritons and their constituents. Afterwards, the concept of Bose-Einstein condensation is presented with emphasis to its applicability on polariton systems. Eventually, the concept of polariton condensation is discussed alongside its experimental evidences and theoretical description. Chapter 3 describes the experimental techniques to excite and characterise polariton graphs in microcavities. In particular, I describe the techniques to shape the spatial and polarisation excitation profile. The final section is dedicated to discuss the novelty of the sample used throughout my thesis, while chapter 4 presents the first observation of polariton condensation in a strain-compensated microcavity in that sample. In chapter 5, I address how polariton graphs can simulate the classical XY model describing both the theoretical foundation and experimental realisation. In chapter 6, I discuss another application of polariton graphs presenting the preliminary results about the observation of stable, irrotational, spontaneous and multiple-charged quantised vortices in polariton polygons. In chapter 7, I discuss a method to measure and quantify the coupling strength across a pair of condensates and I illustrate how polariton spin may lead to further engineer the coupling network in a polariton graph. Eventually, chapter 8 summaries the main conclusions of this thesis and future prospectives.

Chapter 2

Microcavity exciton-polaritons

In the first part of the chapter, the physics of microcavity (exciton-)polaritons is presented. The chapter starts from the concept of photon and exciton confinement in semiconductor heterostructures (sections 2.1.1 and 2.1.2) and continues with the description of two distinct regimes occurring in polariton microcavities, namely, the strong and weak coupling regime (section 2.1.3). I conclude the section discussing polariton spin (section 2.1.3.1) and excitation and relaxation mechanism of polariton (section 2.1.4).

The second part of the chapter is dedicated to the discussion of the concept of Bose-Einstein condensation (BEC). Firstly, I discuss the case of an ideal gas of bosons (section 2.2.1) and, afterwards, I extend the definition of standard BEC to take into account particle interaction and non-equilibrium cases 2.2.2. Then, I conclude discussing systems with reduced dimensionality (section 2.2.3).

In the last section, I introduce the concept of polariton condensation (section 2.3), the experimental evidences (section 2.3.1) and its theoretical description (section 2.3.2).

2.1 Semiconductor microcavities and quantum wells

2.1.1 Cavity photons

A microcavity (MC) is an optical resonator confining light in a region whose size is of the order of its wavelength. Depending on material and application, several structures were developed enabling confinement in one or more dimensions with a vast variety of choice concerning the resonator geometry [16]. For the purpose of this thesis, I focus the discussion on Fabry-Perot resonators which is composed by two parallel mirrors providing light confinement in one dimension. Usually, distributed Bragg reflectors (DBRs), a sequence of layers of alternating materials, are preferred in respect to metallic mirror because reflectivity spectrum can be tailored by changing the number of layers

pair and the index contrast, while the central wavelength can be tuned on demand by adjusting the optical thickness of each layer[8].

Figure 2.1 shows a schematic DBR structure and its corresponding reflectivity spectrum calculated using the transfer matrix method. The DBR is made of 20 pairs of alternating materials whose thickness is $d_i = \lambda_0/4n_i$ with λ_0 the central wavelength of the stop-band and n_i the refractive indices of the two materials.

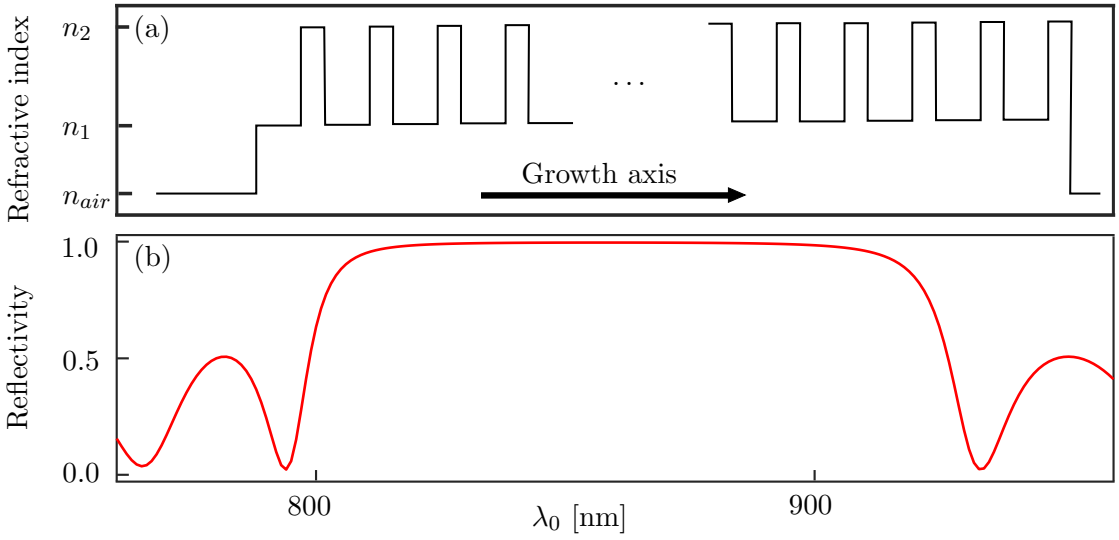

Figure 2.1: (a) Refractive index profile along the growth axis of a 20 pairs DBR centred at 858 nm. (b) Corresponding reflectivity spectrum at normal incidence showing a stop-band around the chosen central wavelength.

A cavity layer whose thickness is multiple of $\lambda_0/2$ sandwiched between two DBRs centred at λ_0 is the simplest configuration to design a planar MC as shown in Figure 2.2(a). A $\lambda_0/2$ layer can be described as a defect layer which breaks the alternating rule defining a DBR. Therefore, in a similar fashion as a crystallography defect may create a state inside the band structure gap, the cavity layer generates an allowed transmitted photonic mode in the centre of the stop-band 2.2(b).

For high reflectivity structures whose residual absorption is negligible, $R \sim 1$ in the stop-band, the condition for such Fabry-Perot longitudinal mode is given as [8]

$$k_z L_c = j\pi \tag{2.1}$$

where L_c is the cavity length, k_z is the wavevector along the growth axis and j is an integer number. Microcavity resonator differs from conventional resonator because the cavity length is of the order of the wavelength of the confined mode, so that a MC is characterised by a single longitudinal mode within its whole stop-band. It is worth noting that, contrary to metallic mirrors, the penetration depth of the cavity field inside DBRs is not negligible. Therefore, L_c in equation 2.1 needs to be replaced by the effective

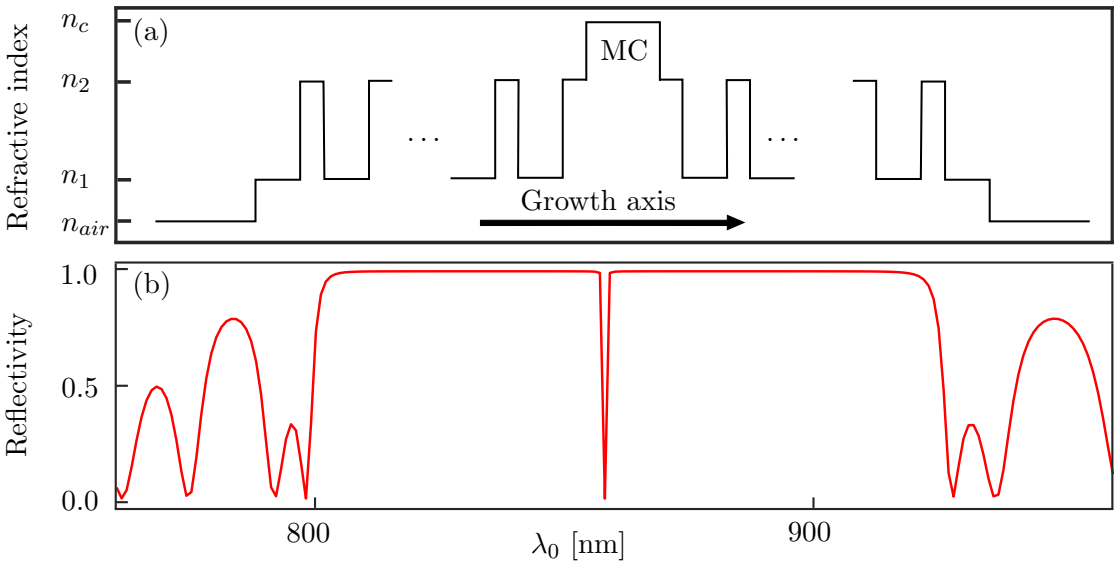

Figure 2.2: (a) Refractive index profile along the growth axis of $\lambda_0/2$ MC sandwiched between two 20 pairs DBRs centred at 858 nm. (b) Corresponding reflectivity spectrum at normal incidence showing a dip in the centre of the stop-band which corresponds to the cavity mode.

cavity length, L_{eff}, which takes into account the spatial extension of the cavity field inside both DBRs.

Equation 2.1 represents a quantisation rule for k_z for a given cavity length, while the in-plane wavevector is a continuous variable due to the continuous translational symmetry of an ideal planar microcavity. As a consequence of the quantisation of k_z the MC photon is characterised by a parabolic dispersion at low in-plane wavevector (Eq. 2.2) and it acquires a mass, $m = \hbar\pi/cL_{eff}$, which is usually about 5 orders of magnitude lighter than an electron.

$$E = \hbar ck = \hbar c\sqrt{k_z^2 + k_{\parallel}^2} \sim \hbar c\,(k_z + k_{\parallel}^2/2k_z) \tag{2.2}$$

where $\hbar$ is the reduced Planck constant and $k_{\parallel}$ is the in-plane wave-vector of the cavity mode.

2.1.2 Quantum well excitons

An exciton, a bound state of an electron and a hole attracted by electrostatic Coulomb force, is a quantum of electronic excitation energy travelling in the periodic structure of a crystal; it is electrically neutral and hence its movement through the crystal gives rise to the transportation of energy but not charge [17]. Excitons are usually classified into two classes: the Frenkel exciton [18] and the Wannier-Mott exciton [19, 20]. The Frenkel exciton describes solids where the interaction between electrons from neighbouring atoms

is small compared with the forces holding the electrons within individual atoms, resulting in a high binging energy, up to $1\,eV$, and in few unit cells extention. Wannier-Mott exciton describes the opposite behaviour and are characterised by a weak binding energy, few meVs, and a spatial extension of tens of lattice constants. From now on, I restrict the discussion to Wannier-Mott excitons since the work of this thesis was done on a GaAs-based sample.

Exciton is a hydrogen-like bound state. Therefore, its binding energy, E_X, and Bohr radius, a_B, can be calculated from the solution of the Schrödinger equation for an hydrogen atom [21, 22] and they read

$$\begin{aligned} E_X &= \frac{\pi^2 m e^4}{4\hbar^2 \epsilon_0^2 \epsilon_r^2} \\ a_B &= \frac{4\pi\epsilon_0\epsilon_r\hbar}{me^2} \end{aligned} \tag{2.3}$$

where m is the reduced mass of the system, ϵ_0 is the vacuum permittivity, ϵ_r is the dielectric constant of the material and e is the electron charge. For the hydrogen atom, where the reduced mass is the electron mass and the dielectric constant is unitary, the binding energy and the atom size are $13.6\,eV$ and 0.529Å. On the other hand, inorganic semiconductor are usually characterised by a dielectric constant one order of magnitude larger and by an exciton reduced mass one order of magnitude lower than the hydrogen atom. Therefore, the typical binding energy is of the order of few meV, while the exciton size spans about tens of lattice constants.

Exciton properties are dramatically modified due to quantum confinement effect when exciton is confined in a region comparable to its diameter in bulk[23]. For the purpose of this thesis, I discuss only the case of confinement in one direction which can be achieved by sandwiching a low energy-gap semiconductor between two layers of a high energy-gap one, the so-called quantum well (QW), as shown in Figure 2.3.

The energy-gap alignment of such heterostructure enables to confined both electrons and holes in the central layer which acts as a 1D potential well along the growth axis. By standard quantum mechanics calculation, it can be shown that the 1D confinement leads to (1) a renormalised energy-gap of the QW material, (2) a quantisation of the exciton motion along the growth axis, (3) an increase of the exciton binding energy and (4) a reduction of its Bohr radius mainly depending on QW thickness [8], as it is shown

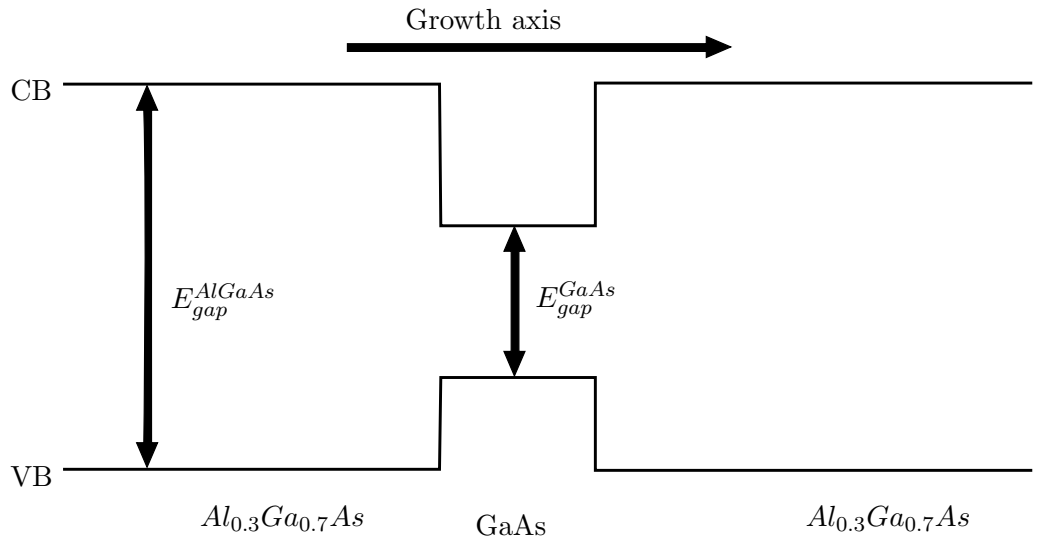

Figure 2.3: Schematic representation of the bulk valence and conduction band (VB and CB) along the growth axis of a $GaAs$ QW embedded between two $Al_{0.3}Ga_{0.7}$ bulk layers. Since the qwerty CB (VB) lies below (above) the corresponding band of the high energy-gap material, both electrons and holes can be trapped in the QW layer.

in equation 2.4 for the case of a barrier of infinite height.

$$\begin{aligned} E_{gap}^{2D} &= E_{gap} + E_C - E_X^{2D} \\ E_C &= \frac{\hbar^2 \pi^2}{2mL^2} \\ k_z L &= j\pi \\ E_X^{2D} &= 4E_X \\ a_B^{2D} &= \frac{a_B}{2} \end{aligned} \tag{2.4}$$

where E_{gap} is the energy-gap of the bulk material, E_{gap}^{2D} is the energy-gap of the corresponding QW, E_C is the quantum confinement energy, E_X^{2D} and a_B^{2D} are the QW exciton binding energy and Bohr radius, k_z is the exciton wavevector along the growth axis, j is a positive integer and L is the QW thickness.

It is worth noticing that the QW exciton dispersion in the QW plane remains parabolic and that light and heavy QW excitons are no longer degenerate at $k_{\|} = 0$ in a QW as the confinement energy depends on the reduced mass of the exciton.

In essence, exciton's constituents in a QW are closer together than in bulk semiconductor due to quantum confinement effect and, therefore, their attractive interaction is enhanced. The exciton effect in bulk inorganic semiconductor at room temperature is usually small because excitons are mainly dissociated as the thermal energy, $E_T = k_b T$ with k_b the Boltzmann constant and T the absolute temperature, is greater than the exciton binding energy, E_X. On the other hand, excitonic effects are enhanced in QW and

can be observed also at room temperature, whereas they are usually observed only at low temperatures in bulk semiconductors [24]. Furthermore, due to the spatial compression of an exciton in a QW, its oscillator strength, which is a measure of the probability and emission of photons, is well known to be greatly increased in QW excitons compared to bulk excitons [25, 26].

In a more realistic model, the Shcrödinger equation should be solved for the case of a particle confined in a finite potential well. The main difference between the two models is represented by the fact that, while in a infinite well the walls are impenetrable, in other words the wavefunction is zero outside the well material, in a finite well the wavefunction decays exponentially in the barriers. As a consequence, the number of bound-states is limited and their energies are smaller than those of the infinite well [23]. However, both models qualitatively agree on the consequences of the quantum confinement previously discussed.

As excitons are composite of two fermions, a natural question arises whether they can be treated as bosons and under which conditions. Accordingly to the second quantisation formalism, excitons are true bosons when their creation and annihilation operators, $X(\mathbf{k}_\parallel)$ and $X^\dagger(\mathbf{k}_\parallel)$, satisfy the relation

$$[X(\mathbf{k}_\parallel), \mathbf{X}^\dagger(\mathbf{k}'_\parallel)] = \delta(\mathbf{k}_\parallel - \mathbf{k}'_\parallel)) \tag{2.5}$$

It can be shown that $[X(\mathbf{0}), X^\dagger(\mathbf{0})] = 1 - O\left(n_X (a_B^{2D})^2\right)$ where n_X is the exciton density [8]. Therefore, excitons can be safely treated as true boson in the limit $n_X (a_B^{2D})^2 \ll 1$.

2.1.3 Polaritons

A polariton is a quasi-particle describing the *strong coupling* between a light excitation and a matter one. Here after, I refer to the bosonic quasi-particles from the strong coupling MC photons and QW excitons as polaritons. Due to their mixed nature, i.e. half-light half-matter, polaritons inherit properties from both components. In particular, from the photonic component they inherit a very light mass which is about 10^{-5} times the mass of the free electron (table 2.1), while from the excitonic component the tendency to interact each other at high densities. As I will discuss in section 2.1.3.1, polaritons carry an integer spin which is also determined by their constituents. Due to conservation laws, polaritons properties are experimentally easily accessible with well established optical techniques by measuring the photons leaking outside the MC. Another advantage of polaritons is that, contrary to QW excitons, they are almost unaffected by QW disorder in realistic systems [27].

The most common structure to study polariton is made of a MC with embedded QWs. Usually, QWs are placed at the antinodes of the cavity field to maximise the light-matter coupling [28], as shown in figure 2.4.

Table 2.1: Physical properties of the polaritons compared with excitons and atomic gases as reported in reference [28]. Here, m_0 is the free electron mass.

System	Effective mass [m_0]	Bohr radius [Å]	Lifetime
Polaritons	10^{-5}	10^{2}	$1 \div 100\,ps$
Excitons	10^{-1}	10^{2}	$1\,ns$
Atomic gases	10^{3}	10^{-1}	$1\,s$

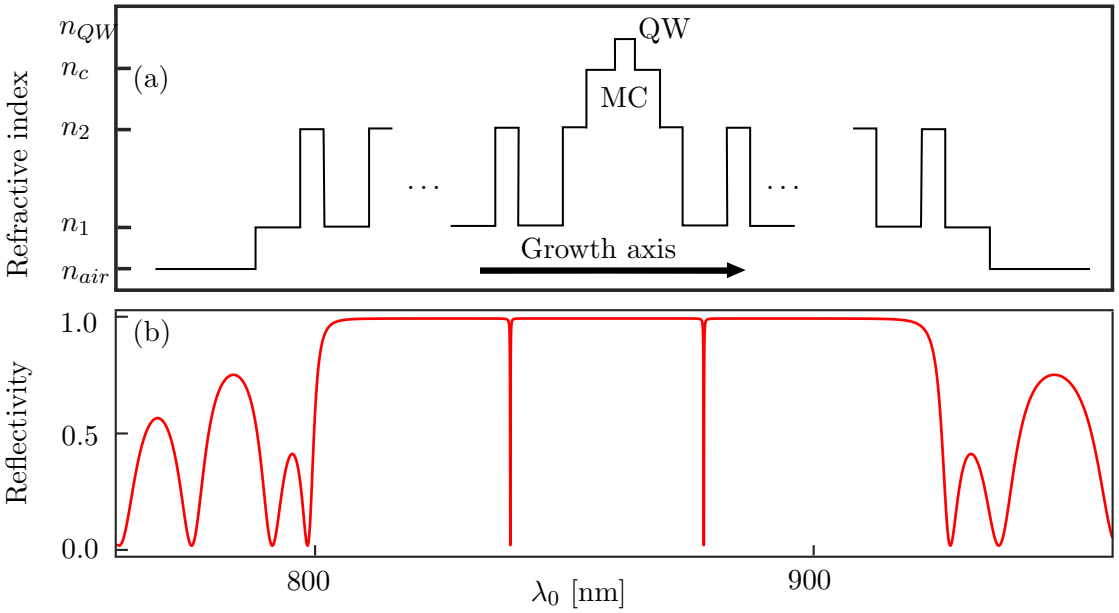

Figure 2.4: (a) Refractive index profile along the growth axis of λ_0 MC sandwiched between two 20 pairs DBRs centred at 858 nm. A WQ is placed at the centre of the structure whose exciton energy is resonant with the cavity field. (b) Corresponding reflectivity spectrum in the strong coupling regime at normal incidence showing a doubled peak centred around of the chosen central wavelength.

By tuning the growth conditions, the energies of the photonic and excitonic modes can be set close to resonance to obtain a significant interaction between the two modes [29]. The interaction is physically originated to the first order by the coupling between the exciton dipole moment, $\mathbf{d}$, and the cavity field, $\mathbf{E}$, and it is characterised by an energy transfer of $E = \mathbf{d} \cdot \mathbf{E}$. The system is said to be in the strong coupling regime when the energy exchange rate, $\Omega = E/\hbar$, is faster than the decay rates of both modes, γ_X and γ_c [30]. In this regime, the spontaneous emission process becomes reversible, in other words photons are absorbed and emitted by the excitons several times before leaving the cavity, resulting in a coherent oscillation of the excitation energy between the two modes as described in the Rabi model. The observation of two modes split around the exciton resonance is universally recognised as the fingerprint of such regime and their energy separation, the so-called *vacuum Rabi splitting*, evaluates the strength of the light-matter coupling in the system, as shown in figure 2.4. The Rabi splitting defines

each polariton system and, depending on the material, it ranges from a few meV in GaAs structures to tens/hundreds of meV in high band-gap semiconductor, i.e. GaN, ZnO and organic materials.

The Rabi splitting in this type of structure was first observed in the reflectivity spectrum of a high-quality GaAs-based structure by Weisbuch and co-authors [7]. In their work, the authors enlightened that the Rabi splitting appears simultaneously with an *anti-crossing* behaviour of the polariton modes, as shown in figure 2.5, when the cavity mode is scanned across the exciton resonance.

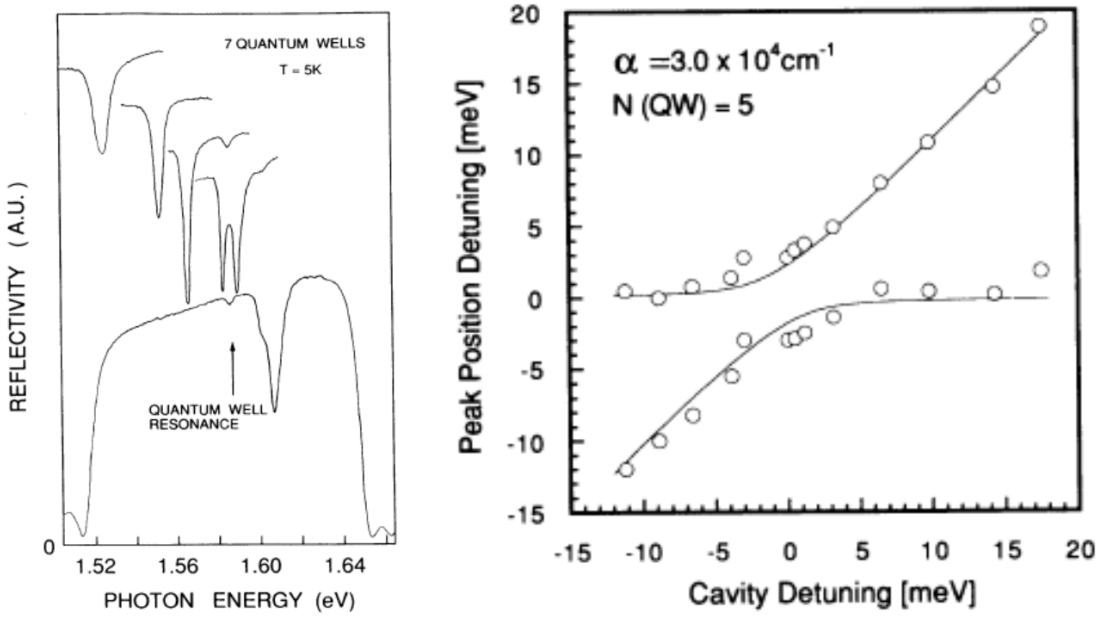

Figure 2.5: Left: Experimental reflectivity at different detuning showing the resonance mode splitting at the resonant energy of $1.605\,eV$. Right: Reflectivity peak energies as a function of the detuning showing the anti-crossing behaviour of the two polariton modes. Figures taken from reference [7]

Within the framework of the second quantisation, the Hamiltonian for uncoupled excitons and photons neglecting decay terms reads

$$H_{free} = \sum_{k_\parallel} E_x(k_\parallel) X_{k_\parallel} X^\dagger_{k_\parallel} + \sum_{k_\parallel} E_c(k_\parallel) C_{k_\parallel} C^\dagger_{k_\parallel} \tag{2.6}$$

where $E_c(k_\parallel)$, $E_X(k_\parallel)$ are the photon and exciton energy respectively, $C_{k_\parallel}$, $X_{k_\parallel}$ ($C^\dagger_{k_\parallel}$, $X^\dagger_{k_\parallel}$) are the annihilation (creator) operators for cavity photons and excitons respectively. In this representation, the interaction Hamiltonian is

$$H_{int} = \sum_{k_\parallel} \hbar\Omega \left(X^\dagger_{k_\parallel} C_{k_\parallel} + X_{k_\parallel} C^\dagger_{k_\parallel} \right) \tag{2.7}$$

For a given $k_\parallel$, the new eigenenergies and eigenstates of the system, the so-called *lower polariton* (LP) and *upper polariton* (UP), are calculated by diagonalisation of the full Hamiltonian, $H_{full} = H_{free} + H_{int}$:

$$\begin{aligned}
E_{UP,LP}(k_\parallel) &= \frac{1}{2}\left(E_c(k_\parallel) + E_x(k_\parallel) \pm \sqrt{(E_c(k_\parallel) - E_x(k_\parallel))^2 + 4\hbar^2\Omega^2}\right) \\
|LP\rangle &= c_{k_\parallel}\,|C_{k_\parallel}\rangle - \chi_{k_\parallel}\,|X_{k_\parallel}\rangle \\
|UP\rangle &= \chi_{k_\parallel}\,|C_{k_\parallel}\rangle + c_{k_\parallel}\,|X_{k_\parallel}\rangle \\
|c_{k_\parallel}|^2 &= \frac{E_{UP}(k_\parallel)E_X(k_\parallel) - E_{LP}(k_\parallel)E_C(k_\parallel)}{(E_C(k_\parallel) + E_X(k_\parallel))\sqrt{(E_C(k_\parallel) - E_X(k_\parallel))^2 + 4\hbar^2\Omega^2}} \\
|\chi_{k_\parallel}|^2 &= \frac{E_{UP}(k_\parallel)E_C(k_\parallel) - E_{LP}(k_\parallel)E_X(k_\parallel)}{(E_C(k_\parallel) + E_X(k_\parallel))\sqrt{(E_C(k_\parallel) - E_X(k_\parallel))^2 + 4\hbar^2\Omega^2}}
\end{aligned} \tag{2.8}$$

where $|LP\rangle$ and $|UP\rangle$ are the eigenstates of the coupled system, $E_{LP}(k_\parallel)$ and $E_{UP}(k_\parallel)$ are the corresponding energies. The coefficients $c_{k_\parallel}$ and $\chi_{k_\parallel}$ represents the *Hopfield coefficients* [31] and satisfy the normalisation condition $c_{k_\parallel}^2 + \chi_{k_\parallel}^2 = 1$. Moreover, their squared norms represents the photonic and excitonic fraction of each polariton mode.

For a fix detuning, $\delta = E_c(0) - E_X(0)$, equation 2.8 enables to calculate both the dispersion relation and the Hopfield coefficients for the LP and UP polariton branches, as shown in figure 2.6.

Taking into account the photon decay rate, γ_c, and the non-radiative broadening of the exciton, γ_X, equation 2.8 becomes [32]:

$$E_{UP,LP} = \frac{1}{2}\left(E_c + E_x - i\hbar(\gamma_X + \gamma_c) \pm \sqrt{(E_c - E_x - i\hbar(\gamma_X - \gamma_c))^2 + 4\hbar^2\Omega^2}\right) \tag{2.9}$$

At zero detuning, the square root is purely imaginary when $2\Omega > \gamma_c - \gamma_X$ which means that the system is in the so-called *weak-coupling* regime where exciton and photon energies remain unperturbed and the decay rates are enhanced.

2.1.3.1 Polariton spin

Polaritons are bosons in the low density regime and, as such, have an integer spin which is determined by its constituents, the QW exciton and the MC photon. In the same way, exciton spin is determined by its building blocks. In zinc-blend crystals such as AlGaAs and CdTe, electrons in the conduction band have S-symmetry ($l = 0$ and $s = 1/2$), while the the holes in the valence band have P-symmetry therefore featuring a six-fold degeneracy ($l = 1$ and $s = 1/2$). The spin-orbit interaction partially removes this degeneracy leading to the formation of 3 two-fold degenerate bands: the spin-split-off band ($J = 1/2$), the heavy and light hole band ($J = 3/2$). In bulk, the light and heavy hole bands are degenerate at the Γ point, but this degeneracy is removed in confined

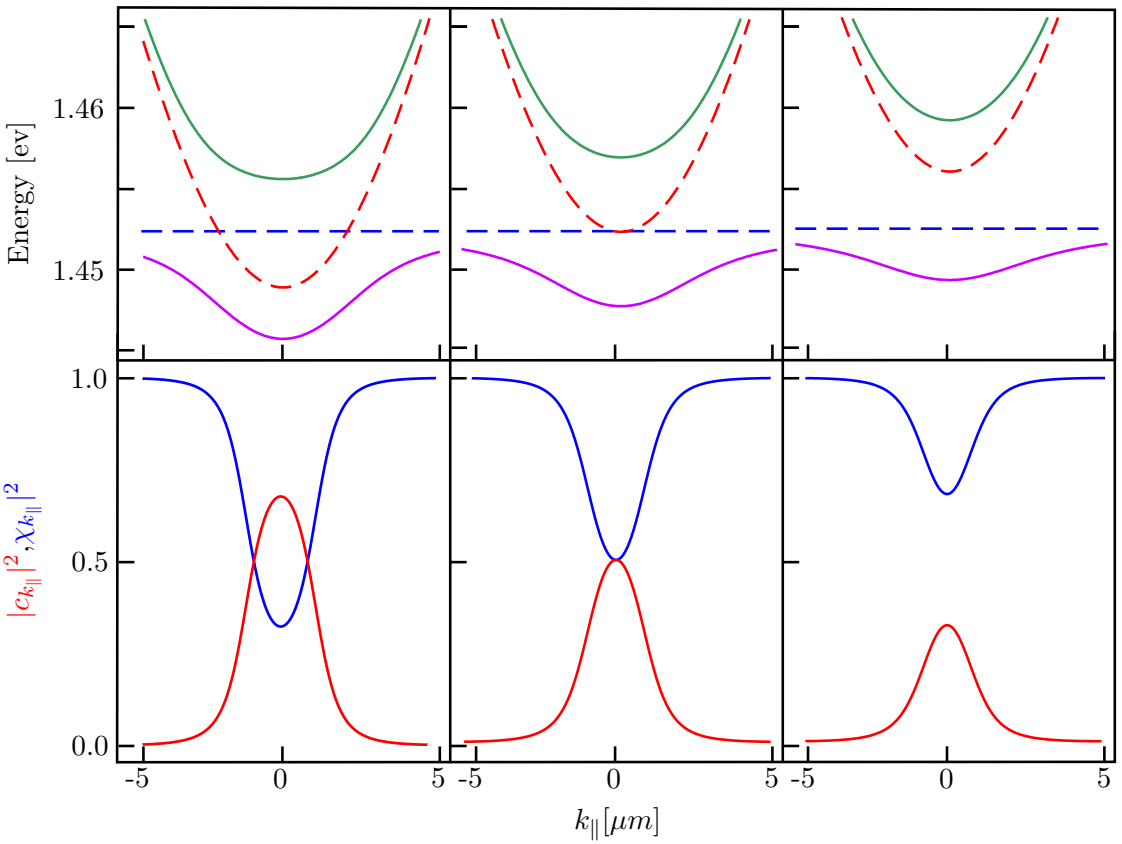

Figure 2.6: Top: Lower polariton (pink), upper polariton (green), exciton (blue) and photon (red) dispersion for negative (left), zero (centre) and positive (right) detuning. Bottom: corresponding Hopfield coefficients.

systems such as QWs due to the confinement energy (equation 2.4), as shown in figure 2.7. QW Excitons are thus composite bosons with spin of ± 1 or ± 2. Since photons carry an angular momentum of 1 with only two projection ± 1, excitons with spin ± 2 do not couple to light, while, excitons with spin of ± 1 can recombine emitting a photon of equal spin corresponding to a left or right circular polarisation. On this basis, the first excitonic states are called *dark states*, while the second ones are called *bright states*. Nevertheless, dark excitons are created whenever electrons and holes are optically excited due to spin-flip processes and their presence has a significant role in interactions with other excitons and polaritons.

2.1.4 Excitation and relaxation mechanisms

Polariton can be excited either resonantly or non-resonantly. The first case corresponds to the direct injection of polariton into the system without any intermediate process. As such, excitation energy and direction have to be properly tuned due to conservation laws. Resonant excitation scheme has the advantages to imprint polariton with the desired features and to strongly suppress the density of the exciton reservoir, but, on the other hand, polariton BEC cannot be conclusively observed under resonant excitation because

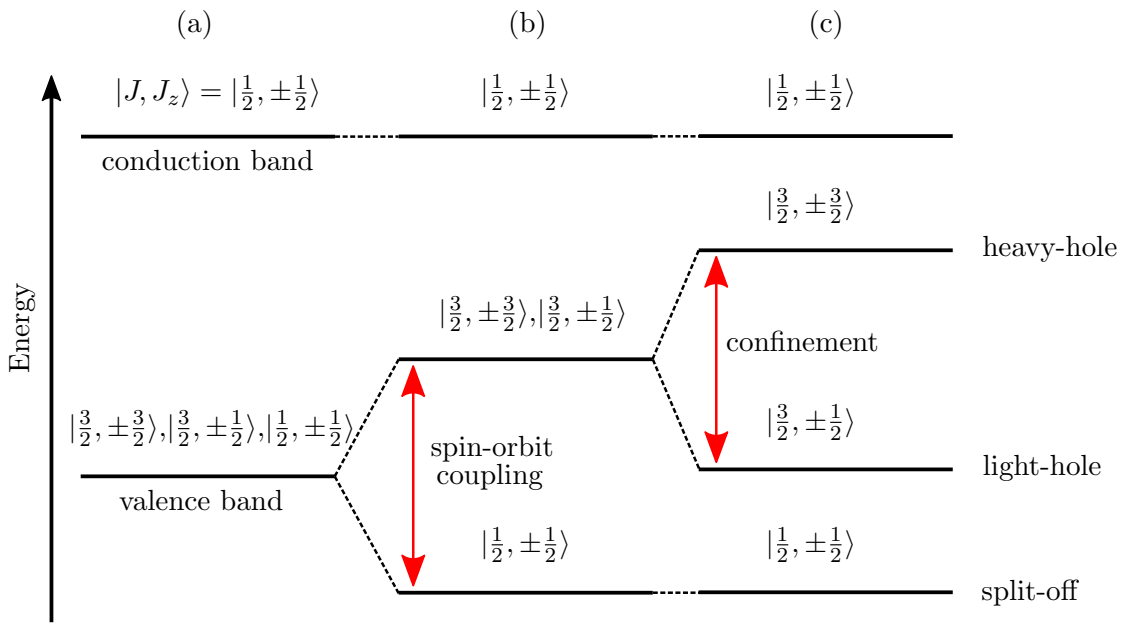

Figure 2.7: Schematic representation of electron's and hole's spin degeneracy in zinc-blend semiconductor crystals without spin-orbit coupling (a), with spin-orbit coupling (b) and with confinement potential (c). QW excitons formed by an electron and a hole of antiparallel (parallel) has $J_z = \pm 1(2)$. Due to conservation laws, only excitons with $J_z = \pm 1$ couple to circular polarised light forming the so-called *bright states*, while exciton with $J_z = \pm 2$ populate the optically inactive *dark states*.

it is not clear if the observed coherence is inherited from the excitation laser or a result of BEC.

Non-resonant excitation is realised by tuning the laser at the first minimum above the stop-band to efficiently couple light inside the MC, as shown in figure 3.10(b). This corresponds to the formation of a hot electron-hole plasma which then relax in energy to populate the polariton dispersion, as shown in figure 2.8. The relaxation process can be described in the following steps:

1. The excitation laser creates a hot electron-hole plasma in the MC and QWs above their energy gap, usually $\sim 100\, meV$ above;

2. The energy excess is transferred to the host lattice via scattering events with the emission of longitudinal optical phonons ($< 1ps$) followed by slower ($\sim 1\, ns$) acoustic phonon relaxation into high momentum exciton forming the so-called exciton reservoir. These excitons do not couple to light because their wavevector is larger than the light wavevector in the medium [33];

3. The exciton reservoir relax in energy to the high wavevector polariton dispersion through the emission of acoustic phonos. During this process, dark exciton states are also populated via spin-flip processes [34];

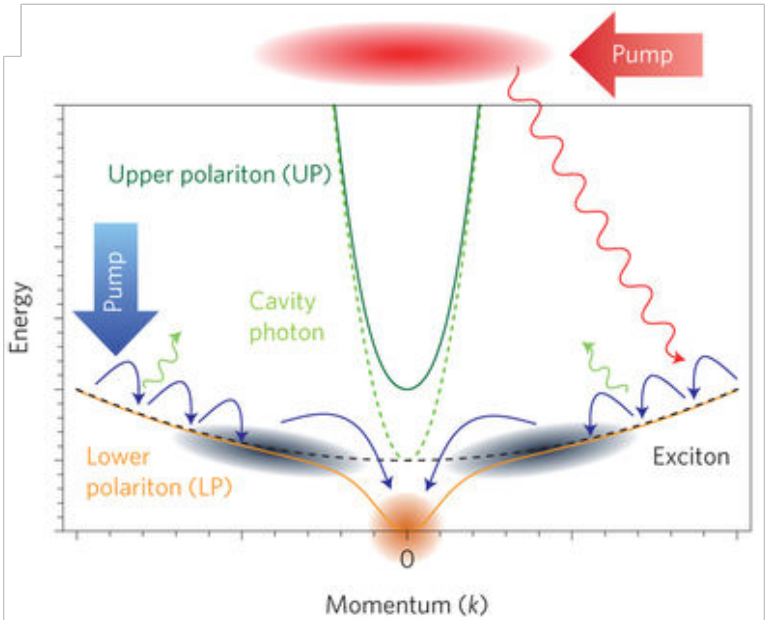

Figure 2.8: a) Schematically representation of the relaxation process under resonant (big blue arrow) and non-resonant (big red arrows) pumping scheme. High-energy excitons, generated by the pump laser, cool down via phonon emission (small blue arrows) towards the LP dispersion and accumulate in the bottleneck region (black clouds). At sufficient high density exciton-polaritons scatter into the condensate (orange cloud) via stimulated scattering. The image has been taken from reference [35].

When hot excitons enters the light cone, polariton are formed and they accumulate in a region of finite wavevector, an effect known as *bottleneck effect* [36], because the acoustic phonon-mediated process becomes more and more inefficient due to the steepness of the dispersion relation. Indeed, as polaritons relax in energy, they becomes lighter and lighter and their lifetime strongly reduces to few *ps* [35] as their photonic component increases, as shown in figure 2.6. However, at a sufficiently dense population of polaritons, polariton can overcome the bottleneck region by stimulated pair scattering [35]. In this process, two polariton of wavevector $k_{\parallel,1}$ and $k_{\parallel,2}$ scatter and result in one polariton at $k_{\parallel,0} = 0$ and another one at $k_{\parallel,3} = k_{\parallel,1} + k_{\parallel,2}$. Obviously, the corresponding scattering rate, W, is proportional to the population of the two initial states and, in addition, it is proportional to the final state occupancy due to the bosonic nature of LP:

$$W_{k_{\parallel,1},k_{\parallel,2}\to k_{\parallel,0},k_{\parallel,3}} \propto N_1 N_2 (N_0 + 1)(N_3 + 1)\, \delta(E_1 + E_2 - E_0 - E_3) \tag{2.10}$$

where E_i, N_i are respectively the energies and the populations of the corresponding i-th state with wavevector $k_{\parallel,i}$, the delta function implies energy conservation and the $+1$ terms represents the spontaneous scattering processes. Similarly to stimulated emission in conventional laser, stimulated scattering process is a phase coherent process [35]. Therefore, once the scattering rate into the ground state exceeds the decay rate, the stimulated scattering processes lead to the formation of a coherent macroscopic population of

the ground state [9]. Furthermore, the reverse of the process described in equation 2.10 is inhibited by the fast and efficient relaxation process of the high-wavevector excitons though phonon emission. As a consequence, it prevents the exciton reservoir to gain any net heat and it acts as a *thermal lock* in close analogy to the concept of *population inversion* of a conventional laser.

It is worth mentioning that, contrary to the resonant case, non-resonantly excited polariton have undergone many dephasing scattering events. Therefore, the observation of a macroscopic coherent state cannot be a reminiscence of the laser phase but it must be a signature of a phase transition showing spontaneous symmetry breaking.

All the experiments reported in this thesis have been realised under non resonant excitation.

2.2 Bose-Einstein condensation

In 1924, Bose and Einstein predicted a new state of matter, the so-called *Bose-Einstein condensate* (BEC) characterised by a macroscopic occupation of the ground state of a bosonic system [37, 38]. BEC was experimentally demonstrated for the first time in 1995 using atomic gases of rubidium [39], sodium [40] and lithium [41] at temperature of the order of nanokelvin. In this prospect, bosonic quasi-particles in solid-state systems (i.e. excitons [42] and polaritons [10, 43–48]) occupy a privileged position due to their lighter mass (table 2.1) which enables the observation of condensation using at most standard cryogenic cooling techniques.

2.2.1 Ideal gas of bosons

Particles are divided in bosons and fermions which obey, respectively, Bose-Einstein (BE) and Fermi-Dirac (FD) distribution function

$$n(E) = \frac{g_E}{e^{\frac{E(\mathbf{k})-\mu}{k_b T}} \pm 1} \tag{2.11}$$

where g_E is the state degeneracy, μ is the chemical potential[1], T the absolute temperature, k_b the Boltzmann constant, $E(\mathbf{k})$ is the energy dispersion and the minus (plus) sign is for bosonic (fermionic) particles. The distribution function has to be non-negative. Therefore, the chemical potential in a bosonic system is bounded by the ground state energy, $\mu \leq E_0$.

[1]The chemical potential can be calculated from the Helmholtz free energy Φ as $\mu = \left(\frac{\partial \Phi}{\partial N}\right)_{V,T}$ and represents the energy required to add/subtract a particle to a system at constant temperature, T, and volume, V.

The particle density of an ideal 3D gas, n, can be then calculated in the thermodynamic limit as

$$n = \lim_{V\to\infty} \frac{\sum_{\mathbf{k}} n(E)}{V} = n_0 + n_e = n_0 + \frac{2.612}{\lambda_{dB}^3} \qquad \lambda_{dB} = \sqrt{\frac{2\pi\hbar^2}{mk_bT}} \tag{2.12}$$

where n_0 is the density of the ground state, n_e is the density of the excited states and λ_{dB} is de Broglie wavelength. The density of the excited states is upper bounded by the system temperature. Therefore, a macroscopic occupation of the ground state is required to satisfy equation 2.12 when the system is cooled below a critical temperature, T_c:

$$T_c = 3.31\frac{\hbar^2}{k_b m} n^{2/3} \tag{2.13}$$

Alternatively, a particle in a gas is described by a wave packet of spatial extension of λ_{dB}. By cooling the system, λ_{dB} becomes of the order of the inter-particle distance, d, so that the wavefunctions of neighbouring atoms overlap forming an extended state with a common wavefunction [49]. On the other hand, the system enters the classical regime at high temperatures where the quantum nature of particles and the overlap of their wavefunctions become negligible. Indeed, in the high temperatures regime, the distribution functions of both fermions and bosons (equation 2.11) approach the classical Maxwell-Boltzmann one.

2.2.2 Beyond standard BEC

In the previous section, I discussed the concept of BEC for an ensemble of free particles at thermal equilibrium, but it cannot grasp the complete picture of real physical systems, usually characterised by non-vanishing interactions. Therefore, a more inclusive definition is required which is the topic of this section.

In 1956, Penrose and Onsager extended the criterium to observe BEC to interacting particles [50] and it requires that a finite fraction of particles occupy a single-particle quantum state, ψ_m. Alternatively, the appearance of *off-diagonal long range order* (ODLRO) at distances greater than λ_{dB} is a smoking gun of BEC. As ψ_m is not required to be neither the ground state nor unique, this criterium represents a generalisation of the BEC criterium for an ideal gas as well. In general, the system is named *simple* BEC when only one single-particle state is macroscopically occupied, otherwise *fragmented* BEC. However, I will neglect the fragmented BEC because polaritons are characterised by a strong repulsive inter-particle interaction which prevents fragmentation favouring simple BEC [51]. Since off-diagonal elements have no classical analogue, the ODLRO is a purely quantum effect and it is responsible for preserving the memory of the quantum phase over macroscopic distances [52]. The built up of ODLRO manifests itself in the first order spatial coherence function, $g^1(\mathbf{r_1}, t_1; \mathbf{r_2}, t_2)$, that is experimentally accessible

by means of interferometric measurements:

$$g^1(\mathbf{r_1}, t_1; \mathbf{r_2}, t_2) = \frac{\langle E^*(\mathbf{r_1}, t_1) E(\mathbf{r_2}, t_2)\rangle}{\sqrt{\langle |E(\mathbf{r_1}, t_1)|^2\rangle \langle |E(\mathbf{r_2}, t_2)|^2\rangle}} \tag{2.14}$$

where g^1 evaluates the coherence of an electromagnetic field and it ranges from 1 for a fully coherent source to 0 for a complete incoherent one.

2.2.3 2D systems, superfluidity and vorticity

An ideal gas at thermal equilibrium in an infinite and uniform 2D system does not undergo BEC because excited states does not saturates at any finite temperature [53, 54]. Furthermore, the result can be extended to the case of interacting particles. Similarly, it was shown that *long-range order* (LRO) cannot appear in 2D systems due to long-wavelength thermal fluctuations [55–58]. Remarkably, BEC phase transition is restored in 2D ideal gas trapped with a power-law potential because excitation momentum is lower bounded resulting in a reduction of phase fluctuations [59]. Furthermore, phase fluctuations vanish for a trapped interactive 2D gas [60].

Nevertheless, a weakly interacting 2D Bose gas is predicted to exhibit a superfluid phase transition at a finite temperature, T_{BKT} [58, 61]. Above T_{BKT}, the density of the superfluid component vanishes and local condensation takes place but, thermally excited free vortices prevent the formation of LRO, i.e. the correlation function decays exponentially with the distance. Below T_{BKT}, vortices organise in pairs with net zero topological charge for stability reason. As a result, different local condensation islands connect and the system exhibits quasi-LRO, i.e. the correlation function shows a power-law decay as a function of the distance.

It is worth mentioning that the superfluid phase is a peculiarity of interacting bosonic systems because free particles are characterised by a parabolic dispersion which cannot satisfy the Landau criterium for superfluidity [62]:

$$v_s < v_{cr} = min\left(\frac{E(p)}{p}\right) \longleftrightarrow \text{superfluidity} \tag{2.15}$$

where v_s is the fluid velocity with respect to a stationary object. If the fluid velocity is slower than the critical velocity, v_{cr}, it cannot dissipate energy, $E(p)$, and, therefore, it flows without any dissipation. Free particles cannot be superfluid as the critical velocity vanishes for a parabolic dispersion. However, a repulsive interaction leads to a linearisation of the dispersion at low momenta according to Bogoliubov theory [63]. Therefore, the critical velocity is finite, $v_{cr} = \sqrt{n_0 U(0)/m}$ where n_0 is the condensate density and $U(0)$ is the Fourier transform of the interaction potential evaluated at zero momentum.

The term superfluidity refers to a frictionless flow of a liquid and it was observed for the first time in liquid ^{4}He by Kapitza [64] and Allen [65]. A few months after, the connection between superfluidity and BEC was proposed by London [66], but it remained speculative and controversial for many years. In fact, Landau proposed a two fluids model to describe ^{4}He superfluidity without any reference to BEC [62]. However, even though this relation has been later experimentally confirmed, fundamental questions still remain concerning the occupancy of the ground state. In particular, due to the strong inter-atoms interaction, the ground state occupancy does not exceed 10% even at temperature where it is predicted to reach almost 100% [67].

It can be shown that the velocity associated to the BEC motion reads [68]:

$$\mathbf{v}(\mathbf{r},t) = \frac{\hbar}{m}\nabla\phi(\mathbf{r},t) \tag{2.16}$$

where $\phi(\mathbf{r},t)$ is the condensate phase. This velocity, being the gradient of a scalar function, is irrotational and, consequently, cannot be dissipative. Therefore, the BEC motion is superfluid in any region in which the BEC wavefunction does not vanish. Furthermore, the circulation calculated around a point characterised by a zero BEC density results quantised and reads:

$$\oint_C \mathbf{v}\cdot d\mathbf{l} = 2\pi n\frac{\hbar}{m} \tag{2.17}$$

where C is a close loop around the zero density point and n is an integer number. Hence, if n is not zero, the superfluid shows a density dip with a phase winding of $2\pi n$ around it. Such circulation is called *quantised vortex* and n is referred to as *topological charge* of the vortex.

After the first observation of polariton BEC, the community has focused on the fluidic nature of polariton BEC and several effects expected in the superfluid regime have been documented, i.e. the dispersion linearisation, the suppression of the Rayleigh scattering and collective dynamic behaviour [13, 69, 70]. Furthermore, being a hallmark of superfluidity, great attention has been dedicated to the observation of quantised vortices in polariton BEC [71–73], to their formation either by polariton turbulent flow [74] or by engineering the excitation source [75–78].

In chapter 6, I will discuss preliminary results on how vortices of arbitrary multiplicity can be imprinted in a polariton system under non-resonant excitation.

2.3 Polariton condensate

The term polariton condensate is used as a broader term to encompass both polariton BEC and polariton laser which are both characterised by the appearance of spontaneous

coherence once the polariton density crosses a threshold [79].

The concept of polariton laser was introduced by Imamoglu in 1996 who proposed to realise an inversion-less laser based on polaritons [80]. A polariton laser is a coherent source of radiation driven by stimulated scattering of polaritons towards a condensate which leaks out of the microcavity by spontaneously emitting coherent photons. As such, it was a dual-sided concept: a new laser source and an example of BEC in a solid state system.

A conventional BEC exists in a thermal equilibrium system, where the particle lifetime is much longer than the relaxation time [35]. Therefore, a polariton condensate is in thermal equilibrium with its host lattice only in some limited experimental conditions [81, 82]. Due to its intrinsic non-equilibrium nature, a polariton condensate may be thought as a laser system. Furthermore, on a device perspective, its structure is exactly the same as a VCSEL and the output is coherent, monochromatic and directional. However, fundamental differences exist between polariton condensates and conventional lasers, namely no population inversion is required, the driven process is bosonic stimulated scattering and the system is in the strong coupling regime.

Personally, I agree with the terminology polariton condensate because the laser acronym explicitly refers to *stimulated emission* and because the experimental conditions to achieve thermal equilibrium of a polariton condensate are currently too limiting and do not include most of the measurements of this thesis, namely negative detuning.

Beyond the nomenclature controversy, polariton condensation refers to a unique case which differs from conventional BEC and lasers. In particular, they benefit by ultra-low operation power, the continuous optical read-out, a wide range of material choice, operation temperature up to room temperature and even the potentiality for electrical injection utilising the well-developed semiconductor technology. As such, they represent a unique and fascinating system not only for fundamental aspects, i.e. BKT theory and out of equilibrium system, but also for practical purposes, i.e. ultra-low consumption lasers and quantum technology devices.

2.3.1 Experimental evidence

According to equation 2.13, condensation can be induced either by cooling at constant density or by increasing the density at constant temperature. Polariton condensate is usually observed using the latter method as the density of polariton is easily controlled via the injection power. Indeed, the first accepted proof of polariton condensation was achieved in 2006 with the observation of a power-driven phase transition from an incoherent state to a macroscopically coherent one [9]. When the excitation power crosses a threshold value, polariton condensate manifests itself by a non linear increase in the emission, a spectral narrowing, long-range spatial coherence and a stochastic

vector polarisation. Furthermore, the observation of a population density following Bose-Einstein distribution represents the smoking gun of the phase transition. However, the latter proof is still challenging due to the inter-particles interaction and the non-equilibrium nature of conventional samples.

2.3.2 Theoretical description of polariton condensates

Polariton condensate is a phase transition characterised by a macroscopic occupation of a single quantum state. Therefore, all particles within the condensate can be described by a single macroscopic wavefunction, $\psi(\mathbf{r}, t)$, which represents the *order parameter* of the phase transition. We numerically model the evolution of the order parameter using the complex Ginzburg-Landau equation and a rate equation for the exciton reservoir [83, 84]:

$$\begin{aligned} i\hbar\frac{\partial\psi}{\partial t} &= \left[-\frac{\hbar^2}{2m^*}(1-i\zeta)\Delta + g|\psi|^2 + \hbar g_r n_r + \frac{i\hbar}{2}(R_r n_r - \gamma)\right]\psi \\ \frac{\partial n_r}{\partial t} &= P - (\gamma_r + R_r|\psi|^2)n_r \end{aligned} \tag{2.18}$$

where ψ is the condensate wavefunction, m^* is the LP mass, γ is a momentum-independent loss rate, n_r is the density of the exciton reservoir, R_r is the scattering rate from the reservoir into the condensate, P is the excitation profile and γ_R is the reservoir loss rate. Interaction within the condensed state and between the condensed particles and the reservoir are modelled by the interaction constants g and g_R, respectively, while the process of relaxation is characterised by ζ [85].

Nowadays, the pumping profile can be almost arbitrary shaped in both shape and/or time using a combination of a multi-beam approach, metallic masks, permanent or programmable diffractive optical elements. For the purpose of this thesis, I am interested in pumping profiles made of several 2D radially symmetric Gaussians arranged in a graph, $P(\mathbf{r}) = \sum_{i=1}^{N} \exp(-2|\mathbf{r} - \mathbf{r_i}|^2/\sigma^2)$ where $\mathbf{r_i}$ is the location of the i-th Gaussian. This excitation geometry may lead to the formation of either a trapped condensate or phase-locked freely-expanding ones depending on the relative distances between the pumping nodes [15]. For the purpose of this thesis, I restrict the discussion to the latter case where polariton condensation occurs on top of each Gaussian profile. Therefore, it is worth to discuss the case of a single Gaussian condensate as the spectral shape of the emission are strongly affected by the pumping strength and geometry, combined with a polariton lifetime. In particular, reference [86] discusses two different spot sizes both twice the threshold power, as shown in figure 2.9:

- $\sigma \sim 20\,\mu m$: the dispersion image reveals a single peak centred at zero momentum and the emission energy is blue-shifted respect to the linear LP dispersion as a consequence of the repulsive interaction with the exciton reservoir;

- $\sigma \sim 1\,\mu m$: the dispersion image reveals two narrow peaks at finite momentum, $\pm k_c$ which fits on the linear LP dispersion. Similarly to the previous case, the exciton density behaves like a static potential hill whose top is populated by the polariton condensate. As such, condensed polaritons start to descent the potential hill accelerating as long as they do not leak out of the cavity. The process of converting potential energy into kinetic can either be complete or partial depending on both polariton lifetime and the extension of the potential.

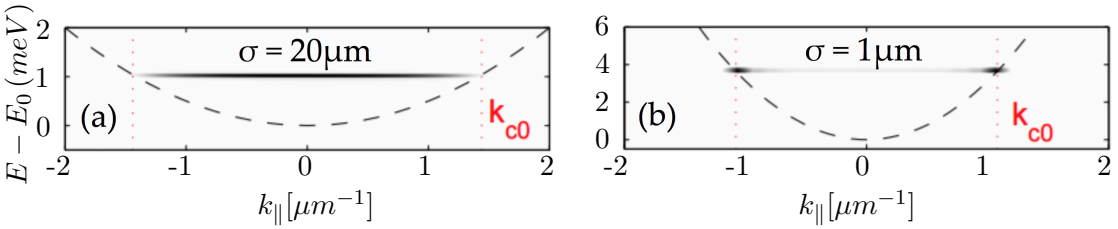

Figure 2.9: Dispersion image at $p = 2\,P_{th}$ for a Gaussian excitation profile with $\sigma = 20\mu m$ (a) and $\sigma = 1\mu m$ (b). Image adapted from reference [86].

In this thesis, I always operate in the second regime, above the trapping criticality and with distances which are usually greater than the spatial extension of the exciton reservoir associated to each graph node. In such configuration, each condensate freely radially expands and these radial flows act as a mutual and coherent resonant exchange of polaritons with its neighbour condensates. As a result, a complex network of couplings is established which is defined and tunabled by the geometry, polarisation and amplitude distribution of the pumping profile. Eventually, the condensates locked their relative phases in order to maximise the density of polariton [14].

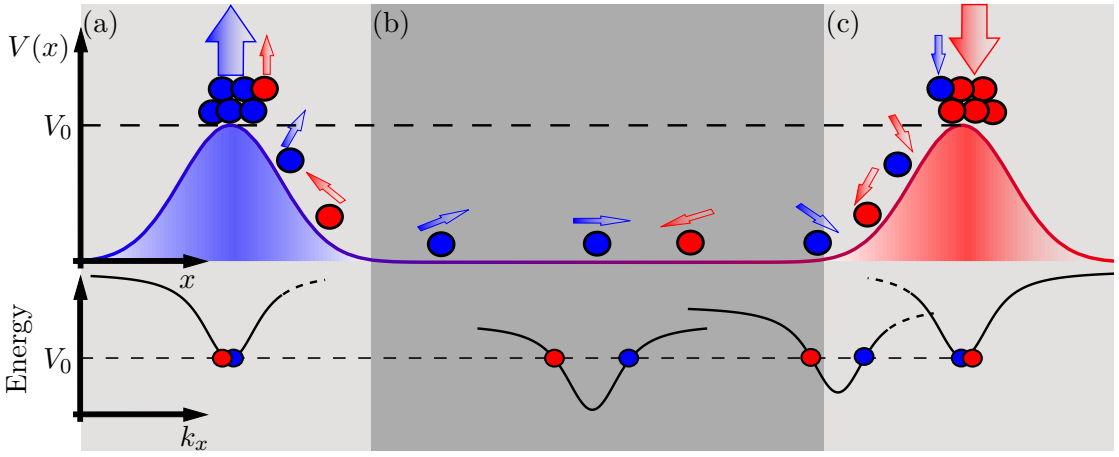

Figure 2.10: Top: Scheme of the ballistic transport of polaritons from the left condensate accelerate and move away from the condensate region (a), propagate at constant velocity (b) and decelerate (c) resonantly feeding the condensate on the right. Arrows show how polaritons' phase evolves in the motion. Bottom: Corresponding schematic representation of the spatially filtered dispersion and polariton energy-momentum state.

Figure 2.10 shows a schematic representation of the phase coupling across two equally pumped co-polarised polariton condensate where the symmetry of the system constraints the relative phase has to be either zero or π. Naively, the system adjusts the relative phase so that ballistically exchanged polaritons are in-phase with the locally excited one. A more detailed study on the phase coupling and its physical origin is discussed in chapter 7.

Chapter 3

Experimental methods and sample

3.1 Real- and Fourier-space imaging

Microcavity polaritons are open dissipative systems which require continuous pumping to balance the loss of polaritons throught photons leaking out of the microcavity. Due to conservation laws, all properties of leaked photons are mapped one-to-one to the properties of the decayed polaritons, i.e. phase, energy, momentum and spin. Therefore, the leaked photons provide a continuous optical readout of the polaritons properties. A common scheme to study polariton microcavities is to build up a setup that allows to measure both the near- and the far-field of the photons leaking out of the sample. The near-field corresponds to the real space intensity map of the sample surface, while the far-field corresponds to the angular distribution of the photons leaked out of the sample. A schematic setup for both real- and Fourier-space imaging is shown in Figure 3.1.

In real-space imaging, the light from the sample plane is collected and collimated using an infinite-corrected microscope objective, L_1, and focused on a charge-couple camera by a plano-convex lens, L_2, to produce a magnified real space image as shown in Figure 3.1(a). Since the amount of photons emitted is proportional to the number of polaritons, the real-space image corresponds to a map of polariton spatial density. By adding an extra plano-convex lens, L_3, in the optical path as shown in Figure 3.1(b), the Fourier-space image is projected onto the focal plane of L_2. Each point in the Fourier-space is given by the superposition of photons in the object plane propagating along a given direction (θ, ϕ), where θ is the emission angle with respect to the normal to the object plane and ϕ is the azimuthal angle. Polariton in-plane wave vector is defined by $k_{\parallel} = k_0 \sin\theta$, with $k_0 = 2\pi/\lambda_0$ and λ_0 being the emission wavelength. Therefore, the Fourier-space image corresponds to a map of the polariton wave vector. The numerical aperture (NA) of L_1 determines the maximum propagation angle collected, $\theta_{max} = \sin^{-1}(NA/n)$, where

n is the refractive index of the medium where L_1 is immersed. Either a camera or the entrance of a spectrometer coupled to a camera is usually positioned at the focal plane of L_2. The latter configuration allows to energy resolve both real- and Fourier-space and, for instance, to directly image polariton dispersion as shown in Figure 4.1(b). It is worth mentioning that the lens configurations of Figure 3.1 can be combined in a modular fashion in order to image the real- and Fourier-space, to spatially filter them and to energy resolved them using a monochromator.

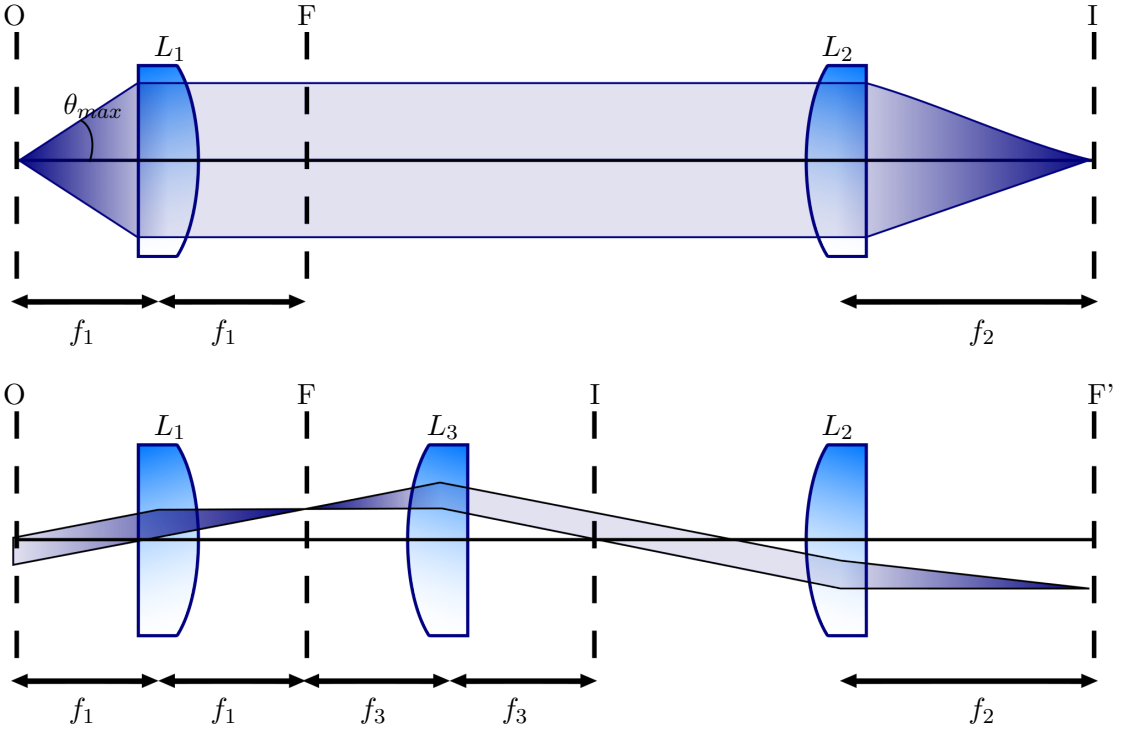

Figure 3.1: (Top) Setup scheme to measure the real-space emission: two lenses, L_1 and L_2, are used to project the image in the object plane, O, onto the image plane, I, with a magnification of $-f_2/f_1$, where f_i are the focal distances of the two lenses. In particular, only the light emitted within a cone dined by the NA of the first lens, $\theta < \theta_{max} = \sin^{-1}(NA/n)$. Note that L_1 generates the Fourier-space image of O in the plane F. (Bottom) Setup scheme to measure the Fourier-space emission: an extra lens, L_3, is added in respect to the real-space imaging configuration. As a result, the object image in O is projected onto the focal plane of L_3 with a magnification of $-f_3/f_1$ and its Fourier-space image, F, is projected onto the focal plane of L_2 with a magnification of $-f_3/f_2$, where f_3 is the focal distance of L_3. Each point in the Fourier-space corresponds to the light emitted in O in specific direction as it is illustrated in the bottom figure using a ray-optic approach.

3.1.1 Filtering

Using one of the schemes presented in Figure 3.1, the real- or the Fourier-space is projected onto the focal plane of L_2 where the emission can be filtered using a transparency mask as shown in Figure 3.2. The mask transmission, $T(x, y)$, is defined as 1 for the region of interest and 0 elsewhere. The most typical masks are the entrance slit of the monochromator (Eq. 3.1a), an iris or a pinhole (Eq. 3.1b).

$$T(x,y) = \begin{cases} 1 & |x - xo| < w/2 \\ 0 & |x - xo| > w/2 \end{cases} \tag{3.1a}$$

$$T(x,y) = \begin{cases} 1 & (x - x_0)^2 + (y - y_0)^2 < r^2 \\ 0 & (x - x_0)^2 + (y - y_0)^2 > r^2 \end{cases} \tag{3.1b}$$

where x_0 and y_0 are the coordinates of the center of the mask in respect to the image, w is the width of the slit of the monochromator and r is the radial aperture of an iris or pinhole. A pinhole is characterized by a fixed r, while the iris aperture can be tuned on demand.

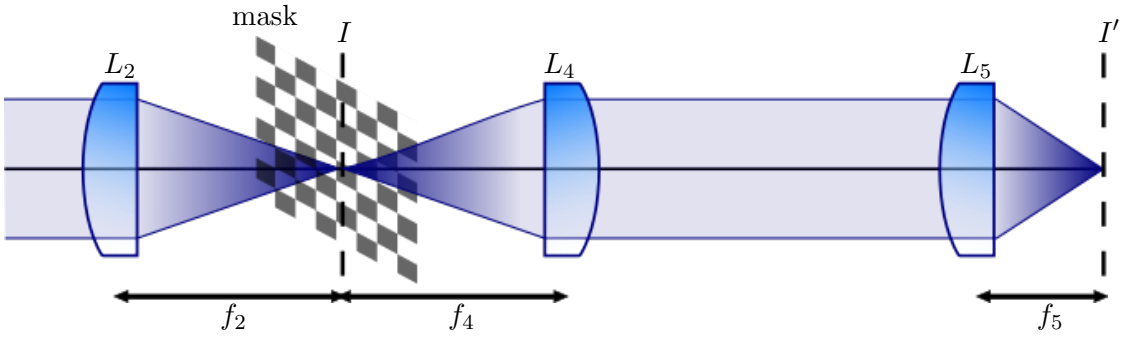

Figure 3.2: An image is reproduced in the focal plane of L_2 (image plane I). A region of interest is selected by inserting a mask whose transmission is 1 or 0 corresponding respectively to the white and grey squares in the figure. The spatially filtered image is then collected and projected onto the image plane I' using two lenses L_4 and L_5, usually coupled to a camera.

3.2 Methods

3.2.1 Calibrations

In order to calibrate the real-space setup, a target with known dimensions is used and placed in the object plane in Figure 3.1. The target is a *Thorlabs positive 1951 USAF test target Ø1" model R1DS1P* which consist of sets of lines. Each set consists of three vertical and three horizontal opaque lines where the line spacing is equal to the opaque

lines width. Each set it is characterized by a group and an element number, (g, e), which determine its line pair density, $n = 2^{g+(e-1)/6} linepair/mm$. Using the lens configuration of Figure 3.1(a) and illuminating with a white light source the target from the back, the target can be projected onto the camera as shown in Figure 3.3(a). The number of pixel corresponding to a line pair, $\Delta x[pixel]$, is equivalent to the actual physical size of the line pair, $\Delta x[mm] = n^{-1}$ resulting in a scaling factor of $0.35\mu m/pixel$. The same procedure applies to both vertical and horizontal dimension allowing to calibrate two axis independently.

Removing the target and switching to the lens configuration of Figure 3.1(b), the Fourier space under white-light illumination is projected onto the camera and, as the white light source emits in all directions, it consists of a circular illuminated region characterized by a sharp edge as shown in Figure 3.3(b). Since only light propagating within θ_{max} can be collected by L_1, the edge points and the centre of the illuminated region can be mapped to photons propagating along the direction defined by (θ_{max}, ϕ) and $(0, 0)$ respectively. The corresponding direction of propagation of the inner points are then obtained with a linear interpolation resulting in a scaling factor of $0.2^o/pixel$.

The spectrometer has been calibrated using a calibrated Argon-Neon source, *Princeton Instruments - IntelliCal*. The lamp has been placed in front of the entrance slit which is close to $20\mu m$ to achieved the best resolution. Using the table provided by the manufacturer [87] three emission lines are found within $860 \pm 10nm$ as shown in Figure 3.3(c). The procedure has been repeated for different central wavelengths covering the range from $800nm$ to $900nm$ and the complete set of tabulated wavelengths has been fit linearly to obtained the calibration curve: $\lambda(x) = \lambda_0 + 0.039 \times (288.2 - x)$ where λ_0 is the wavelength set on the monochromator controller and x is the pixel position on the camera.

3.2.2 Tomography

Tomography is an imaging method which allows to divide an image into sections characterised by a different value of a certain variable and to observe them separately. In particular, I focus the discussion on the so-called energy-tomography technique which allows to filter only photons within a chosen energy interval. I present two different routes to implement this method: the Fabry-Perot approach and the motorised-mirror one.

Fabry-Perot

In the Fabry-Perot method, the light collected by L_1 is transmitted through a Fabry-Perot filter as shown in Figure 3.4. A Fabry-Perot filter is made of two mirrors arranged

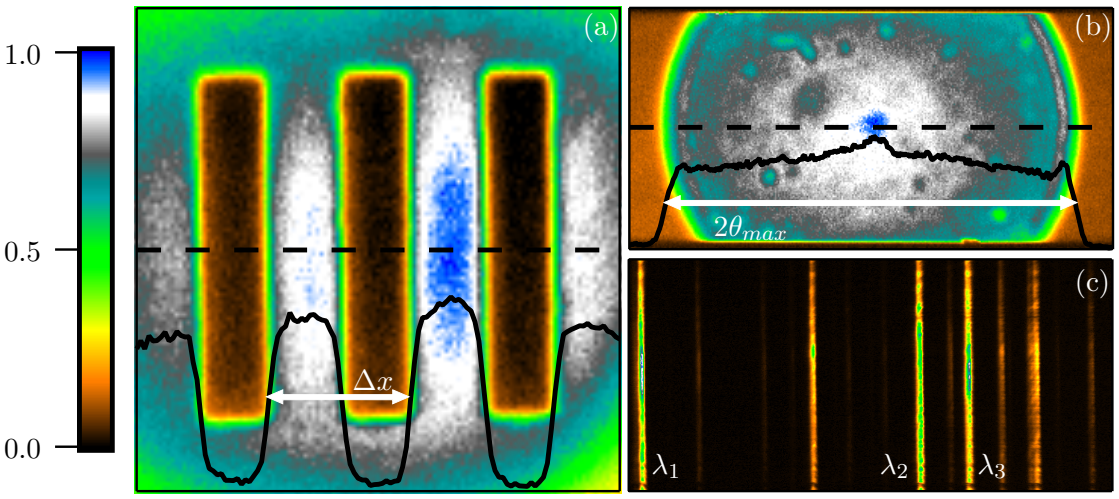

Figure 3.3: (a) Real-space normalized intensity of the horizontal set (g,e)=(6,3) of the test target. The line pair length, Δx, is $12.4\mu m$ and it correspond to 35 pixels on the camera. Therefore, the resulting scaling factor is $0.35\mu m/pixel$. (b) Fourier-space normalized intensity under white-light illumination. The radius of the circle correspond to maximum angle L_1 can collect, θ_{max}. The solid lines in (a) and (b) are the image profiles along the corresponding dashed lines. (c) Energy resolved emission of the Princeton Instrument Argon-Neon lamp within $860 \pm 10nm$ where three wavelengths are found using the table provided by the manufacturer: $\lambda_1 = 852.144nm$, $\lambda_2 = 863.465nm$ and $\lambda_3 = 865.438nm$.

in a cavity geometry and therefore, due to self-interference effect, the transmission spectrum of a Fabry-Perot interferometer presents sharp peaks at certain wavelengths whose positions, λ_0, spectral separation, FSR, and width, BP, are determined by the mirror distance, L, the cavity order, m, and the mirror reflectivity, $R(\lambda)$ as shown in Eq. 3.2

$$\begin{aligned} \lambda_0 &= \frac{2}{m}L \\ FSR &= \frac{\lambda_0}{m} \\ BP &= \frac{2FSR}{\pi}\sin^{-1}\frac{1-R(\lambda)}{2\sqrt{R(\lambda)}} \end{aligned} \tag{3.2}$$

where m is a positive integer number.

The alignment of the two mirrors of the Fabry-Perot interferometer is crucial to obtain a spatially flat energy filter. Therefore, both mirror are mounted on a manual three points adjustment mirror mount and one of them is also equipped with three piezoelectric actuators to finely electrically tune the cavity length, L, the x and y tilting angles. Experimentally, the Fabry-Perot interferometer is put in place so that the first mirror is the one with only manual adjusters and it is aligned perpendicular to the incoming laser beam using the the back reflection. Afterwards, the second mirror is aligned to achieved

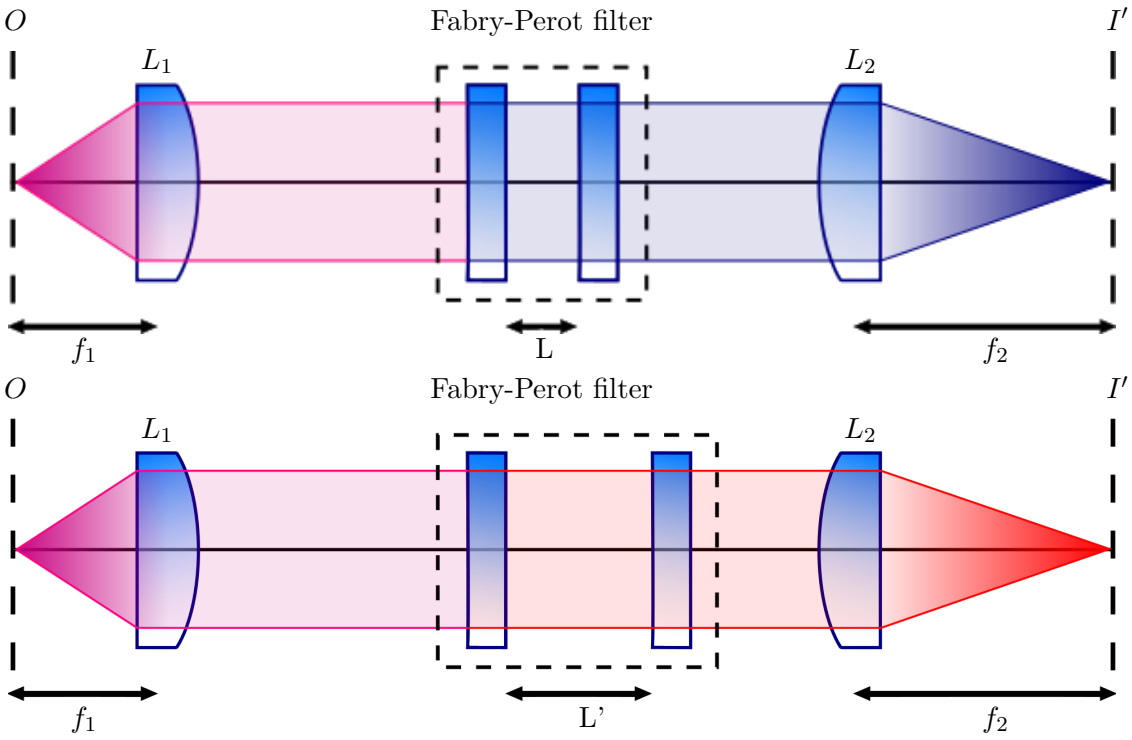

Figure 3.4: The light collected from L_1 is transmitted thought a Fabry-Perot interferometer before being projected in the focal plane of L_2. For a fixed interferometer optical length, L, the transmission of the Fabry-Perot filter is non-vanishing only for wavelengths $\lambda_0 = 2L/m$ where m is any positive integer number, i.e. in the pictures it is shown how the Fabry-Perot filters only the blue (top) or red (bottom) component of the initial red and blue beam accordingly to L.

a fringe-less image on the camera position in the image plane I. The absence of fringes in the measured image is a fingerprint of the flatness of the energy filter in the portion of the image projected onto the camera. To achieve this condition, a sinusoidal signal is applied to the piezoelectric actuator controlling the mirrors separation and x and y tilt angles are adjusted until the whole image recorded on the camera oscillates in-phase. Eventually, the mirrors separation can be electrically tuned with a DC voltage supply in order to tune the energy filter on demand. It is worth mentioning that this approach can be applied to either real- and Fourier-space imaging and it allows to obtain a live two dimensional energy filtered snapshot of the initial image.

Motorized-mirror

In the motorised-mirror method, either the real- or the Fourier-space is projected at the entrance of a monochromator using the appropriate lens configuration described in Figure 3.1. A monochromator is an optical system which reproduce onto its exit slit the image projected onto its entrance slit as it is shown in Figure 3.5(a) and, if needed, to energy resolve it along one direction as it is shown in Figure 3.5(b).

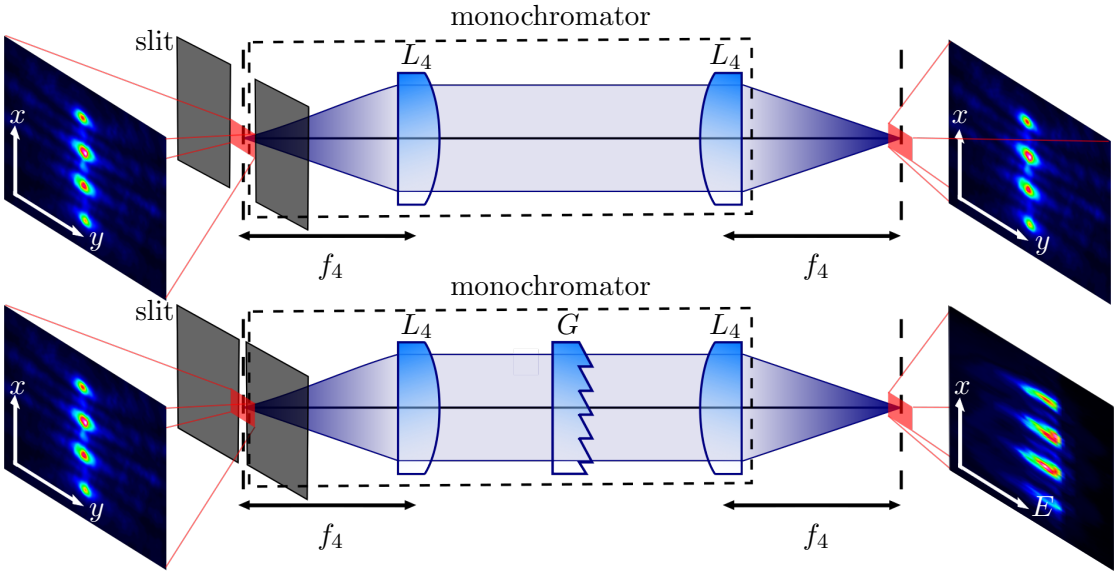

Figure 3.5: (Top) Scheme to reproduce onto the exit slit of a monochromator the image projected onto its entrance slit: the entrance slit is fully open to have the largest field of view. (Bottom) Scheme to energy resolve onto the exit slit of a monochromator the image projected onto its entrance slit: the entrance of the slit is usually sets to the minimum value provided by the instrument in order to achieve the highest spectral resolution. Note that the optical path are not meant to reproduce the inner structure of the monochromator.

The configuration in Figure 3.5(b) is needed to perform the energy tomography. From now on I consider the case of real-space energy tomography, in other words the case where the real-space is projected onto the monochromator entrance slit. In order to achieved the highest energy resolution provided by the instrumentation, the slit is open at the minimum value achievable. As a consequence, the entrance slit is acting as a spatial filter whose transmittance is given by Equation 3.1a. Therefore, the output image, $I(E, y)$, represent a two dimensional map whose axes are energy, E, and position, y, of the input picture spatially filtered around x_0. By using a motorized mirror, it is possible to scan the x dimension and to acquire I(E,x) at different y_i and eventually to reconstruct the two dimensional real-space, I(x,y), at different energies.

3.3 Experimental techniques

3.3.1 Spatial light modulators

A spatial light modulator (SLM) is a device that allows for a bespoken spatial modulation of the amplitude, phase and/or polarisation of a light beam. For the purpose of my thesis, I focus the description on computer-controllable and programmable optoelectronic devices consisting of 2D array of cells filled with liquid crystals (LCs) which

act as modulator material. From now on, the term SLM refers to only this particular type of device. SLMs working principles are based on LCs' birefringence and the possibility to modify their alignment cell to cell by applying a DC voltage, as shown in figure 3.6.

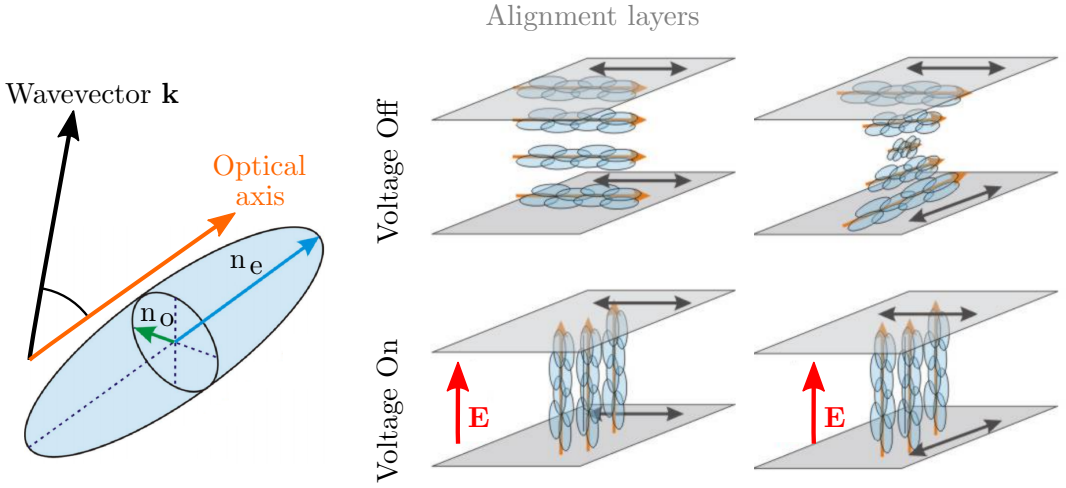

(a) Liquid crystal molecule (b) PAN-LC cell (c) TN-LC cell

Figure 3.6: (a) Schematic of a liquid crystal molecule. Long-range order of the molecular axis leads to the formation of an optical axis giving rise to birefringence $\beta = n_e - n_o$. (b) A PAN-LC cell contains parallel oriented alignment layers leading to a LC cell with uniaxial behaviour. (c) A TN-LC cell has perpendicular oriented alignment layers leading to a helical twist of the LCs? molecular axis for no applied voltage. In both cases (b) and (c) the LC molecules orient along the direction of the electric field E once an external voltage is applied to the cell. The figures are adapt from reference [88].

LCs in SLMs are usually in the so-called *nematic phase* which means that the LC molecules are positioned randomly but show long-range orientational order. As such, they can be described similarly to uniaxial crystal with an optical axis, **c**, and birefringence coefficient, $\beta = n_e - n_o$ where n_o and n_e the ordinary and extraordinary refractive indeces of the material [89]. It is known that in such media any polarised wave travelling at an angle θ with respect to the optical axis can be decomposed into two linearly polarised normal modes a and b with refractive indices [90]

$$n_a = n_o \qquad n_b(\theta) = \frac{n_e n_o}{\sqrt{n_e^2 \cos^2\theta + n_o^2 \sin^2\theta}} \tag{3.3}$$

Therefore, a LC layer of thickness d imposes a phase shift of $\Delta\phi = 2\pi(n_b(\theta) - n_a)d/\lambda_0$ between the two linear component of the incoming beam with wavelength λ_0. As the alignment of the LC molecules can be changed by applying a DC voltage, $\Delta\phi$ can be tuned on demand within the range of 0 to $2\pi\beta d/\lambda_0$.

In most devices, each cell consist of several layers of LC embedded between two electrodes which are coated with alignment layers. SLM are grouped into two classes accordingly if

the two alignment layers are orthogonal or parallel, respectively called *Twisted-Nematic* (TN) and *Parallel Alignment Nematic* (PAN) LCs. In a TN-LC cell, when no voltage is applied, each layer posses a defined optical axis which lies in the layer plane showing a gradual helical twist of 90^o across the cell, while, in a PAN-LC cel, every layer shares the same optical axis, as shown in figure 3.6. The alignment of the LC molecules for both types can be changed by applying a DC voltage at the electrodes allowing to tune the phase delay on demand. The main differences between these two types of cells is that the PAN can be described as a uniaxial crystal, while TN cannot. Therefore, the maximum phase delay provided by a TN cell is more complicated to be computed.

In this thesis, both types of SLMs are in use for the generation of polariton graphs. The beam shaping is realised by using a reflective liquid crystal on silicon SLM, R-SLM, based on PAN-LC cells[1]. An additional polarisation modulation is accomplished by using a transmissive SLM, T-SLM, based on TN-LC cells[2]. The implementations of both SLMs are presented in the next subsection.

3.3.2 SLMs programming

Reflective SLM

It is a known fact that the field distributions of a collimated laser beam at the back and at the front focal planes of a lens, respectively $h(x, y)$ and $g(x, y)$, are linked with a Fourier transform (figure 3.7 and equation 3.4) [93].

$$g(x, y) = H(k_x, k_y)|_{(k_x,k_y)=\frac{2\pi}{\lambda_0 f}(x,y)} \tag{3.4}$$

where $H(k_x, k_y)$ is the Fourier transform of $h(x, y)$, f is the lens focal distance and λ_0 is the laser wavelength.

Referring to the setup described in figure 3.9, $h(x, y)$ is the laser profile at the SLM plane, here a 2D Gaussian beam, $g(x, y)$ is the desired excitation pattern to project onto the sample, here a 2D graph of 2D Gaussian profiles, and $\phi(x, y)$ is the phase pattern displayed on the SLM. For the purpose of my thesis, the phase of the excitation profile is not relevant. Therefore, the phase retrieval problem simplifies to find $\phi(x, y)$ so that $|H|^2$ matches $|g|^2$. The question to be solved is what is the phase of $h(x, y)$, $\phi(x, y)$, in order to achieve the desired intensity pattern $|g(x, y)|^2$ and it represents an example of a *phase retrieval* problem [94–96].

Since phase retrieval problems is ubiquitous in various fields ranging from transmission electron microscopy [97], coherent diffractive imaging, X-ray crystallography [98] and optical wavefront correction in astronomy [99], several methods are available to calculate

[1] PLUTO Phase Only Spatial Light Modulator (reflective), HOLOEYE [91]
[2] LC 2012 Spatial Light Modulator (transmissive), HOLOEYE [92]

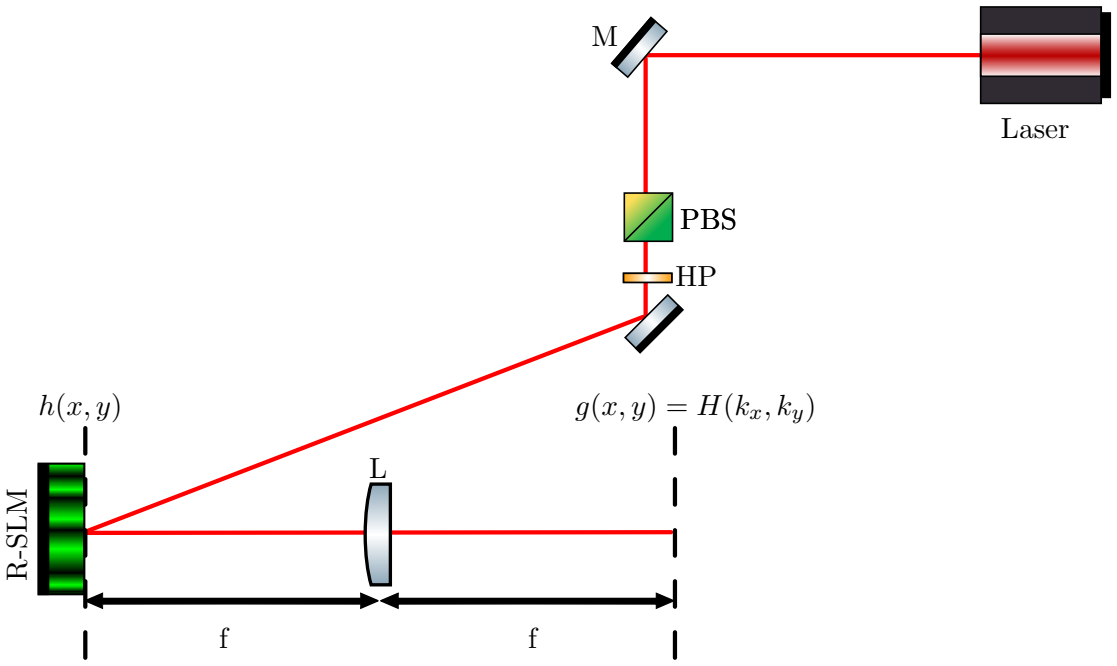

Figure 3.7: Experimental scheme to exploit the Fourier property of a thin lens to generate an arbitrary image in its front focal plane with the help of a SLM.

the phase pattern which includes direct binary search [100], analytic solutions or iterative algorithms based on Fourier or Helmholtz light propagation [101–107].

For the aim of this thesis, I restrict the discussion to a particular set of excitation patterns which are composed of multiple 2D Gaussian profiles spatially separated with the same widths and intensities. The corresponding phase pattern can be exactly analytically calculated but, unfortunately, it requires complex modulation, as shown in equation 3.5. Therefore, they cannot be implemented with the device in use.

$$\phi(x,y) = \sum_{j=0}^{m-1} \exp[i(k_x^j x + k_y^j y)] \tag{3.5}$$

where m is the number of spots required, i is the imaginary unit, k_x^j and k_y^j coefficients determine the position of the j-th spot.

A possible solution is to neglect the amplitude modulation given by equation 3.5 but (1) it results in a decent intensity uniformity between the graph nodes only for simple structures and (2) it creates ghost orders [108]. Both problems can be solved by reducing the SLM active region, i.e. 0 phase delay, but it comes at the dramatic expense of the overall efficiency [108]. It is worth mentioning that it is possible to implement complex modulation in a single phase-only SLM [109]. However, phase-only modulation is still the preferred option due to the higher resolution and efficiency [110].

The most popular approach to compute for the calculation of phase patterns are iterative Fourier transform algorithm (IFTA). An IFTA is defined by the following steps:

1. Measure the beam profile at the SLM, $I_S(x,y)$, and define its corresponding field, $E_S(x,y) = \sqrt{I_S(x,y)}$;
2. Choose a target intensity profile, $I_T(x,y)$, and define its corresponding field, $E_T(x,y) = \sqrt{I_T(x,y)}$;
3. Choose an initial guess phase map, $\phi_0(x,y)$;
4. Define the input field as $E^0_{in} = E_S \exp(i\phi_0(x,y))$;
5. Calculate the output field by means of Fourier transform, $E^0_{out} = \mathcal{F}(E^0_{in})$, and its corresponding output intensity, $I^0_{out} = |E^0_{out}|^2$;
6. Compare I^0_{out} with the desired target intensity map I_T. If the two intensity maps are close enough, then $\phi_0(x,y)$ is the solution to the desired phase retrieval problem, otherwise, the following steps are needed;
7. Generate a new field in the output plane, G^0_{out}, which is usually a combination of E^0_{out} and E_T;
8. Calculate the corresponding input field by means of inverse Fourier transform, $G^0_{in} = \mathcal{F}^{-1}(G^0_{out})$;
9. Define a new input phase mask as the argument of G^0_{in}, $\phi_0(x,y) = arg(G^0_{in})$ and redo the procedure from step number 4.

In addition, it is necessary to design and run at each iteration a procedure to check whether the algorithm is converging or not in order to avoid stagnation.

Two questions remain still open: (1) how to chose the initial guess phase and (2) how to compute G^0_{out}. The strategy to answer the first question is to maximise the overlap between I^0_{out} and I^0_T. To achieve this condition, the initial phase mask can be analytically defined as a combination of a prism and a lens, which are respectively linear and quadratic in respect to the pixel-coordinates. By applying such phase mask, the output intensity remains Gaussian but the prism mask allows to move the image in the focal plane, while the lens mask allows to change its size [111]. The generation of G^0_{out} is basically the main differences between the different algorithms which always represents a trade-off between efficiency and image quality. Here, I report the definition of such field for the two methods widely used in my thesis, the *Gerchburg-Saxton*, GS, and the *Mixed Region Amplitude Freedom*, MRAF (equation 3.6).

$$G_0(x,y) = \begin{cases} E_T e^{iarg(E^0_{out})} & \text{GS algorithm} \\ (mE_T|_{sr} + (1-m)|E^0_{out}|_{nr})e^{iarg(E^0_{out})} & \text{MRAF algorithm} \end{cases} \tag{3.6}$$

where m is the so called mixing parameter, sr and nr are the *signal region* and *noise region*, respectively. In both methods phase freedom is permitted everywhere in the

output plane, while amplitude freedom is allowed only in the noise region of the MRAF one. The additional amplitude degree of freedom is equivalent to ask to the algorithm to converge only in a limited region of space of the output plane, the signal region. As a consequence, the MRAF algorithm produces better quality images than GS but at the expense of the efficiency. As a rule of thumb, the lower the mixing parameter, the better but less efficient the image. In the limiting case of unitary mixing parameter, the two algorithms are equivalent.

A fraction of the light hitting the SLM remains unmodulated for several reasons: the non orthogonal incident angle, the device fill factor, the residual reflection of the active area of the SLM, the non perfect calibration, the cross-talk between adjacent pixels, the pixelation of the modulation and the non-linear response of the device. As a consequence, the calculated image results over imposed to an unwanted bright laser spots in its centre. An approach relies on generating a modulated spots in the target image which destructively interfere with the unmodulated laser light [112]. This approach is very effective but it applies only to analytically calculated pattern. A more general approach relies on spatially offset the calculated image by adding a blazed grating, a focusing lens pattern or a combination of both.

According to the Nyquist-Shannon sampling theorem [113, 114], a signal must be discretised using a sampling frequency at least twice the bandwidth of the signal. In the case of a $N \times M$ pixel SLM, the computation matrix have to be at least $2N \times 2M$ in order to avoid aliasing effects and additional speckle noise. The phase freedom of the SLM is allowed only in the central $N \times M$ part and padded with zeros elsewhere.

Transmissive SLM

After having shaped the beam, the laser image is reproduced in the T-SLM plane, as shown in figure 3.9, where the polarisation of each spot can be changed at will. In particular, we want to smoothly vary the polarisation of each spot from left to right circular at $800\,nm$.

For this task, it is necessary to characterise the T-SLM operation using the Jones matrix formalism [115]. As the T-SLM in use is based on TN-LC cells, the theoretical calculation of the Jones matrix is non-trivial [116] but it depends on parameters not provided by the manufacturer. Therefore, an experimental routine has been implemented to determine the Jones matrix of the T-SLM for each possible grey-level $g = 0, \ldots, 255$, $M(g)$ [117].

Here, I report briefly the main details of the calibration process which has been implemented by J.D. Töpfer during his Master' project. After having tested its working principles, we designed and built together an extension of the setup to accommodate the T-SLM in order to arbitrarily change the polarisation of each spot of the laser image, as shown in figure 3.9.

The generic form of the Jones matrix for a non-absorbing polarisation device can be written as

$$M = e^{i\alpha} \begin{pmatrix} X - iY & Z - iW \\ -Z - iW & X + iY \end{pmatrix} \tag{3.7}$$

where α is a global phase shift (non relevant for our scope), X, Y, W and Z are real parameters in the range $[-1, 1]$ that satisfy the normalisation condition $X^2 + Y^2 + Z^2 + W^2 = 1$. Measurement of the transmitted light though the T-SLM in seven different configurations, which differs in incoming and detected polarisation, enables to analytically calculate the four coefficients [118].

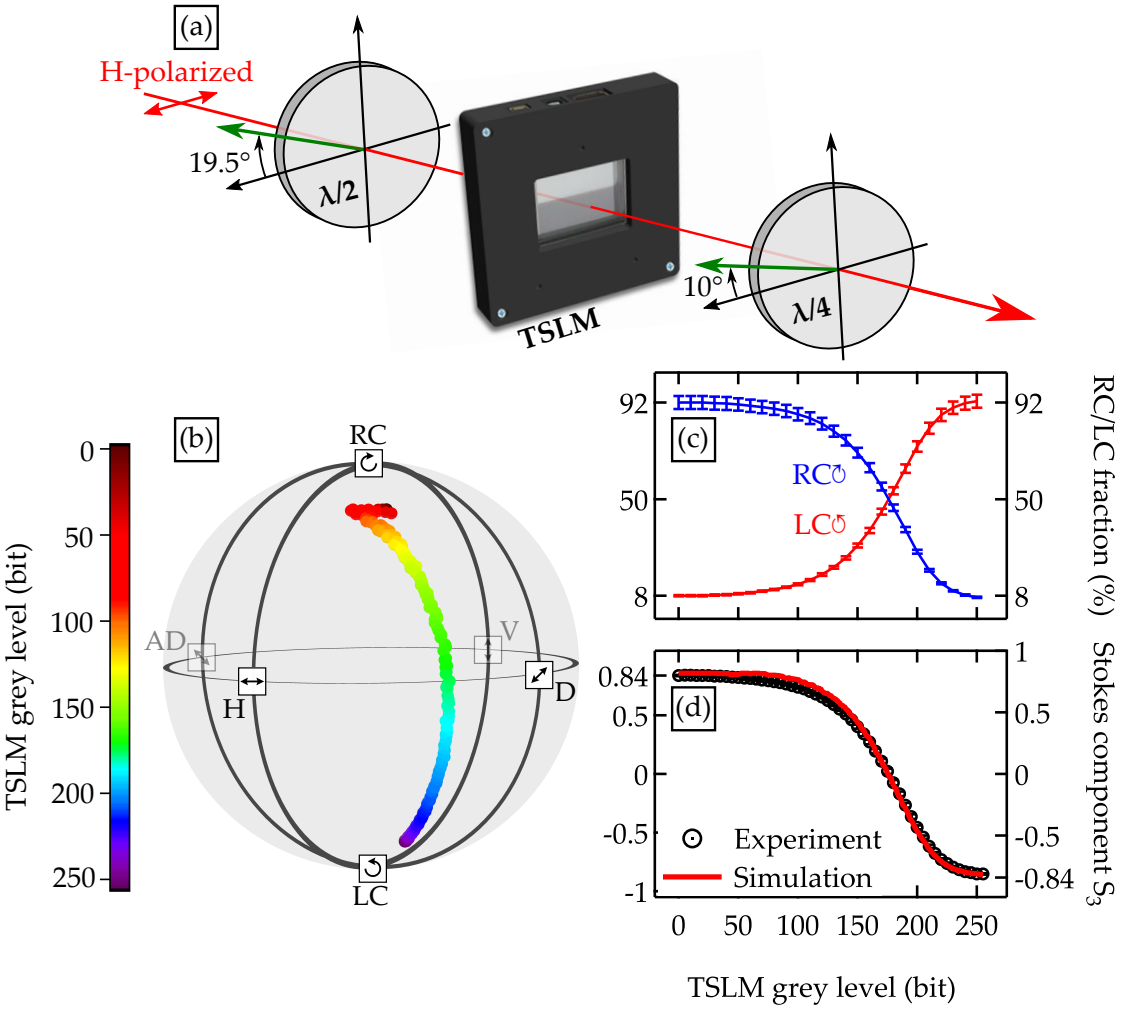

Figure 3.8: (a) Configuration incorporating a T-SLM, a $\lambda/2$ and a $\lambda/4$ waveplates used for the polarisation modulation. An incoming beam with horizontal polarisation is converted into a polarised states on an equi-azimuthal curve as shown in (b). The experimentally measured circular fractions, $I_{R,L}/I_R + I_L$, and circular Stokes component S_3 are shown in (c) and (d) as a function of the T-SLM grey level g. Also, good agreement it is shown in (d) with the simulations using the determined Jones matrix. Starting with a 'black screen' and $S_3(g = 0) = 0.84$, the polarisation state becomes linear by increasing the grey level, $S_3(g = 175) = 0$, and, ultimately, the circular faction inverts for a 'white screen', $S_3(g = 255) = -0.84$. Figure is taken from reference [118]

After having calculated the T-SLM Jones matrix, it is possible to design a system consisting of a $\lambda/2$ and a $\lambda/4$ waveplates, as shown in figure 3.8, to maximise the polarisation modulation depth, $|S_3(g=0) - S_3(g=255)|$ [119]. As a result, we obtained a surprisingly high polarisation modulation, $S_3(g=0) = 0.84$ and $S_3(g=255) = -0.84$, considering that the device is designed for the visible range and not for the near-infrared. Even though the resulting light for the extremes of the grey values is not 100% polarised, we can safely use this scheme to non-resonantly excite a left or right polarised polariton condensate keeping in mind that (1) the light polarisation is also partially distorted at the focal of a large NA lens [120] and that (2) the relaxation process already induces a partial depolarisation of the injected light [121].

3.3.3 Transmission-like setup

The setup described in this subsection has been used for all the measurements of my thesis. The setup is configured in the transmission-like geometry, where two different microscope objectives (or lenses) are used for excitation and collection, as it is shown in figure 3.9.

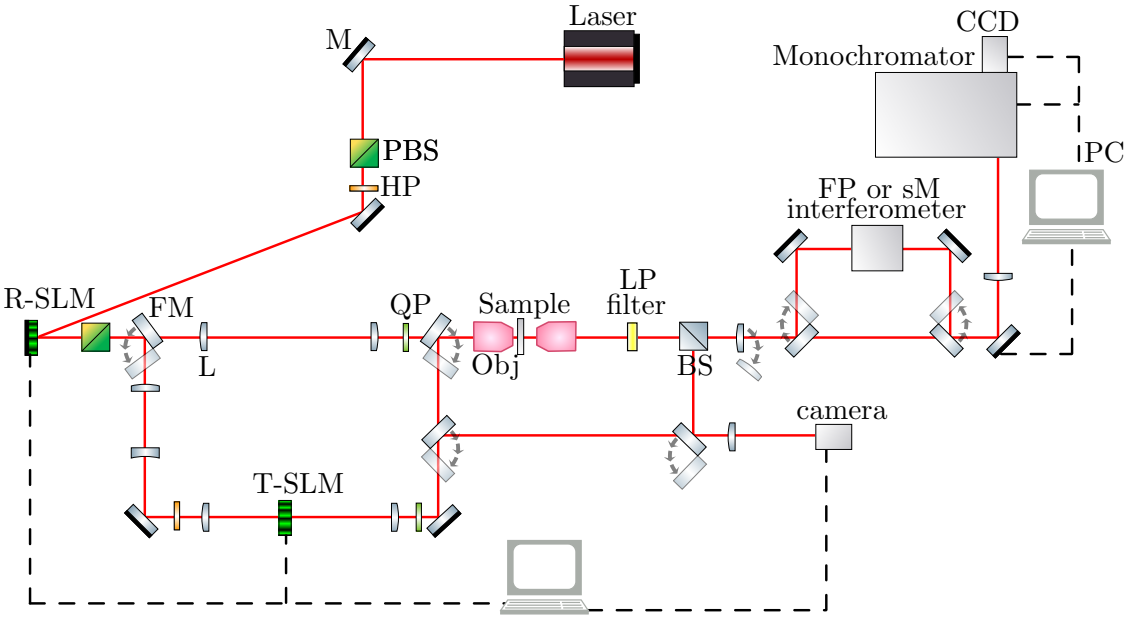

Figure 3.9: Setup scheme as described in the text.

In all the measurements, the sample is held at approximately 6 K in a cold-finger continuous flow cryostat and optically pumped non-resonantly from the episide. The excitation lasers have been all tuned at the first minimum above the stop-band, here 800 nm, as shown in Figure 3.10(b). A polarised beam splitter (PBS) and a half-wave plate (HP) before the R-SLM act as power control because the R-SLM in use modulates only horizontally polarised light. A PBS after the R-SLM removes any spurious component of the modulated beam and then a quarter-wave plate (QP) is used to convert the horizontal

polarised beam into circular. A 3 lenses system is used to project onto the sample the desired excitation pattern; the lenses are chosen so that (1) the sample and the SLM planes are conjugate to achieve the best resolution, (2) the pattern in the sample plane has the desired dimensions and (3) the laser beam does not either under fill or overfill the last lens. An iris is located at the focal plane of the first lens to (1) spatially filter on demand the excitation pattern and (2) to block any unwanted diffraction order from the R-SLM. Alternatively, two flipper mirrors (FMs) enables to elongate the optical path from the R-SLM to the same chosen excitation lens in order to accommodate the T-SLM and its relative polarisation optics as discussed in subsection 3.3.2. The PL was recorded in the transmission geometry through the GaAs substrate with a microscope objective. In front of the back aperture of the collection objective is placed a 808 nm long-pass filter in order to ensure that any residual scattered laser light is blocked. After being reflected on a mirror whose tilting angles can be electrically driven, the PL is projected with an achromatic plano-convex lens on the entrance slit of a 300 mm spectrometer equipped both with a mirror and a 1200 groves/mm grating which is coupled to a charge coupled device (CCD). By using FMs, the PL can be coupled to a stabilised Michelson interferometer (sM) or to a Fabry-Perot (FP) one, respectively described in subsections 3.3.4 and 3.2.2. On demand, the PL can split into two just after the collection objective with a 50:50 beam splitter (BS) enabling to simultaneously record both real-space (camera) and Fourier-space/dispersion image (CCD). After the T-SLM, a FM allows to project onto a camera the excitation path without going through both objectives allowing for a daily routine of calibration of the T-SLM and its associated HP and QP as discussed in subsection 3.3.2.

Stokes components of the PL can be directly measured by inserting a proper set of polarisation optics in the collection optical path (not drawn in figure 3.9). 2D Stokes components can be then calculated as

$$S_{1,2,3} = \frac{I_{H,D,L} - I_{V,AD,R}}{I_{H,D,L} + I_{V,AD,R}} \tag{3.8}$$

where $S_{1,2,3}$ are respectively the linear, diagonal and circular polarisation components, $I_{H,D,L}$ and $I_{V,AD,R}$ are the intensities of the difference polarisation components, i.e. horizontal (H), vertical (V), diagonal (D), anti-diagonal (AD), left-circular (L) and right-circular (R).

3.3.4 Stabilised Michelson interferometry

Polariton condensation is characterised by a built up of long range coherence. One way to measure the degree of coherence of a light source is by performing interferometric

measurements and then by calculating the fringe visibility, V [122]:

$$V = \frac{I_{max} - I_{min}}{I_{max} + I_{min}} \tag{3.9}$$

with I_{max} and I_{min} being respectively the intensities corresponding to the maximum and adjacent minimum in the fringe system.

To show the coherence build up above threshold of a polariton condensate (chapter 4), we measure the fringe visibility by means of an actively stabilised Michelson interferometer in a mirror-retroreflector configuration [9]. The use of a stabilised Michelson interferometer is preferred in respect the Mach-Zehnder interferometer because it guarantees a more accurate fringe visibility measurements by suppressing vibrational noise.

3.4 Sample

A microcavity polariton sample usually consists of a microcavity (MC) sandwiched between two distributed Bragg reflectors (DBRs) with groups of quantum wells (QWs) embedded inside the MC at the anti-nodes of cavity field intensity to enhance the light-matter coupling and to stabilised the exciton as shown in Figure 3.10.

Several materials have already shown polariton Bose-Einstein condensation (BEC) including CdTe, GaAs, GaN, ZnO [10, 43–45] and, more recently, organic semiconductors [46–48]. Among these variety of material choice, GaAs is the preferred material to study polariton fluidic because AlAs/GaAs heterostructures benefit from a moderate exciton binding energy of approximately $10\,meV$ and have a small lattice mismatch together with a high bandgap difference which results in a structure with low photonic and excitonic disorder. As a downside, GaAs does not allow to work in transmission-like geometry (described in Subsection 3.3.3) without further processing after the sample growth because the natural substrate on which to grow this structure, GaAs itself, is not transparent for the emission wavelength. Moreover, although the lattice mismatch of GaAs and AlAs is as small as 0.14% at room temperature [123], it leads to the formation of cross-hatched dislocation and point defects which can generates localisation [124] and elastic scattering [125–128] affecting polariton propagation.

Transmission-like geometry can be achieved by using InGaAs QWs embedded in a GaAs MC with GaAs/AlAs DBRs but it induces further strain in the QWs which may eventually be transferred into strain in the mirrors [129]. Furthermore, it has been shown that an indium content of 3% or lower causes the exciton level of individual wells to hybridise making the observation of condensation difficult [130]. Therefore, the sample design is a compromise between the sample quality and the the exciton confinement strength. Introducing a thin layer of AlP in each AlAs layer of the DBRs results in a strain reduction leading to a lower density of cross-hatched dislocations density [131]. On the basis

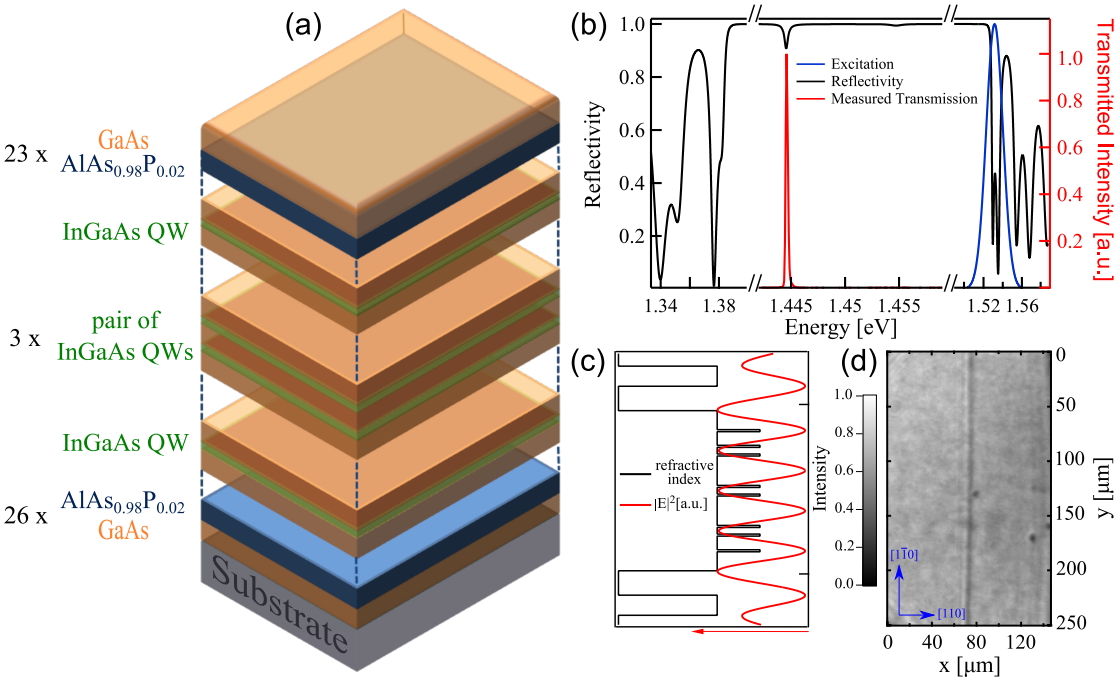

Figure 3.10: (a) Sketch of the microcavity structure: top (bottom) DBR made of 23 (26) pairs of GaAs/$AlAs_{0.98}P_{0.02}$, 2λ GaAs microcavity with embedded 3 pairs of $In_{0.08}Ga_{0.92}As$ QWs placed at the maxima of the field amplitude and two additional QWs at the first and last minima of the field amplitude as carrier collection wells. (b) Calculated reflectivity spectrum of the cavity stop band with the transfer matrix method (black line) and experimental transmittance spectrum for detuning of $-5.8\,meV$. (red line) (c) Sketch of the energy gap (black line) along the growth direction and the corresponding field amplitude of the cavity mode (red line). (d) Real space transmission intensity image of the sample surface under white light illumination on a linear grey scale, as indicated. Figures are adapted from Ref. [1].

of this work, another strain-compensated MC sample was realised at the University of Sheffield and, eventually, it enabled the first observation of polariton condensation in a strain-compensated planar MC with InGaAs QWs [1].

As I describe in Chapter 7, the coupling in a polariton graph is established by polariton ballistically propagates across the graph nodes. Therefore, the density of defects sets a upper limit to the polariton graph size which can be coherently coupled. Furthermore, the transmission-like geometry decouples the excitation and collection optical systems enabling an easier engineering of complex excitation conditions.

For the above-mentioned reasons, the work reported in this Thesis has been carried out on a strain-compensated planar microcavity with InGaAs quantum wells grown by MBE. The sample was provided by Professor Wolfgang Langbein (University of

Cardiff) who has designed it together with Professor Pavlos G. Lagoudakis (University and Southampton). The sample description is provided in Subsection 3.4.1, while I discuss the observation of polariton condensation in this sample in Chapter 4.

3.4.1 InGaAs strain-compensated microcavity

The sample is a 2λ GaAs MC with embedded $In_{0.08}Ga_{0.92}As$ QWs. Three pairs of 6nm QWs are placed at the anti-nodes of the cavity field as well as two additional QWs at the first and last node to serve as carrier collection wells, as shown in Figure 3.10(c). The number of QWs are chosen to increase the vacuum Rabi splitting and to keep the exciton density per QW below the Mott density [132] at sufficiently high total exciton density to achieved polariton BEC. A wide range of detuning are accessible due to wedge of the cavity thickness. Strain compensation is achieved by $AlAs_{0.98}P_{0.02}/GaAs$ DBRs instead of the thin AlP layer used in Ref. [131] because the pseudo-alloy composition can be better controlled in the growth process. The top (bottom) DBR is made of 23 (26) periods as shown in Figure 3.10(a), resulting in a reflectivity higher than 99.9% in the stop-band region of the spectrum as shown in Figure 3.10(b). The average density of hatched dislocations along the [100] direction was estimated from the transmission imaging to be about 6/mm, while no hatched dislocations along the $[1\bar{1}0]$ direction were observed, as shown in Figure 3.10(d).

From the transmitted spectrum at a detuning of -5.8meV shown in Figure 3.10(b), at which the LP has a linewidth of $120 \pm 50\,\mu$eV and an exciton fraction of 20.5%, we obtained a LP Q-factor of 12000 while the photonic Q-factor obtained from reflectivity spectrum calculated using the transfer matrix method is 25000. It is worth mentioning that the simulation has been performed neglecting the in-plane disorder and residual absorption and that the low temperature, 6K, refractive indices of 3.556 and 3.015 have been used for GaAs and $AlAs_{0.98}P_{0.02}$ layers, respectively.

Chapter 4

Polariton condensation in a strain-compensated microcavity

Under specific conditions, polariton systems were reported to undergo a transition into a coherent state. This coherent state shares some characteristic features of both conventional BEC and photon laser but it is usually not at thermal equilibrium with the host lattice [9] and it does not require population invertion [35]. Even though it was recently proved that polariton condensation is not intrinsically a non-equilibrium effect [82], whether to call this transition polariton lasing or polariton condensation is still under debate in the community [79, 133–135] because polariton lifetime of the order of hundreds of picoseconds are needed to achieve thermal equilibrium. Despite the controversy is still open for short-lifetime polaritons, the spontaneous formation of a coherence state is a well-establish fact which has been reported in several samples [8]. However, the observation of polariton condensation in GaAs-bases planar MC with InGaAs QWs is still missing.

To demonstrate polariton condensation, it is important to show that:

- the system is in the strong coupling regime
- the LP emission presents a continuous blueshift of the emission and it shows a threshold at which the intensity grows non-linearly and the linewidth shirks
- the lasing occurs on the polariton mode
- the formation of phase spatial correlation
- a second threshold is observed at higher excitation fluence [136]

where the first three points set an unequivocal distinction between polariton and photon lasing.

In the following sections, we demonstrate the observation of polariton condensate in a strain-compensate planar MC with InGaAs QWs (sample's details are reported in Section 3.4.1) using real- and Fourier-space imaging under non-resonant optical pulsed excitation.

4.1 Experimental method

The sample and the setup are described in details in Subsection 3.4.1 and 3.3.3, respectively, where the R-SLM is replaced with a mirror. The sample was optically pumped non-resonantly from the episide using a 180 fs pulsed Ti:Sapphire laser with a repetition rate of 80 MHz tuned to the first reflectivity minimum above the cavity stop band as it is shown in Figure 3.10(b). The photoluminescence was recorded in the transmission geometry through the GaAs substrate with a $\pm 40^o$ collection angle by a 0.65 NA microscope objective and was spectrally resolved using a 1200 grooves/mm grating in a 300 mm spectrometer coupled to a charge coupled device.

4.2 Strong coupling regime

Figure 4.1(a) shows the LP and UP dispersions below the condensation threshold at a detuning of -5meV. The measured LP dispersion is clearly non parabolic, contrarily to the expected one for a cavity photon. As discussed in Section 2.1.3, the anti-crossing behaviour represents an unequivocal fingerprint of the strong coupling regime [7]. Therefore, taking advantage spatial dependence of the detuning due to the cavity wedge discussed in Section 3.4.1, we recorded the dispersion images at different position on the sample and we extract the LP and UP energy at normal incidence in order to observe the anti-crossing behaviour as it is shown in Figure 4.1(b). Eventually, we fit the obtained data using two coupled harmonic oscillators model [32] and we obtained a vacuum Rabi splitting of approximately 8meV.

4.3 Polariton condensation

We excited the sample with a two dimensional radially symmetric Gaussian profile with a $35\mu m$ full width half maximum (FWHM) using a 5 cm lens in order to observe condensation at $k_{\parallel} \sim 0$ [86]. The non-resonant excitation creates an electron-hole pairs in the InGaAs QWs and GaAs MC which rapidly relax to populate the LP dispersion and the weakly coupled QWs exciton reservoir. By increasing the excitation fluence, the polariton relaxation rate into the ground state of the LP increases and, eventually, overcomes its radiative decay resulting in a macroscopic population of the ground state

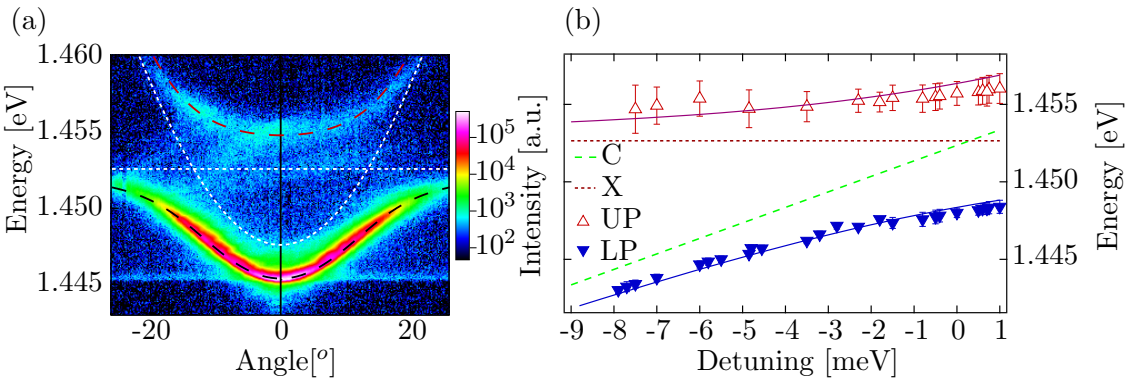

Figure 4.1: (a) LP and UP dispersions below the condensation threshold on a logarithmic color scale as given. The white dashed lines depict the bare exciton (X) and cavity (C) modes and the blue and red solid lines are the calculated LP and UP dispersions. (b) LP and UP energy at normal incidence for different detuning conditions. The error bars correspond to the FWHM of a Gaussian fit to the spectra. The blue (purple) line show the calculated LP (UP), and the dashed green (red) line shows the bare cavity (exciton) mode. Figures are adapted from Ref. [1]

[9]. Figure 4.2(a) shows the both LP and UP dispersions in the low fluence regime, where the renormalisation is negligible. By increasing the excitation fluence, we observe a threshold at $P_{th} = 26\mu J/cm^2$ at which the emission shrinks around $k \sim 0$ in Fourier-space as shown in the intensity profiles in Figures 4.2(a) to 4.2(c). Above threshold the emission at high k follows the calculated LP dispersion, proving the system is still in the strong coupling regime. The LP emission spectrum shows the characteristic feature of a polariton BEC, namely, a linewidth narrowing, Figure 4.2(d), a continuous blueshift of the emission energy, Figure 4.2(e), and a non-linear increase of the emission intensity, Figure 4.2(f). As expected, above the condensation threshold, we observe a broadening of the LP emission and still a blueshift of the emission as the interaction between the condensate and the reservoir becomes stronger [137].

4.4 Photon lasing

The data presented in Section 4.3 are a good indication that we observe polariton condensation using the strain compensated InGaAs sample. To further increase our confidence, we wanted to prove that our structure exhibits a second intensity threshold as the excitation fluence is increased and one enters the photon lasing (weak coupling) regime. The major signature of this behaviour is the observation of two fluence-driven thresholds characterised by a non-linear increase of the emission and a linewidth narrowing.

Photon lasing requires an inversion of the electronic population and, therefore, it is expected to have a threshold fluence of about two order of magnitude higher than polariton

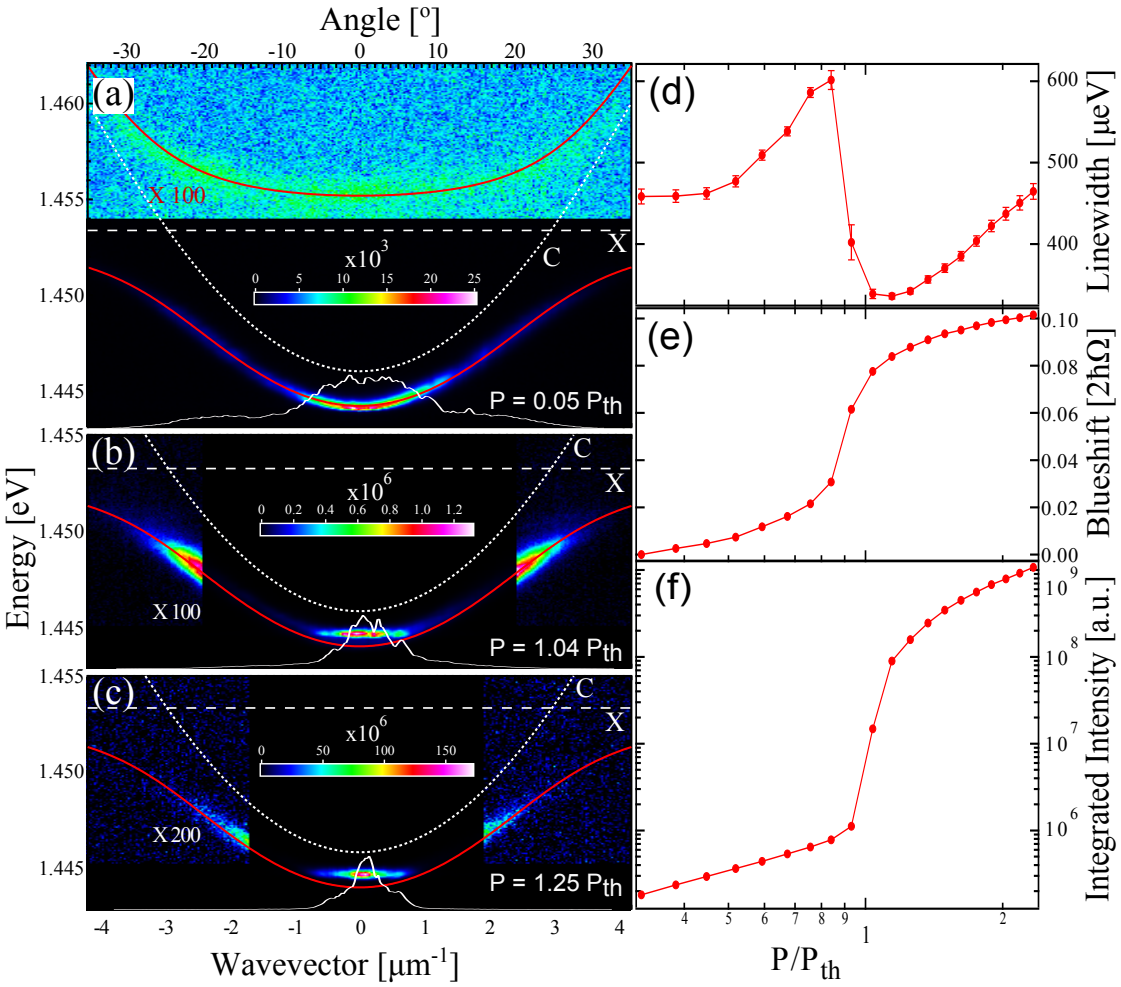

Figure 4.2: Dispersion images on a linear colour scale as indicated below (a), at (b) and above (c) the condensation threshold. The red solid lines are the calculated LP and UP dispersions, while the white dotted and dash lines shows the uncoupled cavity and exciton dispersions, respectively. In (a) the UP energy range is visible, scaled as indicated. The data in (b) and (c) have been scaled as indicated for $|k|$ greater than $2.5\mu m^{-1}$ and $1.8\mu m^{-1}$, respectively. Profiles of the LP emission along k are also shown as white lines. (d) Linewidth, (e) energy shift in unit of the vacuum Rabi splitting and (f) integrated intensity at $k \sim 0$ versus excitation fluence. Figure taken from Ref. [1].

lasing [35]. To achieved this condition, we changed the excitation lens in order to reduce the excitation spot size down to $9.2\mu m$ FWHM. The reduction of the excitation spot leads to polariton condensation at a finite k due to the steepness of the potential profile induced by the repulsive interaction between polaritons and with the exciton reservoir [86]. Therefore, in order to record the evolution of both polariton and photon lasing, we integrated the dispersion image from $1.441\,eV$ to $1.458\,eV$ and $|k| < 3.4\mu m^{-1}$.

As shown in Figure 4.3(a), we observed two threshold behaviour showing an abrupt increase of the emission and a linewidth narrowing. As expected, the second threshold

occurs at a fluence 20 times higher than the first one. Due to integration procedure, we noted that the resulting linewidth is broader and that the intensity increase at both threshold is smaller than the one observed in figure 4.2(d). Figure 4.3(b) shows the energy shift of the emission colour-coded with the average wave-vector of the emission, $\langle k \rangle$. As observed in Section 4.3, we observed a continuous increase of the emission energy and k. However, upon crossing the second threshold, the emission energy shifts towards the energy of the bottom of the uncoupled photonic dispersion. We attributed this behaviour to the transition to the photon lasing [138] indicating that the system is now in the weak-coupling regime following the dissociation of the exciton. This regime is achieved when the so-called Bernard-Duraffourg condition is fulfilled [139] or, in other words, when the electronic population is inverted.

To show the coherence build up above threshold, we carried out interference measurements using an actively stabilised Michelson interferometer in a mirror-retroreflector configuration [9] as described in Section 3.3.4. We measured the phase spatial correlation of the emission in respect with its centre and we extracted the fringe visibilities using Equation 3.9. The measured fringe visibility of both polariton condensate and photon lasing is extended and, as expected for a coherent source, reaches up to about 80%, as shown in Figures 4.3(c) to 4.3(f).

4.5 Conclusions

We presented the first experimental evidence of polariton condensation in a strain-compensated microcavity with suppressed disorder which enables transmission-like geometry. The result was achieved under non-resonant ultra-fast optical excitation without leaving any doubt about the origin of the observed coherence. We proved that the system is in the strong coupling regime and we observed all the characteristic features of a polariton BEC, long-range spatial coherence, non-linear increase of the emission, a linewidth narrowing and a continuos blueshift of the emission energy. We corroborated the observation of polariton BEC by recording a second threshold fluence associated with the well-known photon lasing regime in VCSEL structure. Condensation in a structure with suppressed disorder promises to be a suited system for studying the nature of quantum fluid phenomena [70, 71, 140] and it represents a necessary step towards the implementation of periodic lattices of interacting condensates, providing a platform for on chip simulations [2].

4.6 Contributions and Publications

The experiments reported in this chapter have been carried out mainly by the Pasquale Cilibrizzi, Alexis Askitopoulos and the author. All the data reported in this chapter

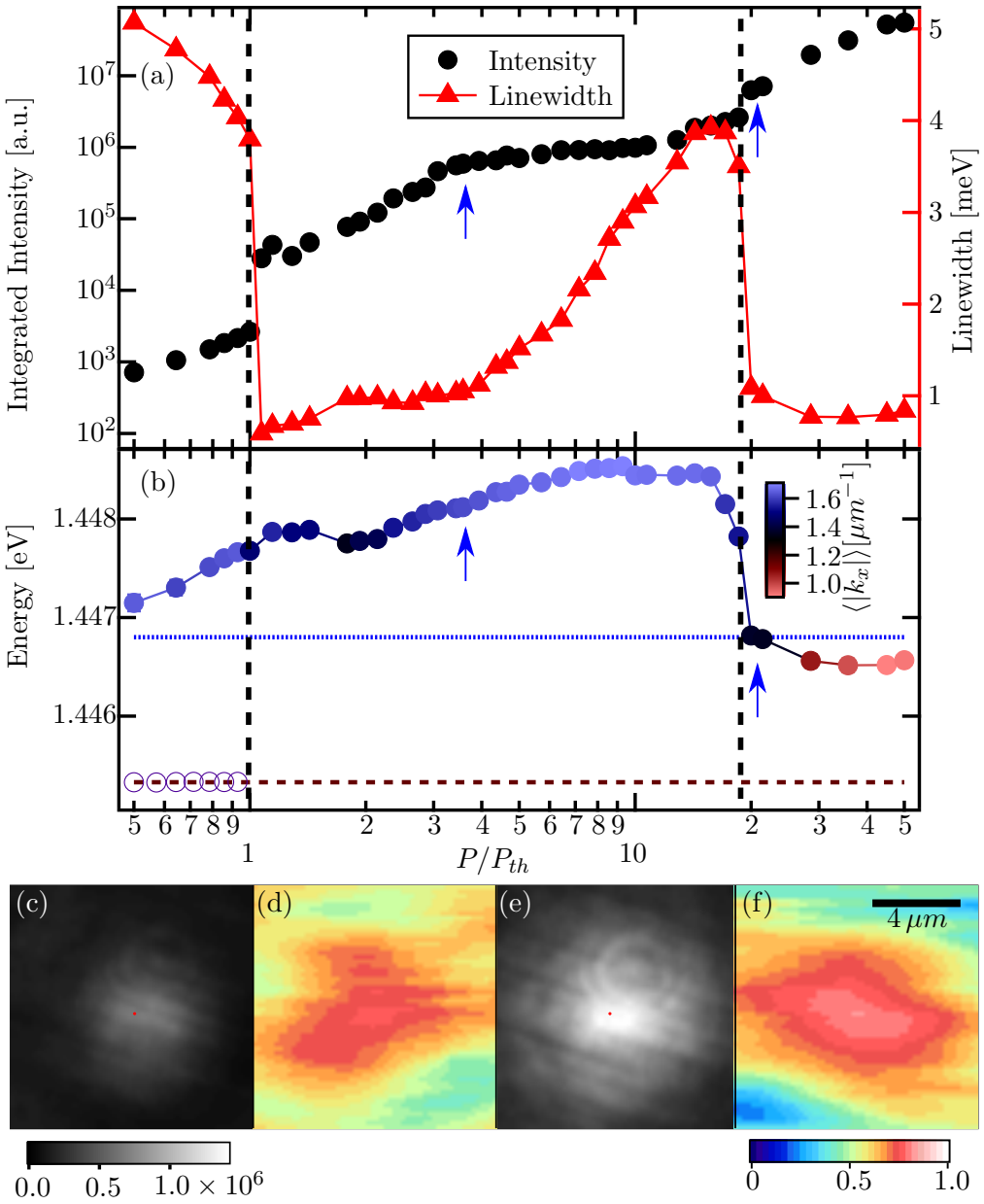

Figure 4.3: (a) LP emission linewidth and integrated intensity as function of the excitation fluence P relative to the polariton condensation threshold. We integrated the emission over the entire LP dispersion, from $1.441\,eV$ to $1.458\,eV$ and $|k| < 3.4\mu m^{-1}$. (b) Average energy colour-coded with the average wavevector, $\langle k \rangle$. The empty circles show the emission from the LP brunch at $k \sim 0$ below threshold. The dotted lines indicate the energy of the cavity (blue) and the LP (brown) at $k \sim 0$. (c,e) Real-space emission intensity and (d,f) fringe visibility in the regime of polariton condensation at $P = 3.8P_{th}$ ((c,d) and photon lasing at $P = 20P_{th}$ (e,f), as indicated by the two blue arrows in (a,b). The visibility is averaged over 24 different phase shifts. The red spots in (c) and (e) indicate $\mathbf{r} = 0$ used in (d,f). Figure taken from Ref. [1].

have been published previously in Ref. [1].

Chapter 5

Realising the classical XY Hamiltonian in polariton simulators

Optimisation problems are ubiquitous in the modern era from social to natural sciences, i.e. protein folding [141], behaviour of financial market [142], dynamics of neural networks [143], behaviour of multi-agent systems [144], devising new chemical materials [145] and finding the ground state of spin liquids [146]. Unfortunately, most of these problems cannot be efficiently tackled with classical computer because their complexity does not scale polynomially with the problem size. An alternative route to efficiently solve these intractable problems was envisioned by Feynman in 1982 who introduced the concept of simulator [147]. A simulator is a problem dedicated device which *mimics* the behaviour of the physical problem of interest enabling either to test and verify its current theoretical model or to gain (further) information about it [148]. Recently, it was demonstrated that most of these optimisation tasks can be mapped into certain universal classical spin models that are characterised by a given set of degrees of freedom, spins, by their interactions, couplings, and by a associated cost function, Hamiltonians [149]. As a results, there is a strong interest across the whole scientific community to realise a simulator able to solve such spin models.

Various systems were proposed and demonstrated to act as a Hamiltonian simulator using networks of artificial spins: superconducting flux quantum bits [150], atomic optical lattices [151] , a network of coupled lasers [152], a network of optical parametric oscillators [153–156], trapped ions [157], phonons in electromechanical systems [158]. In this chapter, I introduce a new platform based on polariton graph to compute the ground state of the classical XY Hamiltonian.

Polariton condensates can be imprinted into any 2D graph by modulating the spatial profile of the excitation beam, offering straightforward scalability. Under optical injection, the network of coupling can be arbitrary tuned by controlling the density profile and polarisation of each individual condensate providing unprecedented control of the cross-site interaction [3, 5]. Due to the finite polariton lifetime, the information about the polariton graph are continuously optically read enabling in-situ characterisation of stationary polariton graph. Furthermore, the bottom-up approach for the search of the ground state of the XY Hamiltonian is achievable within the linewidth of the corresponding state. This is an advantage compared to annealing techniques, where the global minimum is reached though transitions over local minima. In a future prospective, polariton devices have also been demonstrated to sustain room temperature operation [10, 45–48] and electrical injection [11, 159] and it is currently under investigation how to push polariton systems into the full quantum regime [160].

5.1 Experimental method

The sample and the setup are described in details in section 3.4.1 and 3.3.3 respectively. The sample was optically pumped non-resonantly from the episide using a continuous-wave Ti:Sapphire laser tuned to the first reflectivity minimum above the cavity stop band as it is shown in figure 3.10(b). The spatial profile of the excitation beam is shaped to a graph of 2D radially symmetric and identical Gaussian profiles by using a R-SLM and afterwards, it is focused on the sample with a 0.65 NA microscope objective. The resulting Gaussian profiles are characterised by a full width at half maximum (FWHM) of approximately $1-2\,\mu m$. The photoluminescence from the sample is collected through the GaAs substrate with a 0.42 NA microscope objective. Fourier-space and dispersion imaging are performed by projecting the Fourier-space at the slit of a 300 grooves/mm with $50\,\mu eV$ resolution. If not otherwise stated, the real-space spectral tomography is obtained with a tunable Fabry-Perot interferometer with a bandpass of $20\,\mu eV$ and a free spectral range of $2.5\,nm$.

5.2 Theoretical description

In a polariton graph, by increasing the excitation density, condensation occurs at the state with the phase configuration that carries the highest population [14]. This is a consequence of the bosonic nature of the condensation process: the probability to scatter into a particular state grows with its population. At condensation threshold, a macroscopic coherent state is formed described by a wavefunction $\Psi_g(\mathbf{r})$ which we model using the complex Ginzburg-Landau equation (cGLE), as described in section 2.3.2. We make the ansatz that the wavefunction of a graph of m vertices is given by the sum of m

individual wavefunction centred at the graph's nodes, $\Psi_g(\mathbf{r}) = \sum_{i=1}^{m} \Psi(|\mathbf{r} - \mathbf{r}_i|) \exp(i\theta_i)$ where θ_i and $\mathbf{r_i}$ are the phase and position of each condensate respectively. The number of polaritons reads:

$$\begin{aligned} \mathcal{N} &= \int |\Psi_g(\mathbf{r})| d\mathbf{r} = m\mathcal{N}_0 + \sum_{i<j} J_{ij} \cos(\theta_i - \theta_j) \\ J_{ij} &= \frac{1}{\pi} \int_0^\infty |\Psi(k)|^2 J_0(k|\mathbf{r_i} - \mathbf{r_j}|) k dk \\ \Psi(k) &= 2\pi \int_0^\infty \Psi(r) J_0(kr) r dr \\ \mathcal{N}_0 &= 2\pi \int_0^\infty |\Psi(r)|^2 r dr \end{aligned} \tag{5.1}$$

where J_0 is the zero order Bessel function of first kind, $\mathcal{N}_0$ and $\Psi(r)$ are the number of particles and the wavefunction for a single condensate. The oscillating behaviour of the Bessel function brings about the sign change in the coupling constant, J_{ij}. As a consequence, the coupling is expected to oscillate as a function of the condensate separation. Introducing a set of of classical spin associated to each graph node and defined as $\mathbf{S}_i = (\cos\theta_i, \sin\theta_i)$, we refer to the coupling terms to be ferromagnetic (antiferromagnetic) when J_{ij} is positive (negative) in analogy to magnetic systems.

The maximisation of the particles number is equivalent to minimise the XY Hamiltonian, $\mathcal{H}_{XY} = -\sum_{i<j}^{m} J_{ij} \cos\theta_{ij}$. Therefore, measuring the phase configuration of a polariton graph gives information of the global minimum of the XY Hamiltonian. As a result of the phase coupling across the graph, interference patterns form both in real- and Fourier-space. In simple graphs, the phase configuration can be interfere by counting the number of interference maxima between each pair of condensates, otherwise, for more complex coupling networks, it can be obtained by Fourier-space analysis and/or interferometric measurements.

5.3 1D Ising chain

We experimentally address an analogue of the Ising chain by projecting on the sample a linear chain of five equidistant polariton condensates. Due to the symmetry of the structure, the XY Hamiltonian reads $\mathcal{H}_{XY} = -4J\cos\Delta\theta$ where J and $\Delta\theta$ are the coupling and the phase difference between two nearest neighbour condensates respectively. Since the structure is open and the maximum connectivity is two, the system lacks of frustration and the relative phase between any pair or neighbours is either zero or π depending on the sign of J. As such, the linear chain configuration restricts the spin states effectively reducing the chain to the Ising model. Figure 5.1 shows the corresponding

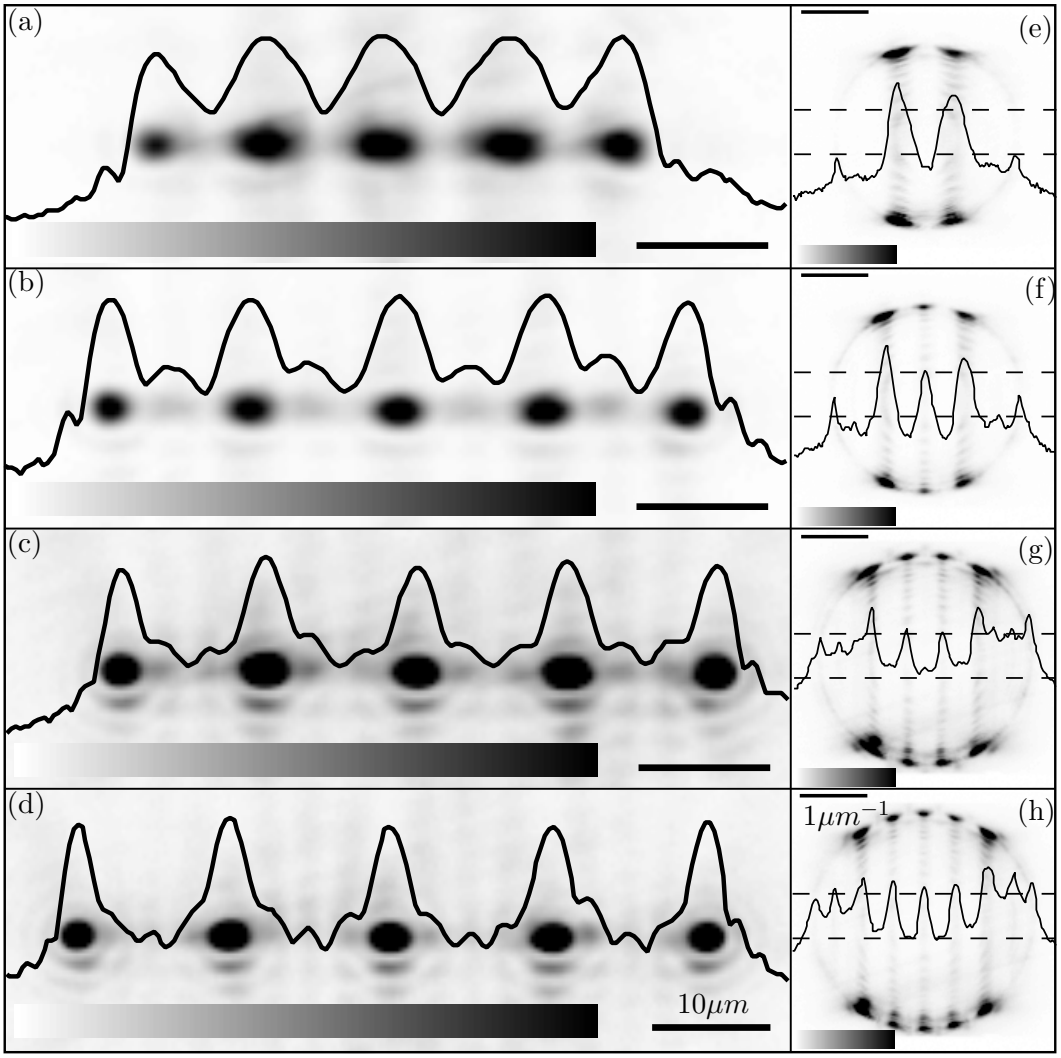

Figure 5.1: Experimental realisation of an Ising chain of five equidistant polariton nodes with lattice constant, condensation wavevector, (d, k_c), of $(9\,\mu m, 1.35\,\mu m^{-1})$ (a,e), $(11.1\,\mu m, 1.37\,\mu m^{-1})$ (b,f), $(11.4\,\mu m, , 1.56\,\mu m^{-1})$ (c,g) and $(13.4\,\mu m, , 1.39\,\mu m^{-1})$ (d,h) respectively. The outer ring radius in Fourier-space corresponds to the condensation wavevector, k_c, whereas the inner fringes correspond to self-diffraction from the Ising chain. The false-grey scale images show the normalised real- (a-d) and Fourier-space (e-h) photoluminescence intensity at the energy of the condensate; (a,b) are saturated at 0.7, (c,d) are saturated at 0.25 and (e-h) are saturated at 0.3 to increase the visibility of the low intensity fringes. Figure taken from reference [2].

real- and Fourier-space photoluminescence for different distances at condensation threshold. The phase configuration are clearly distinguishable in both real- and Fourier-space. In particular, an even (odd) number of density maxima between nearest neighbours in real-space is an unequivocal signature of anti-ferromagnetic (ferromagnetic) coupling. Similarly, the observation of a minimum (maximum) at $k_x = 0$ (where x is the chain direction) in the Fourier-space is typical of anti-ferromagnetic (ferromagnetic) coupling.

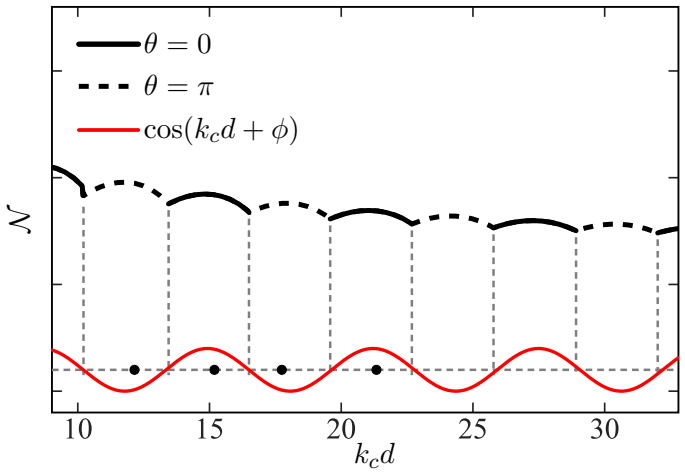

Figure 5.2: The maximum number of particles for a polariton dyad formed under incoherent pumping as a function of $k_c d$ for a fixed k_c obtained by numerically integration of the cGLE. The solid (dash) line corresponds to the ferromagnetic (anti-ferromagnetic) coupling. The switching occurs with a period of $2\pi/k_c$ as the superimposed graph of $\cos(k_c d + \phi)$ illustrated, with $\phi = 225^o$. The black dots are the experimental $k_c d$ corresponding to figure 5.1. Figure taken from reference [2].

Theoretically, solving the 1D Ising chain simplifies to calculate the phase configuration of two condensates, a polariton dyad, as a function of $k_c d$, as shown in figure 5.2. Remarkably, we obtained a perfect agreement between experiments (black dots) and theory (black line). As expected, the phase configuration at fixed condensation wavevector switches between zero and π with a period of $2\pi/k_c$, as shown by the superimposed cosine function (red curve). Nevertheless the cosine function reproduces the oscillating nature of the coupling term, a phase offset of 225^o is required to be consistent. The physical origin of the phase offset can be phenomenologically understood considering our description of the phase coupling which states that the system adjusts the relative phase so that ballistically exchanged polaritons are in-phase with the locally excited ones. As we assume that the acquired phase during the ballistic transport of polariton is $k_c d$, there are at least three factors which we neglect: (1) the finite size of polariton condensate, (2) the finite width of polariton emission and (3) the fact that polariton wavevector is not constant during the ballistic transport.

5.4 2D structures

Equidistance vertices across a circle

We consider a geometry of m polariton condensates regularly arranged across a circle. The XY Hamiltonian reads $\mathcal{H}_{XY} = -mJ\cos\Delta\theta$ where J and $\Delta\theta$ are the coupling and the phase difference between two nearest neighbour condensates and we consider

only first neighbour interaction. If the coupling term is positive, the trivial solution, $\Delta\theta = 0$, is always the ground state of the system. Otherwise, $\Delta\theta = \pi$ when m is even or $\Delta\theta = \pm\pi(m-1)/m$ when m is odd. In the latter case, the periodic boundary condition introduces frustration in the system. As a consequence, the ground state is two-fold degenerate and its phase configurations bring about topological vortices of charge $\pm(m-1)/2$ whose properties will be discussed in chapter 6.

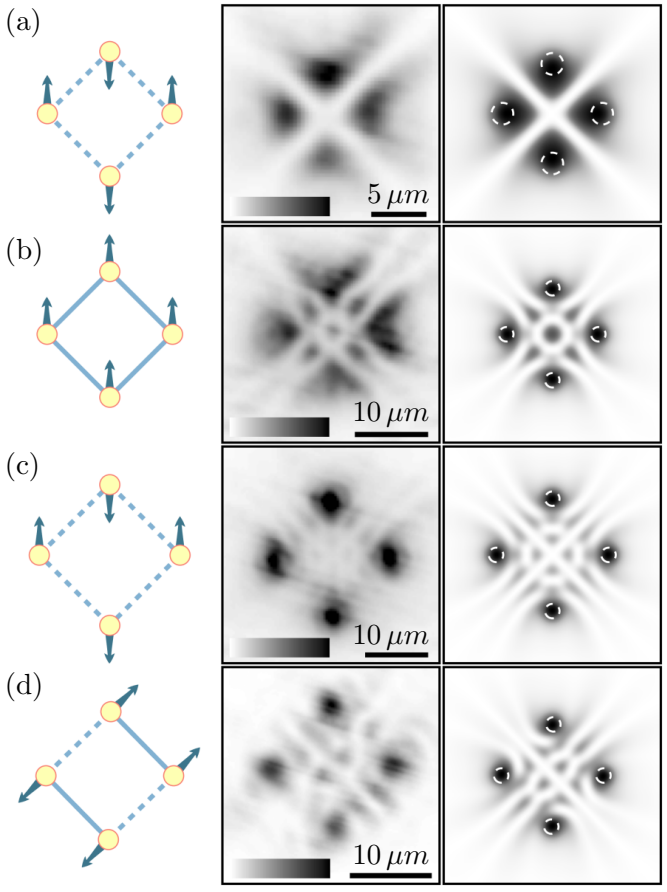

Figure 5.3: Spin configurations of square polariton lattices. The diagram of the numerically calculated spin vectors at the pumping site $\mathbf{S} = (\cos\theta_i, \sin\theta_i)$, the real-space energy tomography of the experimental realisations and the numerical results are shown on the left, central and right columns respectively. Solid and dashed blue lines on the spin vector diagram (left column) indicate ferromagnetic and anti-ferromagnetic coupling, respectively. The false-grey scale mages in the middle column shows the normalised real-space photoluminescence intensity at condensation threshold filtered though a Fabry-perot interferometer tuned at the energy of the condensate; (c) is saturated at 0.5 to increase the fringes visibility. The dashed white circles in the right column show the position of the centre of the pumping spots. The configurations shown are some elementary building blocks of square lattices such as anti-ferromagnetic (a,c), ferro-magnetic)b) and 90^o compass (d). Figure taken from reference [2].

Figures 5.3(a) to 5.3(c) show the spin configuration, experimental results of the real-space photoluminescence intensity at the energy of the condensate at condensation

threshold and numerical simulations for a square with lattice constants that lead to anti-ferromagnetic, ferromagnetic and the next anti-ferromagnetic coupling respectively. Similar to the Ising polariton chain, the type of coupling is clearly distinguishable by the number of fringes between vertices: even for anti-ferromagnetic and odd for ferromagnetic. These observation are in agreements with the π phase difference reported in reference [77].

In the context of solving universal spin models, more complex and exotic coupling configurations than fully anti-ferromagnetic or ferromagnetic couplings are of interest, i.e. network of arbitrary couplings [161] and compass models where the coupling sign are inherently directionally dependent [162]. Polariton graphs can realise complex coupling configurations by introducing an asymmetry either in the excitation density or in the geometry. In figure 5.3(d), we realise the 90^o compass model, where each vertex has one ferromagnetic and one anti-ferromagnetic coupling with its nearest neighbours as it is clearly distinguishable by the number of fringes between nearest neighbours.

Rhombus

The XY Hamiltonian has been simulated on a triangular lattice of atomic condensates proving a rich variety of phase configurations [151]. Furthermore, in the case of three polariton condensates arranged at the vertices of an equilateral triangle under non-resonant pulsed excitation, the phase configuration has been observed to exhibit a transition in the time domain from a trivial phase configuration (positive coupling) to a frustrated one ($\Delta\theta = \pm 2\pi/3$) which correspond to single charged topological states of opposite charge [14].

Here, we experimentally realise a unit cell of a triangular lattice, in other words four polariton condensates in a rhombus configuration. The symmetry in the structures implies that both pairs of condensate laying on one of the rhombus diagonal are always in-phase regardless the coupling sign. Therefore, the XY Hamiltonian reads $\mathcal{H}_{XY} = -J(4\cos(\Delta\theta) - 1)$ where we neglect the interaction along the rhombus long diagonal. If J is positive, the trivial solution represents the ground state, otherwise, $\Delta\theta = \pi$ as in the square case. However, differently from the square unit cell, the rhombus anti-ferromagnetic configuration generates frustration even in the first neighbours approximation.

Figure 5.4 show the spin configuration, experimental results of the real-space photoluminescence intensity at the energy of the condensate at condensation threshold and numerical simulation for a rhombus with lattice constants that lead to anti-ferromagnetic, ferromagnetic and the next anti-ferromagnetic coupling, respectively. The anti-ferromagnetic configurations show a minimum at the centre of the rhombus, while the ferromagnetic one shows a maximum.

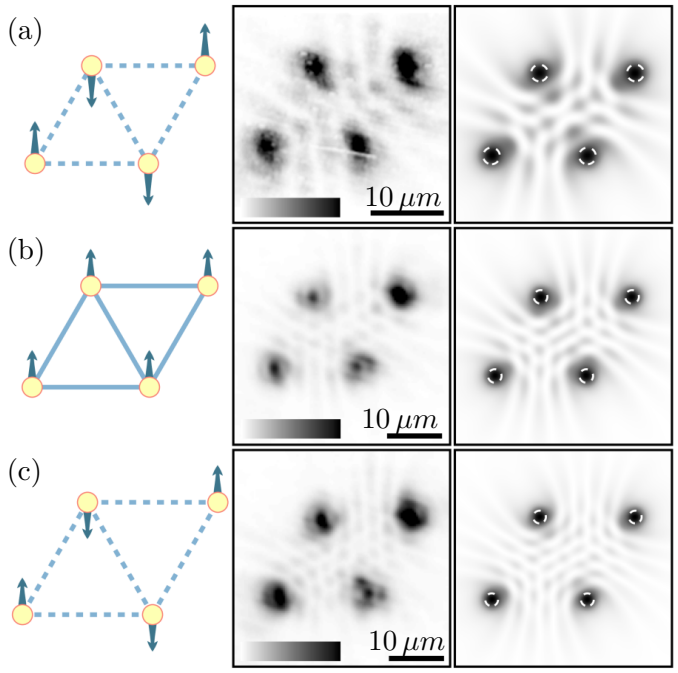

Figure 5.4: Spin configurations of rhombus polariton lattices. The columns of images are as described in the caption of figure 5.3. The configurations shown are some elementary building blocks of triangular lattices such as anti-ferromagnetic (a,c) and ferromagnetic (b). The middle column images are saturated at 0.5 to increase the fringe visibility. Figure taken from reference [2].

Random graph

Beyond solving the XY Hamiltonian for trivial cases, we test our platform on a disordered graph of five vertices. We start with a three adjacent equilateral triangular cells with anti-ferromagnetic coupling and then, we displace one of them out of position in order to break the regularity of the structure. Figure 5.5 shows the spin configuration, experimental results of the real-space tomography of the photoluminescence intensity at the energy of the condensate at condensation threshold and numerical simulation corresponding to this graph. For a periodic structure with only nearest neighbours interaction, the XY Hamiltonian is minimised at $\mathcal{H}_{XY} \sim 3.86J$ with alternating winding around each cell. The phase difference deviates from the $\pm 2\pi/3$ phase difference reported for a single equilateral cell [14] due to the different level of connectivity of each node. Breaking the symmetry leads to a different phase distribution while still maintaining the winding around each cell. The analysis of the fringes on the experimental image is the signature that the symmetry is explicty broken.

Extended polariton lattice

We dedicate this section to test the ability of our platform to search for the ground state with increasing the number of vertices. Firstly, we study a extended square polariton

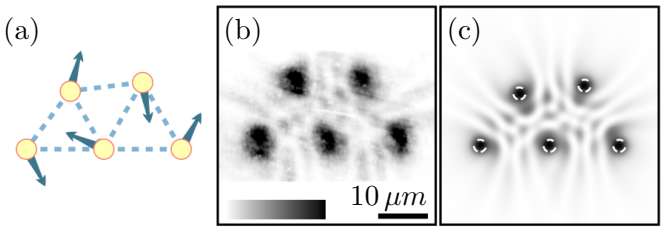

Figure 5.5: Spin configurations of a random polariton graph. The columns of images are as described in the caption of figure 5.3. The middle column images are saturated at 0.5 to increase the fringe visibility. Figure taken from reference [2].

lattices whose solution are known to be the same of a single unit cell previously discussed. Figure 5.6 shows the experimental results of the normalised real- (top) and Fourier-space (bottom) photoluminescence intensity at condensation threshold for 45 coupled condensates arranged on a regular square grid. The lattice constants chosen here result in anti-ferromagnetic, ferromagnetic and the next anti-ferromagnetic couplings respectively. In Fourier-space, sharp peaks appears which is a signature of the degree of coherence of the whole lattice in close analogy to Bragg peaks observed in X-ray scattering experiments. Similar to the single square unit cell, the phase configuration ca be clearly distinguished in real-space by counting the fringes parity between nearest neighbours. Alternatively, the observation of a bright peak at $k_{\|} = 0$ in Fourier-space is a clearer and an equivalent signature of ferromagnetic coupling, while an anti-ferromagnetic is characterised by four bright peaks centred around $k_{\|} = 0$ in Fourier-space.

The results discussed so far prove that the injected polariton lattices under steady-state excitation regime always condensate with the phase configuration that corresponds to the minimum of the corresponding bespoken XY Hamiltonian. Going beyond 45 condensates is currently limited by our laser source and the overall efficiency of our system. A possible route to overcome the power limitation is to switch to a pulse laser. A pulse laser provides an higher peak power but it is broader than a continuous-wave because of the Heisenberg principle and its output power strongly fluctuates due to mode competition. As a result, the emission pattern gets more complicated and it evolves in time/energy as already shown in reference [14].

We switched our laser source to a Ti:Sapphire pulsed laser with a pulse width of 200 fs and a repetition rate of 80 MHz to investigate a triangular polariton lattice. First, we re-address a graph of three condensates arranged at the vertices of a equilateral triangle, a polariton triad. Figures 5.7(a) and 5.7(b) show the experimental results of the normalised real-space photoluminescence intensity at the energies of condensation above condensation threshold. The lattice constant and power are chosen in order to observe a transition in time/energy from positive to negative coupling as a consequence of the relaxation time which causes a reduction of the condensation wavevector. In this case, the tomographic images are obtained with the motorised-mirror method described in

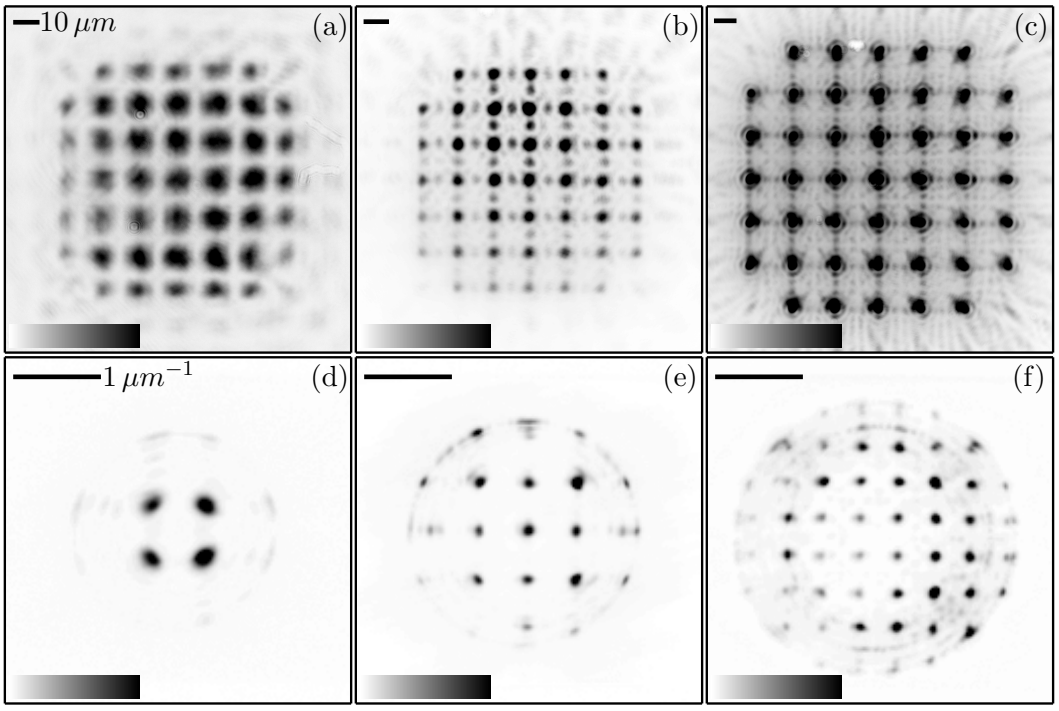

Figure 5.6: Real- (top) and Fourier-space (bottom) normalised photoluminescence intensity at condensation threshold of 45 polariton condensates. The lattice constants chosen realises the anti-ferromagnetic (a,d), ferromagnetic (b,e) and the next anti-ferromagnetic (c,f) configurations respectively. (a) is saturated at 07, (b,c,f) are saturated at 0.3 and (d,e) are saturated at 0.5 to enhance the fringes visibility. Figure taken from reference [2].

section 3.2.2. Similar to the previous case, the appearance of a maximum (minimum) in the centre of the structure is a feature of ferromagnetic (anti-ferromagnetic) coupling across the three condensates. Furthermore, we perform interferometric measurements to directly measure the phase shift between nearest neighbours by using a stabilised Michelson interferometer in retro-reflector geometry, as described in Reference [9]. In particular, the interferometer is aligned so that (1) the pictures of the two arms overlap with a displacement equal to half the distance between condensates as shown in figure 5.7(c) and (2) the fringes modulation occurs along the horizontal direction to achieve the best spatial resolution. The dashed lines in figure 5.7(d) show the normalised intensity profiles taken along the green line of figure 5.7(c) at the condensates energies corresponding to Figures 5.7(a) and 5.7(b). The shift of the fringes maxima is the signature that the two condensates change their relative phase which we calculated by fitting the profiles with a Gaussian multiply by a positive defined periodic oscillatory function (solid lines). The condensates at the two condensation energies shows a change in the relative phase of $(1.2 \pm 0.2)\pi$ which is consistent with the appearance of a pinned single-charged vortex in the middle of the structure in figure 5.7(b), as previously observed in similar experimental conditions on a different sample [14]. The displacement of the phase shift from the theoretical expected value of $\pm 2\pi/3$ and its pinning can be attributed to a small chirality induced in the pumping profile [163].

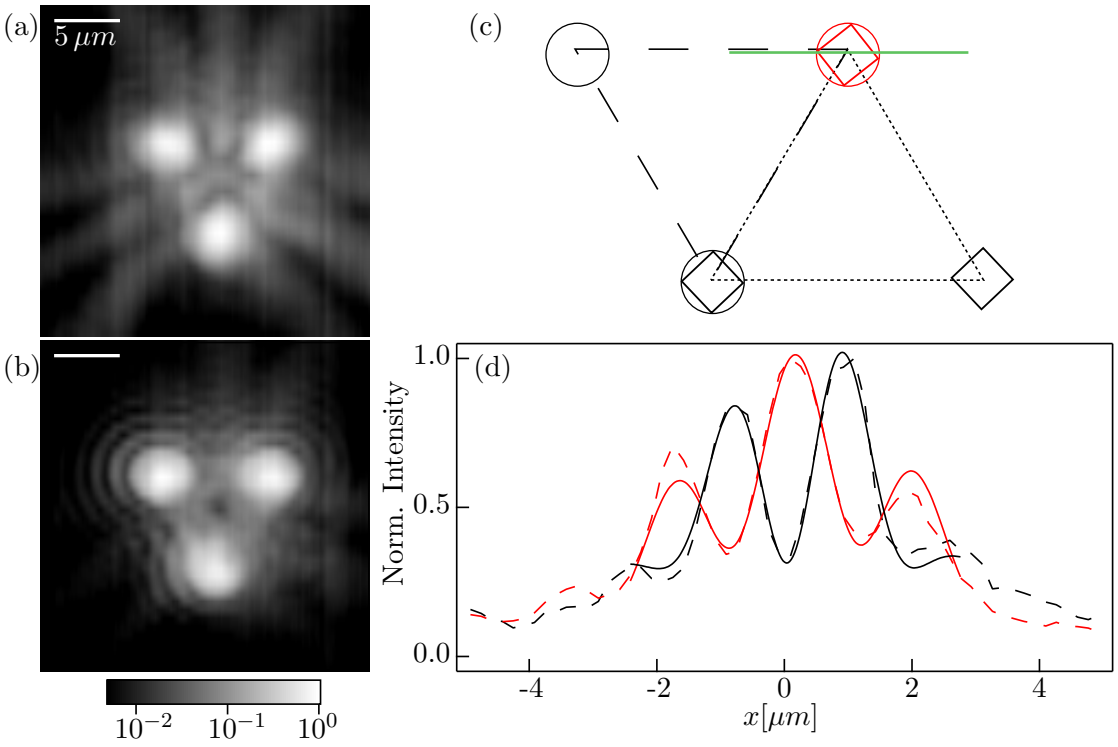

Figure 5.7: Normalised real-space photoluminescence intensity at the energies of condensation above condensation threshold for a polariton triad positively (a) and negatively (b) coupled respectively. (c) Schematic representation of the condensate position on the camera for the interferometric measurements. Squares (circles) indicate the position of the condensates in the retro-reflector (mirror) arm respectively. The red symbols indicates the condensates used to extract the phase shift between the two energy configuration of the triad. (d) Experimental profiles along the green lines in (c) (dashed lines) and fits (solid lines) at the energies corresponding of (a) (red) and (b) (black) obtained with a stabilised Michelson interferometry in a retro-reflector configuration. The shift of the fringes maxima shows a change in the relative phase between the two condensates of $(1.2 \pm 0.2)\pi$ consistent with the appearance of a pinned vortex in the core of the structure in figure (b).

Afterwards, we investigate a triangular polariton lattice of 100 condensates and, due to power limitation, we fed our pulsed laser into an amplifier system whose output has the same spatial and spectral shapes but with a repetition rate of approximately 100 KHz and a roughly 100 times amplification of the peak power. Figure 5.8 shows the experimental results of the normalised real- (left) and Fourier-space (right) photoluminescence intensity at the energies of condensation above condensation threshold. The lattice constant and power are chosen in order to observe a transition in time/energy from positive to negative coupling as a consequence of the relaxation time which causes a reduction of the condensation wavevector. In this case, the tomographic images are obtained with the motorised-mirror method described in section 3.2.2 due to anisotropy of the Fabry-Perot mirrors. Similar to the previous case of extended square lattice, it is more difficult

to distinguish the phase configuration in real- than Fourier-space, where the appearance of Bragg peaks and their position are a clear signature of both the coupling sign and also of the real-space lattice symmetry.

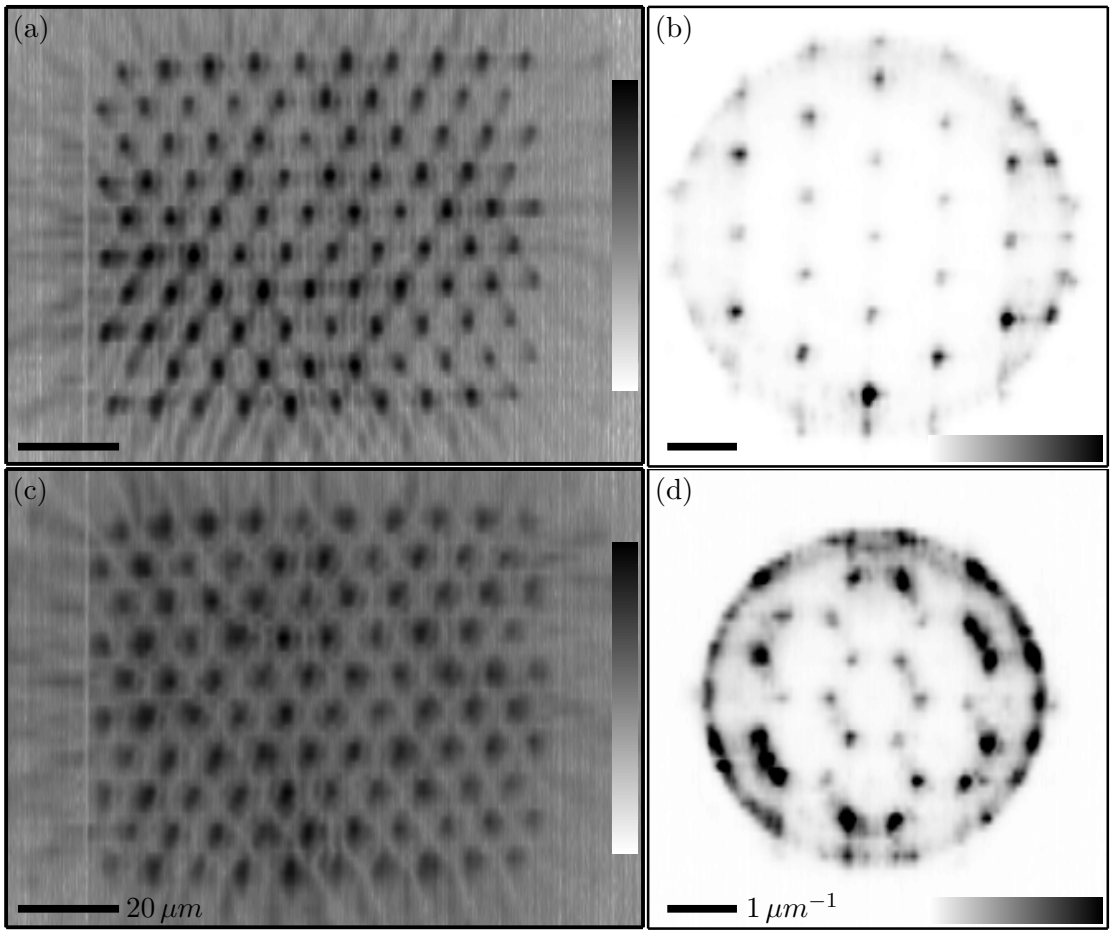

Figure 5.8: Real- (left) and Fourier-space (right) normalised photoluminescence intensity above condensation threshold at the condensates energies. The lattice constants chosen realises the next anti-ferromagnetic (a,b) and the next ferromagnetic (c,d). (a,c) are plotted in log colour scale and are lower saturated at 0.001, (b,d) are plotted in in linear colour scale and are upper saturated at 0.3.

5.5 Conclusions

In conclusions, we have theoretically proposed and experimentally demonstrated a new platform to simulate the classical XY Hamiltonian which we have tested with different 1D and 2D structures. We have proved that the coupling sign can be tuned either by the graph geometry and/or by the excitation profile of each node and different methods to measure the solution of the required problem have been introduced which relay on standard optical techniques. Furthermore, in comparison with annealing techniques, the

bottom-up approach here proposed to find the ground state ensures to reach the global minimum of the bespoken Hamiltonian without being trapped in local minima.

Some fundamental questions about our platform remains open requiring further work to determine the fundamental computation power of our platform, i.e. upper limit of coherently coupled vertices, level of connectivity and accuracy of finding the ground state for complex coupling networks. Nevertheless, the optical approach for both input and output is promising as it allows for tunable coupling strengths between vertices and rapid scalability utilising mature semiconductor and photonic technologies.

5.6 Contributions and Publications

The experiments reported in this chapter have been carried out by the the author, Dr. Pasquale Cilibrizzi, Dr. Alexis Askitopolos and Prof. Pavlos Lagoudakis. The theoretical simulations have been performed by Kirill Kalinin and Prof. Natalia Berloff. Where cited, data reported in this chapter have been published previously in Ref. [2].

Chapter 6

Vortices in polariton graphs

Quantised vortices (QVs) are fundamental topological objects which plays an important role in frictionless fluidic phenomena. Indeed, the appearance of vortex lines has been documented in rotating superfluid helium [164] and the formation in a lattice structure, the so-called *Abrikosov lattice* [165], lies at the heart of the partial Meissner effect observed in high-temperature superconductors [166].

The achievement of Bose-Einstein condensation in atomic gases [39–41] has offered a powerful tool to study superfluidity in an extremely clean and controlled environment which has been soon followed by the observation of quantised vortices by means of condensate stirring [167]. Multiple QVs are thermodynamically unstable in spinless, macroscopic and homogeneous superfluids because the vortex energy scales quadratically with the vortex charge, and therefore, they tends to break into arrays of single charged vortices [168]. However, several scheme have been proposed to stabilised multiple QVS, i.e. potential confinement stronger than harmonic one and fast rotation [169], but the observation of multiple QVs remain elusive [170]. In addition, multiple QVs have been reported in other superfluids, i.e. ^{3}He [171] and mesoscopic superconductors [172], but the experimental evidences are still not conclusive. Apart from quantised vortices that exist on a non-zero background, a new class of vortices was introduced theoretically and achieved experimentally in periodic photonic structures, the so-called *discrete vortex solitons* (DVSs) [173, 174]. DVSs are exponentially localised bright solitons with a vortex nested inside it and, contrary to optical vortices, they exist on a negligible background [175]. By engineering the input laser phase profile, stationary DVSs have been observed [176]. Similarly, topological charge can spontaneously occur either as excited or ground state of ring networks with equal couplings across nearest neighbour nodes [177–179]. In these setting, the phase winding manifest itself only as a phase winding around these sites and, therefore, it does not result in the formation of a nonlinear vortex.

In this chapter, I discuss the preliminary results in the realisation of a crossbreeds of DVSs and giant vortices in a graph of polariton condensates. One one side, they shows

a discrete phase different between nearest condensates as optical DVSs, but the phase winding spontaneously forms under non-resonant excitation through bosonic stimulation. In this respect, they are closer to vortices in atomic condensates but, as we demonstrate, they do no require any rotation and even multiple charged vortices are fully stabilised by the ballistic exchanged of polariton across sites.

6.1 Experimental method

The setup is described in section 5.1. Here, we consider polariton graphs where each node occupies the vertex of a regular polygon. Figure 6.1 shows a schematic of the expected density profile of an heptagon of polariton condensates with anti-ferromagnetic coupling.

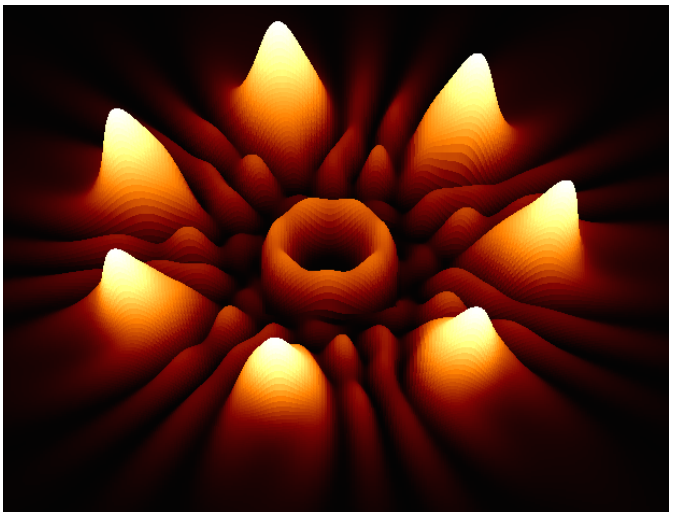

Figure 6.1: Schematic density profile of an regular heptagon of polariton condensates with anti-ferromagnetic coupling between its vertices. Within the inner ring visible at the centre of the structure, a giant vortex occurs that is fully contained within the inner ring. Figure taken from reference [4].

6.2 Theoretical description

The theoretical description is discussed in 5.2. The XY Hamiltonian for a regular vertices polygon reads $\mathcal{H}_{XY} = -mJ\cos\Delta\theta$ where m is the number of vertices of the polygon, J is the coupling between nearest neighbours and $\Delta\theta$ is the phase difference between any pair of nearest condensates. It is worth mentioning that polygon structures are constrained by periodic boundary conditions.

6.3 Regular polygons

As discussed in section 5.3, the coupling across polariton condensates is determined by the adimensional parameter $k_c d$, where k_c is the condensation wavevector and d is the condensate separation. It has already been shown that, under pulsed excitation and for a fixed geometry, a polariton triad can exhibit a transition from ferromagnetic to anti-ferromagnetic coupling which corresponds to a transition from the trivial phase configuration to a topologically charged one [14]. This result has been reproduced as a preliminary work at the beginning of my PhD and it is presented in section 5.4 . As we are interested in stationary states, we engineer the coupling strength and sign by tuning the distance across sites.

Firstly, we experimentally realise the ferromagnetic configuration for different polygons where the trivial phase configuration minimises the corresponding XY Hamiltonian. Figure 6.2 shows the experimental results of the real-space photoluminescence of ferromagnetic coupled polygons of even and odd number of vertices. The ferromagnetic configuration is clearly distinguishable from the number of fringes between each condensate pair and by the appearance of a density maximum at the core of the structure.

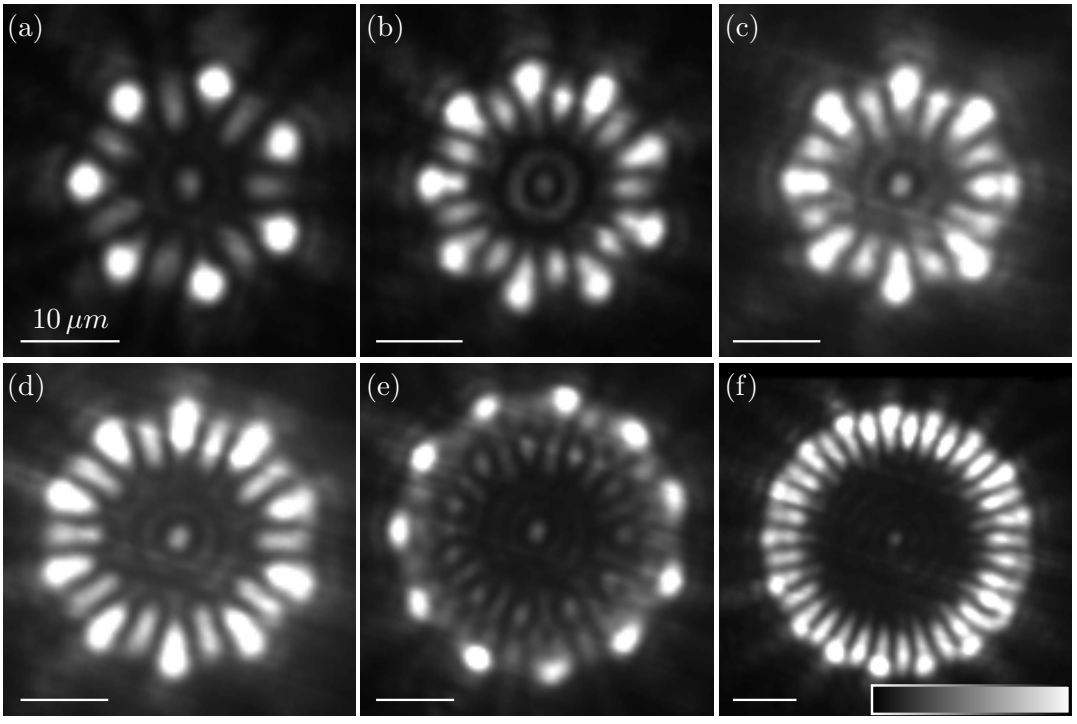

Figure 6.2: Normalised real-space photoluminescence intensity at condensation threshold for polygons of seven (a), height (b), nine (c), ten (d), eleven (e) and seventeen (f) vertices ferromagnetic coupled. Figures are plotted in linear colour scale saturated at 0.5 to enhance the fringes visibility. Figures 6.2(b) and 6.2(c) taken from reference [4].

Figure 6.3 shows the result of the numerical simulation for an octagon and a nonagon polariton graph which corresponds to the experimental realisation of Figures 6.2(b) and 6.2(c) proving a good agreement.

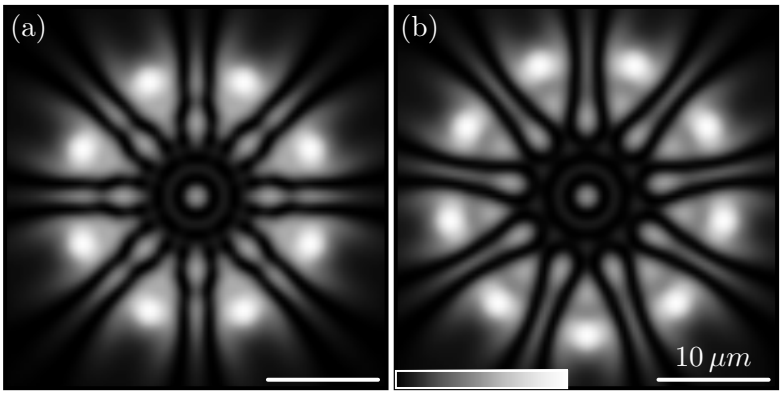

Figure 6.3: Numerical simulation of the density profiles for polygons of 8 (a) and 9 (b) vertices ferromagnetic coupled corresponding to Figures 6.2(b) and 6.2(c). Figure taken from reference [4].

Next, we tune the condensates separation to achieve anti-ferromagnetic coupling between nearest neighbours. Figure 6.4 summaries the experimental results and numerical simulation for polygons with even number of vertices where the anti-phase configuration minimises the corresponding XY Hamiltonian, in particular we investigate an octagon and a decagon. As usual, the parity and symmetry of the fringes between any pair of nearest neighbours in real-space (left column) is a clear manifestation of the anti-ferromagnetic coupling across the structure. Furthermore, the phase configuration is clearly distinguishable by the observation of a photoluminescence minimum at both the centre of the structure in real-space and also at the centre of Fourier-space (central column). We note that Fourier-space is divided into circular sectors by nodal radial lines crossing its centre. Therefore, as expected, this configuration does not correspond to the formation of a vortex localised at the centre of the structure since the latter requires a continuous flow of polaritons along a ring concentric to the polygon. In the right column, we further prove the absence of a vortex in the middle of the structure by plotting the velocity stream lines and the zeros of the real and imaginary parts of the numerically evaluated wavefunction. Evidently, there is no velocity circulation around the centre. In conclusions, we demonstrate that an even polygon anti-ferromagnetic coupled cannot form a vortex in its core but this result does not prevents single quantised vortices to appear away from the structure centre.

The most interesting configuration is predicted for a graph of polariton condensates anti-ferromagnetic coupled arranged at the vertices of a regular polygon with an odd number of vertices. In this case, the system is frustrated because the anti-phase configuration is not self-consistent due to the periodic boundary condition. As a consequence, the phase

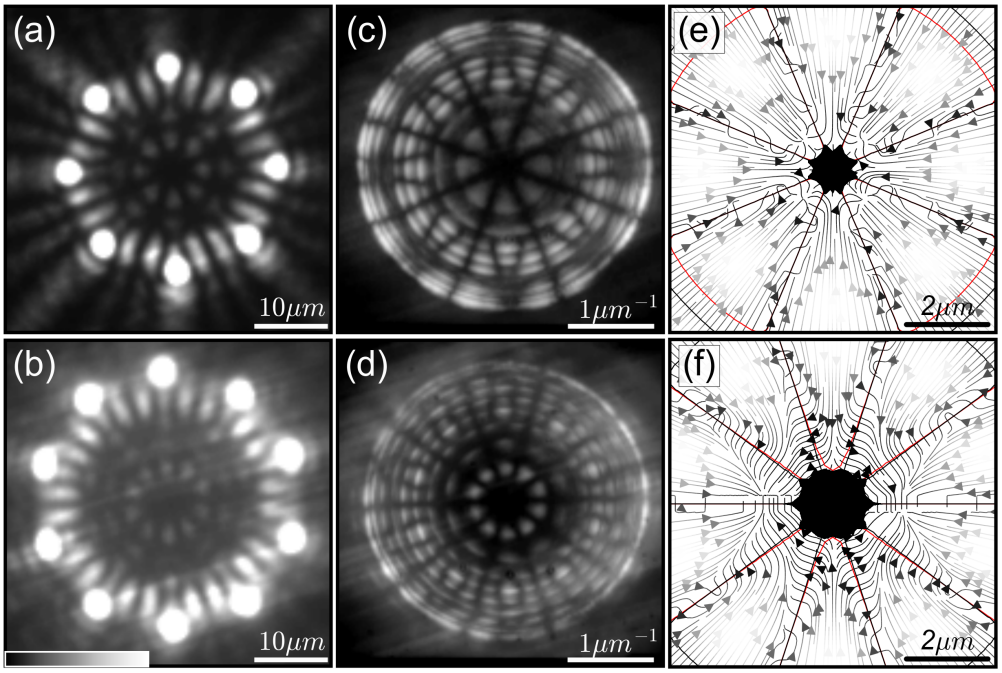

Figure 6.4: Experimental real- (left) and Fourier-space (centre) normalised photoluminescence intensity at condensation threshold for an octagon (top) and a decagon (bottom) with anti-ferromagnetic coupling between nearest neighbours. (right) Corresponding numerically evaluated velocity stream-lines and zeros of the real and imaginary parts of the wavefunction (red and black solid lines).The black filled area in (e,f) indicates the areas where the polariton density is less than 10^{-5} of its maximum. (a,b) are plotted in linear colour scale saturated at 0.2 and 0.25 respectively, and (c,d) are plotted in logarithmic scale saturated at 0.005 and 0.03 respectively to enhance the fringes visibility. Figure taken from reference [4].

configuration that minimised the corresponding XY Hamiltonian is topologically non-trivial with a charge of $\pm(m-1)/2$ where m is the number of the vertices of the polygon. Figure 6.5 summarised the experimental measurements and theoretical simulations for seven (top row), nine (middle row) and eleven (bottom row) condensates respectively arranged at the vertices of regular polygons at condensation threshold. Similar to figure 6.4, both real- (left column) and Fourier-space (central column) bring about the signatures of anti-ferromagnetic coupling but they show some differences. In particular, we observe no radial nodal lines in Fourier-space and the density minimum at the centre or real space is surrounded by a bring and continuos ring which are both signature of the formation of vortices in the middle of the structure. As before, we plot in the right column the corresponding velocity stream-lines and the zeros of the real and imaginary parts of the numerically evaluated wavefunction that show the velocity circulation around the structure core.

Our experimental observation and numerical simulations provide a preliminary evidence for the presence of multiple charged vortices of winding number ± 3, ± 4 and ± 5 in the core of a heptagon, nonagon and hendecagon polariton graph respectively. In the

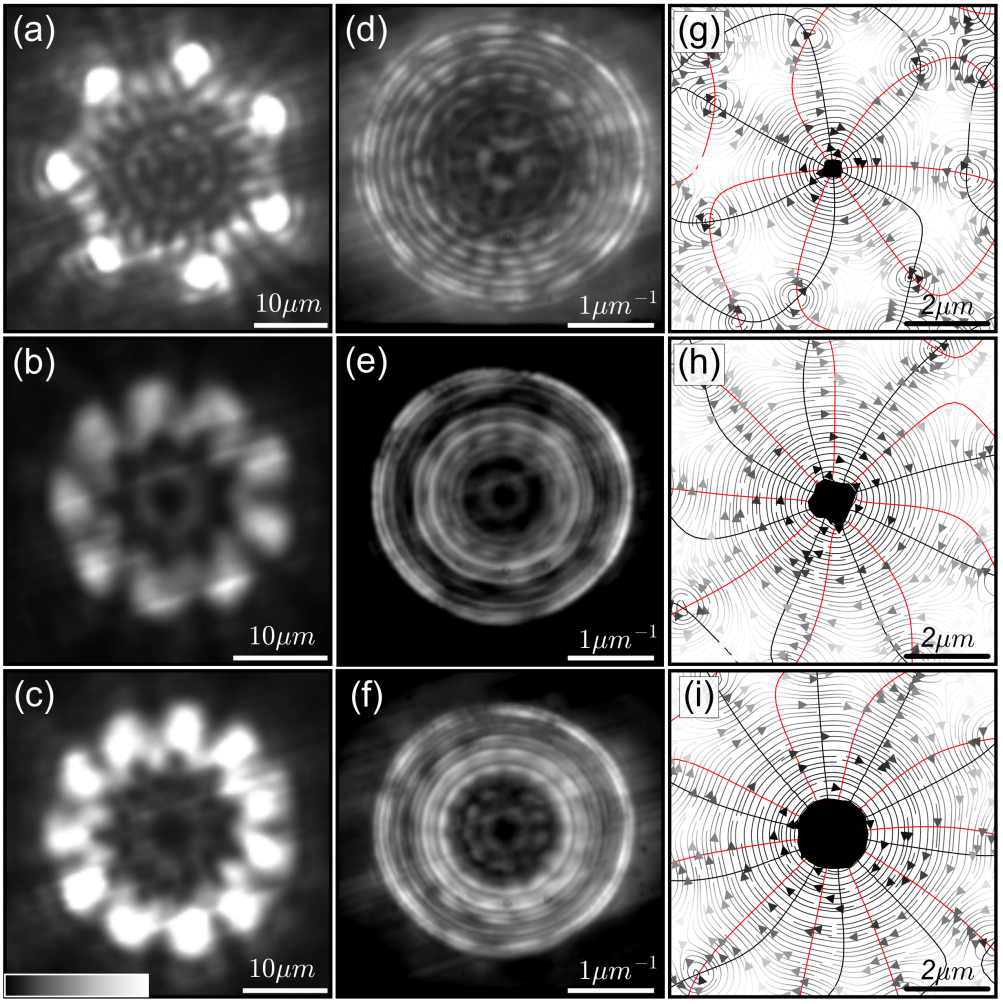

Figure 6.5: Realisation of heptagon, octagon and nonagon in a polariton graph. The columns of images are as described in the caption of figure 6.4. (a,c) are saturated at 0.2 and 0.5 respectively, (d-f) are plotted in a logarithmic colour scale and are saturated at 0.01, 0.02 and 0.025 respectively to enhance the fringe visibility. Figure taken from reference [4].

following, we provide further proofs on support of our claim by resolving the spatial phase distribution around the vortex core using off-axis digital holography [71]. Therefore, we measure the interference pattern of the vortex core with a reference phase profile in a stabilised Mach-Zehnder interferometer where we use as reference phase one condensates forming the structure tenfold magnified. It is worth remember that the ground state of these structures is two-fold degenerate corresponding to the formation of a vortex or an anti-vortex. Whereas vortex formation stochastically results in clock- or anti-clockwise winding of the phase across our polygon, we are expected to record an average of them as the acquisition time is much longer than the polariton coherence time. However, any chirality in the excitation pattern and/or any anisotropic defect in the polariton flow may pin vortices in one of the two directions. Figure 6.6 shows the experimental results (1st and 3rd rows) and numerical simulations (2nd and 4th rows) for the case of a heptagon (1st and 2nd rows) and a nonagon (3rd and 4th rows). The interference

patterns, the extracted phase profiles obtained by off-axis digital holography inside the white dashed square as illustrated in the first column and the phase extracted along the green circles illustrated in the central column are shown in the left, central and right columns respectively. Eventually, our measurements, corroborated by our numerical results, provide further insights but not conclusive that we observe an averaged vortex of multiplicity 3 in the centre of our heptagon and a pinned vortex of multiplicity 4 for our nonagon.

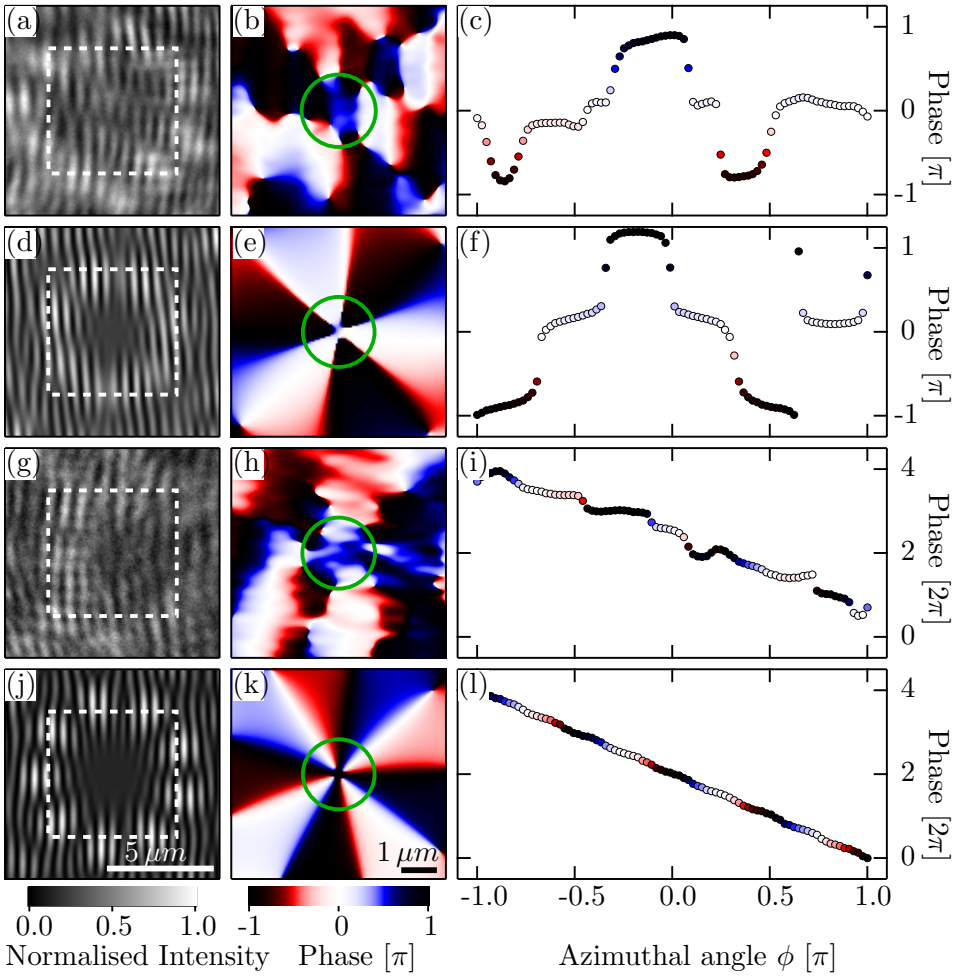

Figure 6.6: First column: experimental (1st and 3rd rows) and theoretical (2nd and 4th rows) interference patterns of the vortex core of an heptagon (1st and 2nd rows) and of a nonagon (3rd and 4th rows) with one of its condensates tenfold magnified obtained in a stabilised Mach-Zehnder interferometry. Central column: extracted phase obtained by off-axis digital holography inside the dashed white square illustrated in the first column. Right column: phase extracted along the green circle which encloses the structure centre as illustrated in the central column. Each phase in the graphs on the right column is colour coded to colour scale of the phase map. (c,f) shows six π step-like jumps in the phase profile which is consistent with the observation of a averaged vortices of opposite charge. (i,l) shows a more gradual change of the phase profile along the azimuthal direction which may be associated to a pin vortices of charge 4. Figure taken from reference [4].

6.4 Conclusions

In conclusions, we have presented the study of polygons of polariton condensates with both ferromagnetic and anti-ferromagnetic coupling. We have demonstrated, as expected, that the all condensates are in-phase phase when the nearest neighbours coupling is ferromagnetic regardless of the polygon type and that even polygons anti-ferromagnetic coupled do not lead to the formation of vorticity because the structure lacks of frustration. We have also provided the first preliminary results concerning the formation of stable, spontaneous and multiple charged QVs driven by geometrical frustration in odd polygon anti-ferromagnetic coupled. It is fairly to say that the results obtained so far are not conclusive concerning the observation of QVs as neither the interferometry measurements are clear enough, nor a complete study and understanding has been done to justify the appearance of a pinned or unpinned QV.

It is worth mentioning that m different solutions satisfy the periodic boundary condition of a polygon of m vertices and they are characterised by a phase shift between nearest neighbours of $2\pi n/m$ where n is an integer. Therefore, any polygon can sustain topologically charged solution but most solutions does not represents a maximum of the polariton density which is the driven mechanism of our system. A possible and fascinating route to unlock such configurations would be a more complex engineer of the coupling terms which can be achieved by exploiting the spin degree of freedom and/or by engineer a non-negligible next neighbours interaction.

6.5 Contributions and Publications

The experiments reported in this chapter have been carried out by the the author, Julian Töpfer and Prof. Pavlos Lagoudakis. The theoretical simulations have been performed by Kirill Kalinin and Prof. Natalia Berloff. Some data reported in this chapter are currently under peer review, Ref. [4].

Chapter 7

Polariton dyad coupling

A polariton graph is a set of spatially separated condensates which are divided in two classes: those where polariton condensates are spatially confined and those where they can freely expand in the cavity plane. Coupling between confined condensates occurs though quantum tunneling, i.e. Josephson coupling between two nearby defect sites [12]. Spatially confined polariton graphs have been intensively studied in regular structures using different photon confinement methods such as intracavity mesas [180, 181], etching micropillars [182, 183] and changes of the photonic boundary conditions via deposition of a metallic epilayer mesh [184–188]. Alongside these fabrication methods, the strong inter-particles interaction of polaritons enables to imprint arbitrary and reconfigurable trapping potentials by exploiting the optical malleability of the potential landscape felt by polaritons. When the potential landscape is made of spatially separated spots arranged in a close loop, as the nearest neighbours separation is increased, the system undergoes a geometry-driven phase transition switching from the formation of a single trapped condensate in the middle of the structure to a coherent phase locking of multiple condensates [15]. In the trapping regime, the interaction between trapped condensates is governed by Josephson coupling mechanism which -with an appropriate choice of the excitation condition- induces a stable spin correlation between confined condensates [189, 190]. For separation distances above the criticality for polariton trapping, each condensate arranges its phase to maximise the total density of polaritons through stimulated relaxation and -under pulse excitation- different phase configurations can manifest themselves during the relaxation process on a few picoseconds timescale [14].

In chapters 5 and 6, I have presented the mapping of the XY Hamiltonian to a bespoken freely expanding polariton graph. Up to now, we have studied regular structures where the nearest neighbours approximation holds and all the coupling terms are equal, namely $J_{ij} = J \ \forall i, j$. Therefore, the phase configuration is completely determines by the coupling sign regardless its magnitude. However, engineering a complex network of couplings is necessary for mapping high-complexity optimisation tasks [191].

In this chapter, I present a detailed study of the coupling mechanism between two spatially separated polariton condensates, hereafter referred to as a *polariton dyad*, in the absence of a potential barrier. Here, we propose a method to quantify the dyad coupling energy which represents an essential ingredient to develop a recipe of how to map the optimisation problem of interest to its corresponding polariton graph. Lastly, I also discuss some preliminary results about how to exploit the polariton spin degree of freedom to further engineer the coupling network in a polariton graph.

7.1 Experimental method

The setup is described in section 5.1. Firstly, we consider a polariton graph made of two co-circularly polarised, identical and radially symmetric Gaussian profiles for a set of relative distances from $7.5\,\mu m$ to $47\,\mu m$. At the end of the chapter, we study the dyad coupling at a fix distance as a function of the polarisation of one of the two Gaussian profile. The latter measurements have been performed using the extended arm of the setup shown in figure 3.9.

7.2 Theoretical description

The theoretical description is discussed in section 5.2. The XY Hamiltonian for a polariton dyad is simply $\mathcal{H}_{XY} = -J\cos\Delta\theta$ where J is the dyad coupling and $\Delta\theta$ is the phase difference of the two condensates forming the dyad. As discussed in section 5.3, the system symmetry limits the phase configuration to be either zero, if $J > 0$, or π, if $J < 0$.

7.3 Dyad coupling

We investigate the sign and strength of coupling across a polariton dyad by recording both real- and Fourier-space images at condensation threshold for a continuously varying separation distance in the range from $7.5\,\mu m$ to $47\,\mu m$ where we observe 19 abrupt alternations between in-phase and anti-phase phase configuration as it was previously observed in reference [14] but now in the steady state regime. During these measurements, we fix the excitation density to the condensation density for the longest separation distance we can observe coherent coupling across a dyad, here $47\,\mu m$. Figure 7.1 shows three snapshots of the real- and Fourier-space intensity profiles (top) and their corresponding numerical simulations (bottom) for separation distances which -with the usual mapping of the condensates relative phases to classical spins- corresponding to

anti-ferromagnetic, ferromagnetic and next anti-ferromagnetic coupling. The phase configuration is clearly distinguishable both in real- and Fourier-space as already discussed in section 5.3.

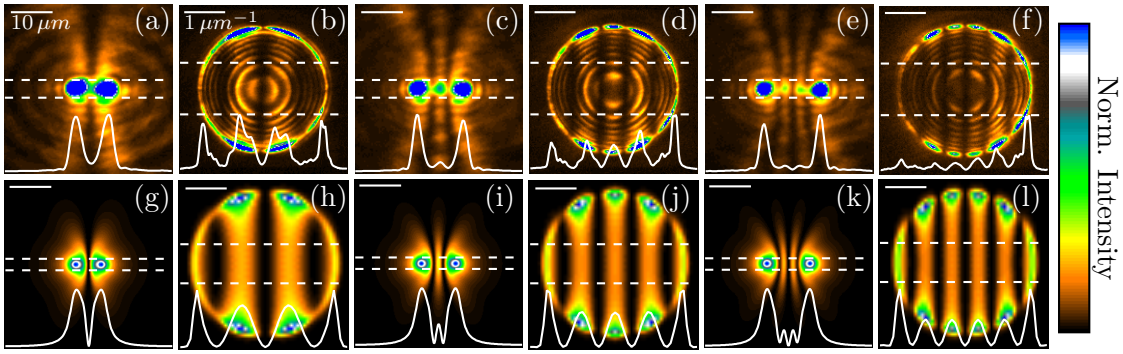

Figure 7.1: **Upper row:** Experimental real (a,c,e) and Fourier (b,d,f) space normalized intensities for polariton dyads at separation distances equal to 7.5 μm (a-b), 10.9 μm (c-d) and 13.4 μm (e-f) between the two condensates. Figures a-c-e and b-d-f are saturated respectively at 0.2 and 0.3 to enhance the pattern visibility. The solid white lines correspond to the horizontal integrated intensity profiles extracted from the regions delimited by the white dashed lines. In real space the parity of the interference fringes between the two condensates is correlated with the phase configuration of the dyad: AF for an even number of fringes (a,e), or F for an odd number (c). In Fourier space, the profiles show respectively a minimum (maximum) at k=0 for the AF (F) configuration (b,d,f). **Lower row:** Real and Fourier space time-integrated results of numerical simulations of the cGL equations at separation distances equal to 6.5 μm (g-h), 8.5 μm (i-j) and 10.5 μm (k-l). Figure taken from reference [3].

Upon non-resonant excitation, polariton states are populated though the relaxation process and, as a by-product, the exciton reservoir is formed as well. For separation distance above the trapping criticality, condensation occurs where the exciton density is maximum. Therefore, due to the strong inter-particles interaction, condensed polaritons sit on top of a potential hill whose height scales predominantly with the exciton density [137]. While the exciton cloud is strongly localised at the pumping site due to the exciton heavy mass, condensate polaritons ballistically expand away from the pumping area converting their potential energy into kinetic one. In the case of a polariton dyad, freely expanding polaritons from either condensates act as a source to one another. With increasing separation distance, the relative strength of the mutual resonant pumping decays exponentially due to the cavity lifetime, τ, while the sign of the coupling is expected to switch sinusoidally due to the ballistic nature of the expansion. Thus, the dyad coupling, J, is expected to scales as $J \propto \exp(-t/\tau)\cos(\tilde{\omega}\, t + \phi)$, where t is the time of flight from one condensate to the other and ω is a constant that depends on the dynamics of the polariton motion. The time of flight can be evaluated from $t = \frac{1}{2}\int_{x_1}^{x_2} \sqrt{\frac{2m^*}{E-V(x)}}$, where m^* is the polariton effective mass, x_i is the position of the

i-th condensate, E and $V(x)$ are respectively the total and potential energy of polaritons. Figure 7.2(a) shows the calculated time of flight as a function of the product of the condensates wavevector, k_c, and the condensates separation, $d = |x_1 - x_2|$, obtained by numerical integration where $E = \hbar^2 k_c^2 / 2m^*$, m^* is obtained by a parabolic fitting of the experimental dispersion in the linear regime and $V(x) = E \times f(x)$ where $f(x)$ is approximated by the experimental real-space intensity profile along the dyad axis, i.e. solid white lines in figure 7.1(a). Due to the accelerated motion of polariton propagating in a non-constant potential landscape, the time of flight results approximately proportional to $k_c d$, as shown in figure 7.2(a). Therefore, we expect a function dependence of $J = J(k_c d) \propto \exp(-\gamma k_c d) \times \cos(\omega k_c d + \phi)$. Remarkably, the coupling obtained numerically by means of equation 5.1 results in good agreement with the just derived phenomenologically functional behaviour, as it is shown in figure. 7.2(b).

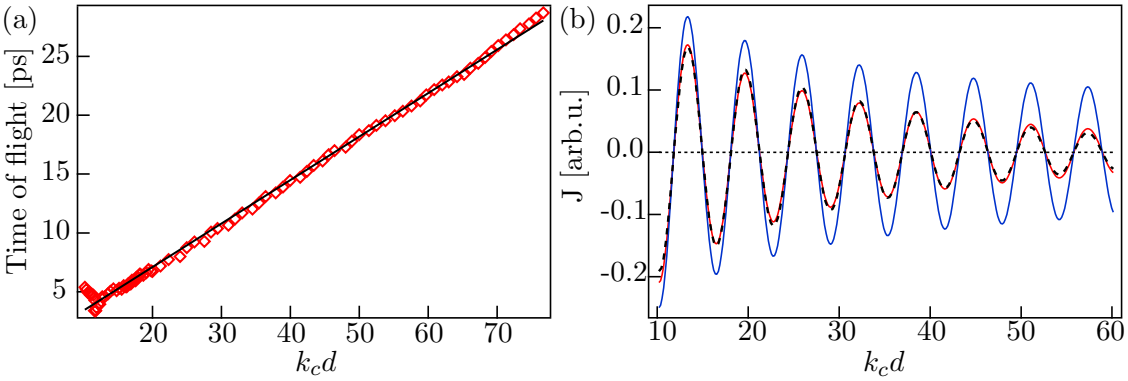

Figure 7.2: (a) Polariton dyad time of flight numerically evaluated (red square) and corresponding linear fit (black line) as a function of $k_c d$. Polariton dyad coupling numerically evaluated by solving equation 5.1 (solid lines). The blue line corresponds to the case where the dyad emission in Fourier-space is a delta function, the red lines corresponds to the case where the dyad wavefunction is approximated as the sum of two single condensate wavefunctions as discussed in section 5.2 which results nicely fitted by an oscillating exponential function (black dashed line). Figure taken from reference [3].

In the following, we keep the condensate wavevector virtually constant by retaining the two Gaussian intensity profiles unchanged, while changing the separation distance between the two pump spots. We record dispersion images for the full range of separation distances, where we observe coherent coupling, ranging from $7.5\,\mu m$ to $47\,\mu m$. Figures 7.3(a) and 7.3(b) show the dispersion images for separation distance of $7.5\,\mu m$ and $47\,\mu m$. Figure 7.3(c) shows the normalised energy profiles of Figures 7.3(a) and 7.3(b) integrated over $\left|k_{\|}\right| < 1.28\,\mu m^{-1}$, where we resolve an energy shift of approximately $250\,\mu eV$. Figure 7.3(d) shows the complete set of the normalised profiles of the dispersion images along $k_{\|}$ integrated over $E = 1.4478\,eV \pm 0.4\,meV$, where we observe a minimal change of k_c vs separation distance. At the same time we note the alternation

of ferromagnetic/anti-ferromagnetic coupling characterised by a maximum/minimum of the intensity at $k_{\|} = 0$ respectively.

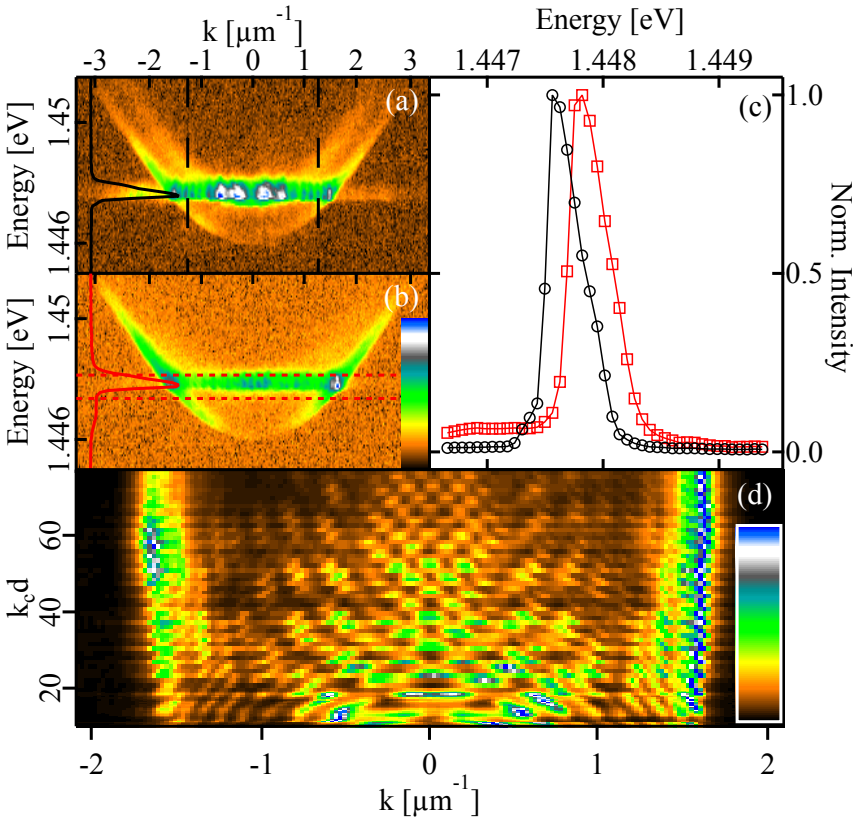

Figure 7.3: Normalised dyad dispersion images at a separation distances of $7.5\,\mu m$ (a) to $47\,\mu m$ (b). The colour scales are both logarithmic and saturated at 0.001. (a) corresponds to the AF phase configuration shown in Figures 7.1(a) and 7.1(b). The solid lines are the spectra integrated over $\left|k_{\|}\right| < 1.28\,\mu m^{-1}$, the area delimited by the dashed lines in figure (a). (c) Normalized integrated spectra comparison (markers): the photoluminescence emission of (a) is red-shifted of approximately $250\,\mu eV$ in respect to (b). The solid lines are guides for the eye. (d) Normalised Fourier-space profiles as a function of $k_c d$ integrated over $E = 1.4478\,eV \pm 0.4\,meV$, the area delimited by the dotted lines in (b). The colour scale is linear and the image is not saturated. The observation of a maximum (minimum) at $k = 0$ indicates ferromagnetic (anti-ferromagnetic) coupling across the dyad. Figure taken from reference [3].

Experimentally, we observe an exponential growth of the dyad energy, $E(k_c d)$, which saturates at $E(\infty) = 1.4479\,eV$ corresponding to a dyad whose coupling is negligible. Therefore, we define the coupling amplitude for a dyad of separation distance d as

$$|J| = E(\infty) - E(k_c d) \tag{7.1}$$

where $E(k_c d)$ is calculated with a Gaussian fit of the energy profiles obtained as in figure 7.3(c). Figure 7.4(a) shows the amplitude of the dyad coupling as a function

of $k_c d$ using equation 7.1 which reveals an oscillatory decay in agreement with the expected functional form but the oscillations amplitude is reduced. The black lines are fitting curves resulting in $\gamma = 0.05 \pm 0.005$ and $\omega = 1.1 \pm 0.1$. As previously discussed, the sign of the coupling determines the dyad configuration and it depends only on the sign of the cosine function. When $\beta = k_c d + \phi = \pm\pi/2$, the coupling is expected to annihilate but the experimental β broadens due to the finite emission linewidth, Δk and the finite dimension of the condensates, Δd, so that every dyad configuration is the average of different β weighted on the corresponding polariton population. In this light, a dyad configuration is experimentally well defined when $\cos(\beta)$ has a defined sign for $\beta = (k \pm \Delta k)(d \pm \Delta d) + \phi$, otherwise the state is a mixture of the in-phase and anti-phase configurations. In particular, when β is centred at $\pm\pi/2$, polaritons evenly contribute to both configurations preventing the experimental oscillation to reach the zero line.

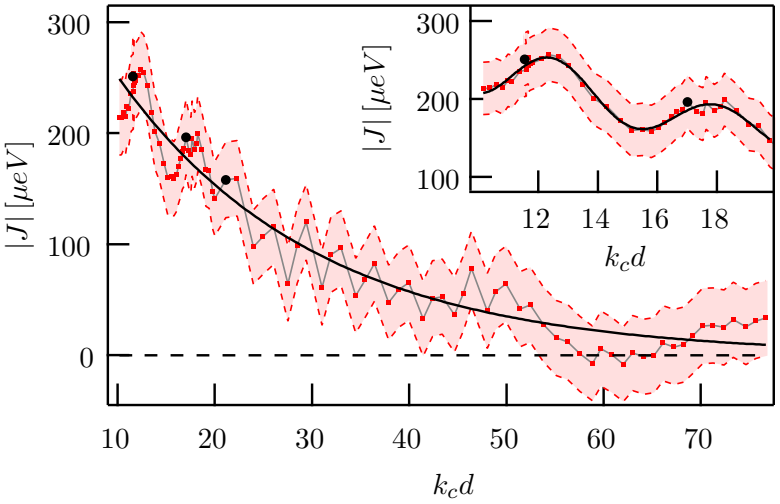

Figure 7.4: Experimentally amplitude of the coupling strength, $|J|$, (red points) as a function of $k_c d$ calculated by mean of equation 7.1.The exponential fit results in a decay constant of 0.05 ± 0.005. The inset is a zoomed region showing the oscillating trend of the curve with a oscillating frequency of 1.1 ± 0.1. The light red filled region include the error bars for each point. Error-bars are calculated as, $\Delta E(k_c d) = \sqrt{\delta E_1^2 + \delta E_2^2}$ where δE_1 is the digital resolution of the spectrometer, here $35 \mu eV$, and δE_2 is the fitting error of $E(k_c d)$. Black point corresponds to the experimental configurations in Figure 7.1. Figure taken from reference [3].

In a polariton device under non-resonant excitation, the exciton density grows linearly with the excitation power up to the threshold value for polariton condensation at which it stops growing and remains constant [86]. In the vicinity of the condensation threshold, the emission energy of a polariton condensate is predominantly determined by the exciton density [137]. Therefore, the change of the dyad emission energy has to be directly linked to a variation of the exciton density as the excitation power has been kept constant throughout the experiment. By equation 5.1, the number of polaritons in a dyad is the sum of the number of polaritons without coupling, $2\mathcal{N}_0$, and the coupling

contribution, $J\cos\Delta\theta$. Thus, regardless of the sign and strength of J, either the in-phase or the anti-phase configuration determines a particle number higher than $2\mathcal{N}_0$. As such, the coupling mechanism causes an enhancement of the scattering rate from the reservoir to the condensates due to its bosonic stimulation nature which determines a decrease of the emission energy at small separation when the coupling is stronger.

7.4 Dyad spin coupling

Upon non-resonant excitation, polariton condensates spontaneously build-up a polarisation vector [9] which can be understood either by a polarisation pinning mechanism [192], or by an incomplete relaxation of the QW excitons during the energy relaxation process [193]. In the latter case, it is evident that a polarised reservoir favours the formation of a spinor condensates of the same polarisation. In particular, circularly polarised light leads to the formation of a polarised condensate co-circular with the excitation beam, while linear polarised light leads to the formation of polarised condensate where the polarisation axis is stochastically chosen at each realisation [194, 195]. The different behaviour for a linearly and circularly polarised excitation can be attributed polarisation dependent efficiency of the spin relaxation mechanism [196].

This section is dedicated to investigate the dyad coupling at a fixed distance as a function of the polarisation of one of the two condensate. Therefore, since we want to study between condensates with a known and bespoken spin state, it is favourable to use circularly polarised light for each graph node as the corresponding polariton condensate polarisation is directly related to the pump polarisation. In particular, one condensate is always kept left circularly polarised, while the polarisation of the second is smoothly tuned by means of a T-SLM between right to left circular following an equi-azimuthal trajectory on the Poincare sphere as discussed in figure 3.8.

Firstly, we measure the Stokes parameters, $S_{1,2,3}(x,y)$ as defined in equation 3.8, for a single condensate as a function of the excitation polarisation. Figures 7.5(a) and 7.5(b) show the spatially resolved circular Stokes component, $S_3(x,y)$, for right (a) and left (b) circular polarised excitation profile. At the condensate centre, the Stokes parameter reaches its maximum modulus of 0.80 corresponding to a 90% circular polarised light which has been inherited by the excitation source. Figure 7.5(c) shows that the averaged S_3 over a circular region of 2 μm around the condensate centre remains constant up to 1.5 times the threshold power for condensation. On the contrary, figure 7.5(d) shows that an average zero polarisation is observed at any excitation power when the excitation laser is horizontal or vertical polarised. It is worth mentioning that this results does not imply the existence of a non-polarised condensate but rather a vanishing mean spin due and ensemble average on 10^5 experimental realisations, as already observed in references[194, 195]. In addition, the amount of power that is coupled into the cavity

does not depends on the polarisation as we do not observe a significant change neither in the photoluminescence nor in the condensation wavevector.

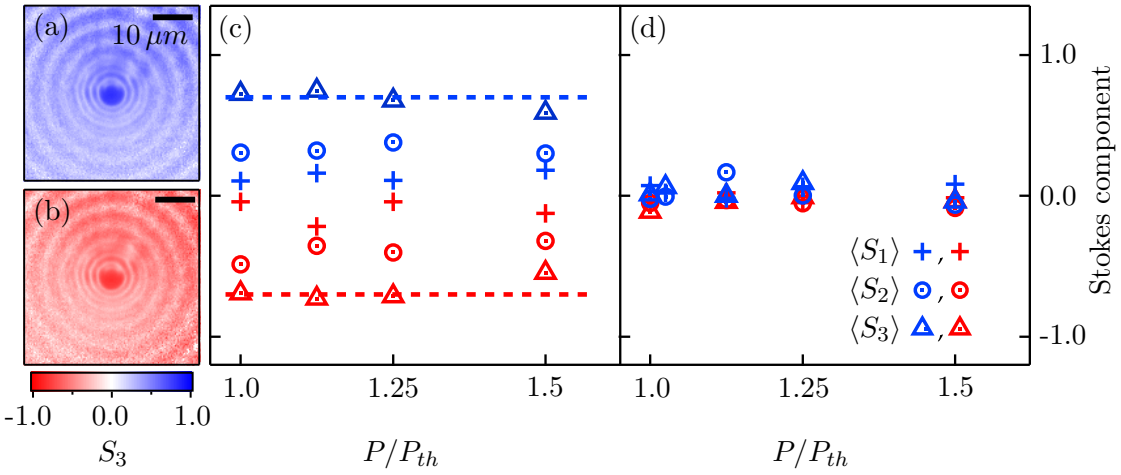

Figure 7.5: Measured real-space spatially resolved circular Stokes component of a single polariton condensate at condensation threshold non-resonantly pumped with a right (a) and left (b) circularly polarised pump. (c,d) Stokes parameters, $S_{1,2,3}$, of the condensation emission averaged within a circular region of radius $2\,\mu m$ around the condensate's centre as a function of power for right (red symbols) and left (blue symbols) pump polarisation. (d) Same as (c) but red (blue) symbols corresponds to horizontal (vertical) pump polarisation. The horizontal dashed lines in (c) correspond to $S_3 = \pm 0.7$.

Up to now, the excitation profiles has been homogeneously polarised and therefore, polariton wavefunction can be described as a scalar function neglecting its spinor nature, $\psi(\mathbf{r}, t)$. However, the most general polariton state is a linear combination of ± 1 spin states, $(\psi_+(\mathbf{r}, t), \psi_-(\mathbf{r}, t))$. Theoretically, equation 5.1 can be applied each component of the spinor wavefunction with an appropriate redefinition of the potential terms which takes into account the interaction of condensed polaritons with both co- and cross-polarised species. The ratio between the interaction strength of co- and cross-polarised particles is specified by a parameter α. In particular, α is expected to be negative which indicates a repelling force between co-polarised particles, otherwise attractive [197] and its modulus is expected to be lower than 1 due to spin anisotropy of the exciton-exciton interaction exchange interaction [196]. It is important to notice that α plays a crucial role in the dyad spin coupling because it couples the evolution of the two components of the spinor wavefunction.

We investigate the spin coupling in a polariton dyad with separation distance of $14\,\mu m$. Figures 7.6(a) to 7.6(d) show the real- and Fourier-space of a left co-circularly (a,b) and cross-circularly (c,d) polarised polariton dyad respectively. We observe a transition from ferromagnetic to anti-ferromagnetic coupling considering the fringes parity in real-space and the presence of a maximum or minimum at $k_{\parallel} = 0$ in Fourier-space. Nevertheless,

the outer ring in figure 7.6(d) still reveals a remaining contribution of the ferromagnetic configuration which can be attributed to the fact that each condensate is not 100% circularly polarised due to technical limitation and the spin relaxation mechanism. The dotted lines in Figures 7.6(a) and 7.6(b) are located on top of the fringes maxima as a guide for the eyes and are replicated in Figures 7.6(e) and 7.6(f). Figures 7.6(e) to 7.6(h) show the real- and Fourier-space circular Stokes parameter of a left co-circularly (e,f) and cross-circularly (g,h) polarised polariton dyad respectively. Figures 7.6(e) and 7.6(g) show similar features to Figures 7.6(e) and 7.6(g) but the visibility of the interference patterns is now higher than 0.5. The profile in figure 7.6(e) shows two maxima of $S_3 = 0.8$ located on top of condensates' position. On the contrary, the profile in figure 7.6(f) shows that the highest polarisation is displaced from the actual condensates' position by $1.5\,\mu m$ each into the structure centre. Moreover, the intensity maxima of the fringes in figure 7.6(b) coincide with zero lines of S_3. In addition, outside the dyad structure, S_3 has an opposite sign from the closest condensate. In other words, even though the closest condensates is left-circular polarised, there is a net flux of polariton of opposite polarisation outside the dyad. This effect, which may seems surprising at fist glance, could be possible attributed by to spin-dependent directional flow of polariton due to the polarisation inhomogeneity of the excitation profile. Indeed, figure 7.6(h) shows a strong polarisation dependent of motion in agreement with our interpretation.

7.5 Conclusions

In conclusion, we have developed a method to experimental measure the coupling strength across the nodes of a freely expanding polariton condensates graph. We have demonstrated how the phase coupling mechanism causes a shift in the polariton emission energy up to $250\,\mu eV$. We have proved that graph nodes can be coherently coupled up to macroscopic distances and that the coupling can be tuned within a wide range of both sign and strength offering the possibility to design polariton graphs whose corresponding optimisation task is considerable complex. Furthermore, we have also introduced how to control the coupling by exploiting the polariton spin which promises to further increase the complexity of the coupling network but it is yet to be explored whether and how a system of coupled polariton spinor condensates can effectively be mapped onto an analogue spin Hamiltonian. In this prospect, a more detailed interferometric study and a generalisation of our theoretical description is required to complete our understanding about the dyad spin coupling.

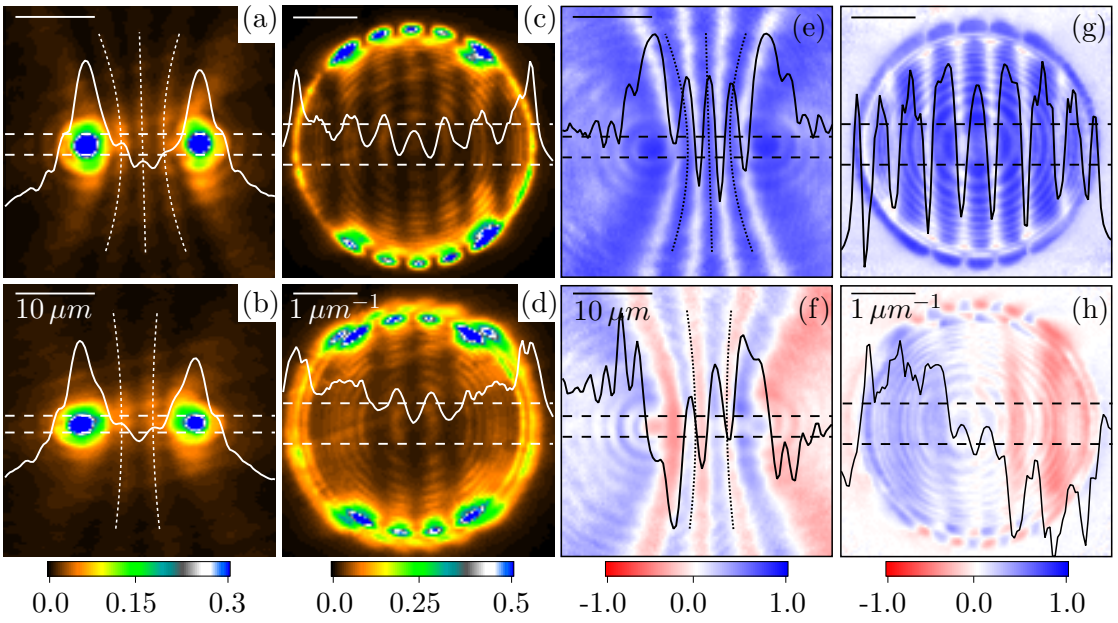

Figure 7.6: From left to right: real-space, Fourier-space, real-space circular Stokes component and Fourier-space circular Stokes component intensity map for a left co-polarised (top) and cross-polarised (bottom) dyad with separation distance of 14 μm. The solid lines are profiles integrated over the region delimited by the dashed lines. The dotted lines in the 1st and 3rd column lies on top of the fringes maxima of the figure of the real-space intensity profile. Images are saturated as indicated to enhance the fringes visibility. Figure taken from reference [5].

7.6 Contributions and Publications

The experiments reported in this chapter have been carried out by the the author and Julian D. Töpfer. The theoretical simulations of figure 7.1 have been performed by Kirill Kalinin and Prof. Natalia Berloff. Where cited, data reported in this chapter have been published previously in Ref. [3, 5].

Chapter 8

Conclusions and outlooks

The perfection of semiconductor growth techniques has made possible achievement of the strong coupling of light with matter in semiconductor microcavities. As such, photonic and excitonic eigenstates hybridise forming polaritons, an extremely light and strongly-interacting bosonic quasi-particle whose properties can be tuned by scanning the exciton-cavity detuning. After the first observation of light-matter strong coupling [7], much interest has raised in polariton systems due to their inherited non-linearity and non-parabolic dispersion which allow to trigger fascinating scattering processes [198]. Furthermore, polaritons have been shown to undergo a density-driven phase transition to a macroscopically occupied state with long-range phase coherence [9]. This phenomenon is associated to the formation of a polariton condensate which differs from classical BEC due to the strong inter-particle interaction and its non-equilibrium nature. The strong interaction of polaritons with the exciton reservoir provides a strong optical malleability of the potential landscape felt by polariton. In particular, in the case of tightly focused excitation profiles, the resulting anti-trapping potential causes a radial and ballistic outflow of polaritons away from the pumped area [86]. Therefore, imprinting multiple spatially separated condensates, a polariton graph, leads to a coherent exchange of particles. As a consequence of the noticeable interactions across neighbouring condensates, a polariton graph arranges its phase configuration to maximise the number of particles [14].

The work discussed in this thesis proposes and demonstrates polariton graph as a new system for simulating universal spin models. Moreover, as spin models can describe both physical spin system but also optimisation tasks, polariton graphs offer a promising platform to solve the quest of the optimum solution of a vast variety of optimisation problems. The main results are summarised in the following: in chapter 3, I discuss the optical techniques to both optically imprint a bespoken polariton graph and to read-out its phase configuration. In particular, the use of two combined SLMs is demonstrated to enable the imprinting of any polariton graph with single-node polarisation control. Then, different techniques are illustrated to optically read-out the polariton graph phase

configuration under steady-state excitation. In addition, tomographic techniques are discussed to measure the time/energy evolution of the polariton graph phase configuration under pulsed excitation. Ultimately, a full description of the sample is provided. In chapter 4, the first observation of polariton condensation is reported in a strain compensated structure with InGaAs quantum wells. The resulting low density of defects is an essential ingredient to prove that scalability for a polariton-based simulator as it sets an upper-limit to the largest polariton graph coherently coupled. In addition, the material choice enables to work in transmission-like geometry simplifying the engineering of a graph with a complex network of coupling. In chapter 5, I presented both the theoretical frameworks and the experimental realisations of mapping a polariton graph to the classical XY Hamiltonian under both steady-state and pulsed excitation. The platform has been tested with graphs of different geometry and dimensionality. In chapter 6, polariton graphs are also presented as an alternative route to create stable, spontaneous and irrotational quantised vortices of arbitrary multiplicity. However, the experimental features presented here are not conclusive yet. In chapter 7, a detailed study of the coupling mechanism is presented proving coherent coupling over macroscopic distances and a large tunability range of the coupling. In addition, a method to quantify and measure the coupling across a condensate pair is proposed and demonstrated. Eventually, interaction between cross-polarised polariton dyad is presented where it is shown that two phase configurations are accessible by tuning the polarisation of each pump beam. However, a direct measurement of the spinor condensate's phase distribution is more complex and yet to be performed.

The presented work introduces polaritons as a new promising platform to simulations which offers application-oriented advantages over similar systems based on ultra-cold atomic gases in optical lattice [151] or network of coupled lasers [152]. Polariton condensates can be optically imprinted in any 2D graph with arbitrary polarisation distribution by using SLMs and a single focused beam. The coupling network can be tuned within a wide range of both signs and strengths both by tailoring the graph geometry, overall excitation density and by engineering each node's profile and polarisation. Optical read-out relies on standard optical techniques and it is continuous provided by photons leaking out of the cavity due to the polaritons finite lifetime enabling in-situ characterisation of polariton graphs. In addition, contrary to coupled laser network, polariton devices may operate in single-mode regime avoiding mode competition as they are based on microcavities. As such, they can stable operate near condensation threshold enabling the bottom-up approach to search for the ground states with no requirement for annealing. Furthermore, the state of the art polariton devices already operate at temperatures much higher than atomic BEC ones and, in addition, the ongoing development of new materials is heading towards the establishment of room temperature polariton condensates [10] and even the potentiality for electrical injection [11].

In conclusions, polariton graphs is an appealing platform for performing simulations

due to its optical read-out, rapid scalability and single site control. Nevertheless, more work needs to be done to understand its intrinsic limitation and to push the system to its limits, i.e. graph size upper-limit, upper-limit of the coupling network complexity and accuracy of finding the ground state. In an hypothetical road map, I would prioritise further understanding of the coupling across cross-polarised condensates concerning both theory and experiments. The next step can be to imprint a complex network of couplings and to validate the experimental solution with the results inefficiently calculated with a computer. Afterwards, future works include expanding the graph measuring the coherence between nodes as a function of their physical distances to established a graph size upper-limit and to determine if it depends on the graph geometry and on the complexity of the coupling network. Furthermore, there is still a lack of understanding about how the the energy gap of the XY Hamiltonian scales with the coupling network complexity. Eventually, the accuracy of the platform should be tested considering problems of interest, i.e. the travelling salesman or its simplified version of the knight problem [199].

Appendix A

Transfer matrix code

Matlab transfer matrix code used to calculate the reflectivity spectrum of Figures 2.1, 2.2 and 2.4.

```
c0=299792458;

lambda0=858;

nSub=3.5;
nL=1.9;
nH=2.3;
nCin=3.5;

nQW=3.6;
dQW=10;
G0=2*10^13;
w0=2*pi*c0/lambda0*10^9;
g=7*10^10;

dL=lambda0/nL/4;
dH=lambda0/nH/4;
dCin=lambda0/nCin/2;
N=20;
lambda=760:0.01:960;

structure=2;

for mm=1:length(lambda)
    L(mm)=exp(1i*(2*pi)/(lambda(mm))*nL*dL);
```

```
    H(mm)=exp(1i*(2*pi)/(lambda(mm))*nH*dH);
    Cin(mm)=exp(1i*(2*pi)/(lambda(mm))*nCin*dCin);

    r_QW(mm)=1i*G0/(w0-2*pi*c0/lambda(mm)*10^9-1i*(G0+g));
    t_QW(mm)=1+r_QW(mm);

    RR_QW(mm)=abs(r_QW(mm))^2;

    IinDBRtop=[1 1;-nL nL]^(-1)*[1 1;-1 1];
    DBRtop=[L(mm) 0;0 conj(L(mm))]*[1 1;-nH nH]^(-1)*[1 1;-nL nL]*
           *[H(mm) 0;0 conj(H(mm))]*[1 1;-nL nL]^(-1)*[1 1;-nH nH];

    IinCav=([1 1;-nL nL]^(-1)*[1 1;-nH nH])^(-1)*([1 1;-nCin nCin]^(-1)*
           *[1 1;-nH nH]);
    Cav=[Cin(mm) 0;0 conj(Cin(mm))];

    QW=1/t_QW(mm)*[t_QW(mm)^2-r_QW(mm)^2 r_QW(mm);-r_QW(mm) 1];
    CavQW=Cav*QW*Cav;
    IoutCav=([1 1;-nH nH]^(-1)*[1 1;-nCin nCin]);

    DBRbottom=[H(mm) 0;0 conj(H(mm))]*[1 1;-nL nL]^(-1)*[1 1;-nH nH]*
              *[L(mm) 0;0 conj(L(mm))]*[1 1;-nH nH]^(-1)*[1 1;-nL nL];
    IoutDBRbottom=([1 1;-nH nH]^(-1)*[1 1;-nL nL])^(-1)*[1 1;-1 1]^(-1)*
           *[1 1;-nL nL];
    if structure==0
        matrix=IinDBRtop*DBRtop^N*IoutDBRbottom;
    elseif structure==1
        matrix=IinDBRtop*DBRtop^N*IinCav*Cav*IoutCav*DBRbottom^N*
           *IoutDBRbottom;
    elseif structure==2
        matrix=IinDBRtop*DBRtop^N*IinCav*CavQW*IoutCav*DBRbottom^N*
           *IoutDBRbottom;
    end

    R(mm)=abs(matrix(2,1))^2/abs(matrix(1,1))^2;
    T(mm)=abs((matrix(1,1))^(-1))^2;
end
plot(lambda,R,'LineWidth',2)
```

Appendix B

Phase retrieval code

Igor Pro code used to calculate the phase pattern for the R-SLM.

```
#pragma rtGlobals=3
#include <functionprofiling>

//<==><==><==><==><==><==><==><==><==><==><==><==><==><==><==><==><==><==><==><==><==>
// Author Matteo Silva
// Date 2015, 11th of May
//<==><==><==><==><==><==><==><==><==><==><==><==><==><==><==><==><==><==><==><==><==>

Menu "Matteo"
 SubMenu "SLM"
  "Test Pattern/6",TestPattern()
  "Test Pattern - HS/S6",HS_TestPattern()
  "Hologram - Alg./5",SpatialLightModulator(0)
  "Set of Holograms - Alg./S5",SpatialLightModulator(1)
  "Hologram - ES/7",ExactSolution(0)
  "Set of images - ES/S7",ExactSolution(1)
  "Holoeye Lattice/9",SetHSL(0)
  "Set of Holoeye Lattice/S9",SetHSL(1)
 end
end

//<==><==><==><==><==><==><==><==><==><==><==><==><==><==><==><==><==><==><==><==><==>
function Optimization()
 BeginFunctionProfiling()
 ExactSolution(0)
 ExactSolution(1)
```

```
 SpatialLightModulator(0)
 SpatialLightModulator(1)
 EndFunctionProfiling()
end

//<==><==><==><==><==><==><==><==><==><==><==><==><==><==><==><==><==><==>

Function TestPattern()
 SetDataFolder root:Holography
 Wave Source,Hologram,IntOut
 Wave/C Ein,Eout
 Ein=sqrt(Source)*Exp(Cmplx(0,Hologram))
 FFT/Dest=Eout Ein
 IntOut=MagSqr(Eout)
 DoWIndow Test
 DoWIndow/F Test
 SetDataFolder root:
End

//<==><==><==><==><==><==><==><==><==><==><==><==><==><==><==><==><==><==>

Function HS_TestPattern()
 ImageLoad/T=rpng/Q/N=Hologram/G
 Wave Hologram
 make/N=(1920,1920)/O Source,IO,Holo
 make/N=(1920,1920)/O/C Ein,Eout
 SetScale/I x,-960,960,Source,Ein
 SetScale/I y,-960,960,Source,Ein
 Source=Gauss(x,0,050,y,0,050)
 Holo=(q>419 && q<1500)? Hologram[p][q-420]:128
 Holo-=128
 Holo/=128
 Ein=Sqrt(Source)*Exp(Cmplx(0,pi*Holo))
 FFT/Dest=Eout Ein
 IO=MagSqr(Eout)
End

//<==><==><==><==><==><==><==><==><==><==><==><==><==><==><==><==><==><==>

Function SetHSL(NI)
 Variable NI
```

```
 NewDataFolder/O/S root:Holoeye
 NewPath/O/Q/C SaveHere,"Macintosh HD:Users:ms1d14:Desktop:SLMimages"
 Make/N=(400,400)/O Tg
 Variable/G CP
 String/G Name="",ltt="Sq" //sSq,Rtx,Kgm,Exa,2D,Sq,Tr
 Variable ii,Set=NumberOfImages(NI)
 for(ii=0;ii<Set;ii+=1)
  Tg=0
  Name=""
  CP=ii
  HoloeyeSoftwareLattice(ltt)
  ImageSave/D=40/T="JPEG"/P=SaveHere/Q=1.00 Tg as Name
 endfor
 SetDataFolder root:
End

//<==><==><==><==><==><==><==><==><==><==><==><==><==><==><==><==><==><==><==><==>

Function HoloeyeSoftwareLattice(ltt)
 String ltt
 Wave Tg
 Variable GvsD=1
 Variable sz=1*1
 Variable w=0.06*10
 Variable d=40
 Variable r=50
 Variable a=DefLatBasis(ltt)
 Wave Basis
 NVar CP
 NVar/C v1,v2
 SVar Name
 d=2+CP
 r=4*d
//Lattice definition
 Variable ii,jj,kk,pp,qq
 for(ii=-100;ii<=100;ii+=1)
  for(jj=-100;jj<=100;jj+=1)
   for(kk=0;kk<a;kk+=1)
    pp=Real(ii*v1+jj*v2+Basis[kk])*d+200
    qq=Imag(ii*v1+jj*v2+Basis[kk])*d+200
    if((pp+w*sign(ii)-200)^2+(qq+w*sign(jj)-200)^2<r^2)
```

```
     if(GvsD==0)
      Tg+=Gauss(x,pp,w,y,qq,w)
     elseif(GvsD==1)
      Tg+=(abs(pp-p)<sz && abs(qq-q)<sz)? 1:0
     endif
    endif
   endfor
  endfor
 endfor
 DoUpdate
 if(GvsD==0)
  Name="HS_Glat_"+ltt+"_d"+num2str(d)+"pxl"
 elseif(GvsD==1)
  Name="HS_Dlat_"+ltt+"_d"+num2str(d)+"pxl"
 endif
End

//<==><==><==><==><==><==><==><==><==><==><==><==><==><==><==><==><==><==>

Function ExactSolution(NI)
 Variable NI
 NewDataFolder/O/S root:Holography
 Variable jj,ii,Set=NumberOfImages(NI)
 NVar CP
 Initio()
 VariablesChoice()
 Spring()
 for(ii=0;ii<Set;ii+=1)
  CP=ii
  HoloDef()
  Wave Hologram,Holo,Source,IntOut,Grating,Lens
  for(jj=0;jj<2;jj+=3)
   CropPhase(Hologram,Holo,jj)
   Saving(Holo,jj)
  endfor
 endfor
 SetDataFolder root:
End

//-----------------------------------
```

```
Function HoloDef()
 Wave Hologram,Grating,Lens
 Wave/C Ein
 Duplicate/O/C Ein,auxC
 auxC=0
 SVar Name
 Variable ii,jj,kk
 Variable pp,qq,phi,phi0=pi/2
 Variable k=3
 Variable num
 NVar CP
//     POLYGONS
//     num=8
//     sprintf Name,"ES_poly_%02.f_k=%06.3f",num,k
//     for(ii=0;ii<num;ii+=1)
//      phi=phi0+2*pi/num*ii
//      auxC+=exp(cmplx(0,k*(x*cos(phi)+y*sin(phi))))
//     endfor
//     auxC*=exp(cmplx(0,p*Grating[0]+q*Grating[1]))

// LATTICES
 num=3
 String ltt="Kgm"
 Variable a=DefLatBasis(ltt)
 Wave Basis
 NVar/C v1,v2
 k=2
 sprintf Name,"ES_"+ltt+"_%02.f_k=%06.3f",num,k
 for(ii=-100;ii<=100;ii+=1)
  for(jj=-100;jj<=100;jj+=1)
   for(kk=0;kk<a;kk+=1)
    pp=Real(ii*v1+jj*v2+Basis[kk])*k
    qq=Imag(ii*v1+jj*v2+Basis[kk])*k
    if(pp^2+qq^2<(num*k)^2)
     auxC+=exp(cmplx(0,pp*x+y*qq))
    endif
   endfor
  endfor
 endfor
 Hologram=atan2(imag(auxC),real(auxC))
 KillWaves auxC
```

```
End

//<==><==><==><==><==><==><==><==><==><==><==><==><==><==><==><==><==>

function SpatialLightModulator(NI)
 Variable NI
 Variable jj,ii,Set=NumberOfImages(NI)
 Initio()
 VariablesChoice()
 NVar s,t1,a1,a2,Sym,CP
 wave Hologram,Holo
 Wave/C Ein
 SVar Name
 Spring()
 autumn()
 for(ii=0;ii<Set;ii+=1)
  CP=ii
  Name=""
  Autumn()
  Precession()
  DiagonalShift()
  for(jj=0;jj<2;jj+=1)
   CropPhase(Hologram,Holo,jj)
   Saving(Holo,jj)
  endfor
 endfor
 SetDataFolder root:
 TestPattern()
end

//<==><==><==><==><==><==><==><==><==><==><==><==><==><==><==><==><==>

function Initio()
 NewDataFolder/O/S root:Holography
 Variable/G wl=0.8//um
 Variable/G f=500//mm
 Variable/G pxl=8//um/pxl
 variable/G NIt=30,ItCount=0
 Variable/G m=0.4,e=1,r=25
 Variable/G CP=0
 String/G Name=""
```

```
 String/G SavingFolder="Macintosh HD:Users:ms1d14:Desktop:SLMimages"
 String/G SubFolder=""
 Make/O/N=2 SLM=0,SLM2=0
 SLM[0]=1920; SLM[1]=1080; SLM2=WaveMax(SLM)
 SLM2=2048; SLM2*=2
 make/O/N=(SLM2[0],SLM2[1]) Source,Target,Hologram,IntOut,auxW
 make/O/N=(SLM2[0],SLM2[1])/C Ein,Eout,EoutNew,EinNew
 make/O/N=(SLM[0],SLM[1]) Holo
 Source=0
 Target=0
 Hologram=0
 IntOut=0
 Variable/G Dk=pxl/(wl*f)
 Variable/G Dx=1/(Dk*SLM2[0])
 SetScale/P x,-SLM2[0]*Dk/2,Dk,Source,Ein,EinNew,Hologram
 SetScale/P y,-SLM2[1]*Dk/2,Dk,Source,Ein,EinNew,Hologram
 SetScale/P x,-SLM2[0]*Dx/2,Dx,Target,IntOut,auxW,Eout,EoutNew
 SetScale/P y,-SLM2[1]*Dx/2,Dx,Target,IntOut,auxW,Eout,EoutNew
 make/O/N=10 SPar=0
 make/O/N=69 TPar=0
 make/N=2/O Lens,Grating
 Lens[0]=0.5
 Lens[1]=0.2
 Grating[0]=0.408
 Grating[1]=Grating[0]
end

//<==><==><==><==><==><==><==><==><==><==><==><==><==><==><==><==><==><==><==>

Function NumberOfImages(NI)
 Variable NI
 variable Set=1
 if(NI==1)
  Prompt Set,"Number of image for the set"
  DoPrompt "Holo Set Extention",Set
  if(V_Flag==1)
   abort
  endif
 endif
 return Set
End
```

```
//<==><==><==><==><==><==><==><==><==><==><==><==><==><==><==><==><==><==><==>

Function VariablesChoice()
 variable/G s=0
 variable/G t1=3
 variable/G a1=0
 Variable/G a2=1
 variable/G sym=0
End

//<==><==><==><==><==><==><==><==><==><==><==><==><==><==><==><==><==><==><==>

function Spring()
 NVar s
 wave Source,SPar,SLM2
 Source=0
 SPar[0]=0
 SPar[1]=0
 SPar[2]=5
 SPar[3]=5
  if(s==1)
   variable xW=SPar[2],yW=Spar[3]
   Prompt xW,"Enter the x width"
   Prompt yW,"Enter the y width"
   DoPrompt "Source dialog",xW,yW
   SPar[0]=xW; SPar[1]=yW
  endif
//     Standard input
//     Source=Gauss(x,SPar[0],SPar[2],y,SPar[1],SPar[3])
//     Rega Fit
 Variable w_x,w_y,cor
 w_x=217.92
 w_y=281.1
 cor=-0.26836
 w_x*=25/15*0.015//mm //I used a telescope made of 25cm and 15 cm to demagnified
 w_y*=25/15*0.015//mm // on the QCam whose pize size is about 14-16um
 Source=Exp(-1/(1-cor^2)*(((x-SPar[0])/w_x)^2+((y-SPar[1])/w_y)^2-2*cor*(x-SPar[0])*(y-SPar
 WaveStats/Q Source
 SPar[4]=V_sum
end
```

```
//<==><==><==><==><==><==><==><==><==><==><==><==><==><==><==><==><==><==><==><==>

function Autumn()
 NVar t1
 wave SPar,target,TPar,SLM,SLM2
 TPar=0
 Target=0
 TPar[0]=0
 TPar[1]=0
 SVar Name,SubFolder
 if(t1==0)
  Name="Vortex"
 elseif(t1==1)
  Name="V_AV"
 elseif(t1==2 || t1==3)
  Name="Lat"
 elseif(t1==7)
  Name="Dyad"
 elseif(t1==8)
  Name="Polygon"
 endif
 SubFolder=":"+Name
 Execute/Q Name+"()"
 WaveStats/Q Target
 variable A=V_sum; Target*=(SPar[4]/A)
end

//----------------------------------------

function Vortex()
 wave TPar,Target,SPar
 TPar[2]=0.061
 TPar[3]=TPar[2]
 TPar[4]=0.5
//     NVar CP
//     TPar[4]=CP
 Svar Name
 Name+="_d="+num2str(TPar[4])
 if(abs(mod(TPar[4],1))<=0.01)
  Name+=".00"
```

```
 elseif(abs(mod(TPar[4]*10,1))<=0.01)
  Name+="0"
 endif
 TPar[5]=TPar[0]-Tpar[4]/sqrt(12)
 TPar[6]=TPar[1]-Tpar[4]/2
  TPar[7]=TPar[0]-Tpar[4]/sqrt(12)
  TPar[8]=TPar[1]+Tpar[4]/2
 TPar[9]=TPar[0]+Tpar[4]/sqrt(3)
 TPar[10]=TPar[1]
 variable ii=5
 Do
  Target+=Gauss(x,TPar[ii],TPar[2]/sqrt(2),y,TPar[ii+1],TPar[3]/sqrt(2))
  ii+=2
 while(TPar[ii]!=0)
end

//---------------------------------------

function V_AV()
 wave TPar,Target
 TPar[2]=0.061; TPar[3]=TPar[2]; TPar[4]=12.5
 NVar CP
 Svar Name
 Name+="_d="+num2str(TPar[4])
 if(abs(mod(TPar[4],1))<=0.01)
  Name+=".00"
 elseif(abs(mod(TPar[4]*10,1))<=0.01)
  Name+="0"
 endif
 TPar[5]=TPar[0]-Tpar[4]/4*sqrt(3)
 TPar[6]=TPar[1]-Tpar[4]/4
  TPar[7]=TPar[0]+Tpar[4]/4*sqrt(3)
  TPar[8]=TPar[1]+Tpar[4]/4
 TPar[9]=TPar[5]
 TPar[10]=TPar[6]+Tpar[4]
  TPar[9]=TPar[5]
  TPar[10]=-sqrt(3)*(TPar[9]-1920)+1920
 variable ii=5
 Do
  Target+=Gauss(x,TPar[ii],TPar[2]/sqrt(2),y,TPar[ii+1],TPar[3]/sqrt(2))
  ii+=2
```

```
 while( Tpar[ii]!=0)
end

//---------------------------------------

Function Dyad()
 wave TPar,Target
 TPar[2]=0.061
 TPar[3]=TPar[2]
 TPar[4]=20
 TPar[5]=1
//     Set of image
 NVar CP,Dx
 TPar[4]=(160+trunc(CP/10)*2.5)*Dx
 TPar[5]=1+mod(CP,10)/50
 Svar Name
 String auxName
 Sprintf auxName,"%.3f",TPar[4]
 Name+="_d"+auxName
 Sprintf auxName,"%.2f",TPar[5]
 Name+="IR"+auxName
 Variable HV=1
 TPar[6]=TPar[0]+Tpar[4]/2*(1-HV)
 TPar[7]=TPar[1]+Tpar[4]/2*HV
  TPar[8]=TPar[0]-Tpar[4]/2*(1-HV)
  TPar[9]=TPar[1]-Tpar[4]/2*HV
 Target=Gauss(x,TPar[6],TPar[2]/sqrt(2),y,TPar[7],TPar[3]/sqrt(2))+
   +TPar[5]*Gauss(x,TPar[8],TPar[2]/sqrt(2),y,TPar[9],TPar[3]/sqrt(2))
End

//---------------------------------------

Function Polygon()
 wave TPar,Target
 TPar[2]=0.015
 TPar[3]=TPar[2]
 TPar[4]=12.5
 TPar[5]=4
//     Set of image-------------------
 NVar CP
 TPar[4]=0.12+0.005*trunc(CP/2)
```

```
 TPar[5]=6+2*mod(CP,2)
//-----------------------------------
 TPar[6]=2*pi/TPar[5]
 TPar[7]=2*TPar[4]*sin(TPar[6]/2)
 TPar[8]=0
 TPar[9]=2*pi/180*0
 SVar Name
 String auxName
 Sprintf auxName,"%.3f",TPar[4]
 Name+="_"+num2str(TPar[5])+"-"+num2str(TPar[8])+"d="+auxName
 variable ii,Xc,Yc
 for(ii=0;ii<TPar[5]+TPar[8];ii+=1)
  if(ii<TPar[5])
   Xc=TPar[0]+TPar[4]*cos(TPar[6]*ii+TPar[9])
   Yc=TPar[1]+TPar[4]*sin(TPar[6]*ii+TPar[9])
  elseif(ii==TPar[5]) //only if TPar[8]=1=>spot in the middle
   Xc=TPar[0]
   Yc=TPar[1]
  endif
  Redimension/N=(TPar[5]+TPar[8]) AR
  Target+=AR[ii]*Gauss(x,Xc,TPar[2]/sqrt(2),y,Yc,TPar[3]/sqrt(2))
 endfor
End

//<==><==><==><==><==><==><==><==><==><==><==><==><==><==><==><==><==><==><==>

Function Lat()
 wave TPar,Target
 SVar Name
 NVar t1,CP
 t1=2+trunc(CP/25)
 TPar[2]=0.06*1
 TPar[3]=TPar[2]
 TPar[4]=0.404*3
 TPar[5]=2//radius of the image
 String auxName="",ltt="Kgm"
 switch(t1)
  case 2:
   Name+="_G_"+ltt
   break
  case 3:
```

```
   Name+="_D_"+ltt
   break
  default:
   abort
 endswitch
 Sprintf auxName,"%.4f",TPar[4]; Name+="_d"+auxName
 Sprintf auxName,"%02.1f",TPar[5]; Name+="_r"+auxName
 Variable a=DefLatBasis(ltt)
  Wave Basis
  NVar/C v1,v2
  Variable ii,jj,kk,x0,y0
  for(ii=-100;ii<=100;ii+=1)
   for(jj=-100;jj<=100;jj+=1)
    for(kk=0;kk<a;kk+=1)
     x0=Real(ii*v1+jj*v2+Basis[kk])*TPar[4]+TPar[0]
     y0=Imag(ii*v1+jj*v2+Basis[kk])*TPar[4]+TPar[1]
    if((x0+TPar[2]-TPar[0])^2+(y0+TPar[3]-TPar[1])^2<TPar[5]^2)
     if(t1==2)
      Target+=Gauss(x,x0,TPar[2]/sqrt(2),y,y0,TPar[3]/sqrt(2))
     elseif(t1==3)
      Variable pp,qq,sz=10
      pp=(x0-DimOffSet(Target,0))/DimDelta(Target,0)
      pp=(pp-trunc(pp)<0.5)? trunc(pp):trunc(pp)+1
      qq=(y0-DimOffSet(Target,1))/DimDelta(Target,1)
      qq=(qq-trunc(qq)<0.5)? trunc(qq):trunc(qq)+1
      Target+=(abs(pp-p)<sz && abs(qq-q)<sz)? 1:0
     endif
    endif
   endfor
  endfor
 endfor
End

//---------------------------------------

function DefLatBasis(input)
 String input
 Variable a
 Variable/C/G v1,v2
 make/N=(10)/O/C Basis=0
 if(cmpstr(input,"Tr")==0)
```

```
 a=1
 v1=cmplx(1,0)
 v2=cmplx(1/2,sqrt(3)/2)
elseif(cmpstr(input,"Sq")==0)
 a=1
 v1=cmplx(1,0)
 v2=cmplx(0,1)
 Basis[0]=0
elseif(cmpstr(input,"2D")==0)
 Variable phi=pi/4
 Variable l=1
 a=1
 v1=cmplx(1,0)
 v2=l*cmplx(cos(phi),sin(phi))
 Basis[0]=0
elseif(cmpstr(input,"Exa")==0)
 a=2
 v1=cmplx(1,0)
 v2=cmplx(1/2,sqrt(3)/2)
 Basis[0]=0
 Basis[1]=cmplx(0,0.5)
elseif(cmpstr(input,"Kgm")==0)
 a=3
 v1=cmplx(1,0)
 v2=cmplx(1/2,sqrt(3)/2)
 Basis[0]=0
 Basis[1]=0.5*cmplx(1,0)
 Basis[2]=0.5*cmplx(1/2,sqrt(3)/2)
elseif(cmpstr(input,"Rtx")==0) //Rhombitrihexagonal
 a=6
 v1=cmplx(0,1)
 v2=cmplx(sqrt(3)/2,1/2)
 Basis[0]=sqrt(3)/2/(1+sqrt(3))*cmplx(1,1/sqrt(3))
 Basis[1]=Basis[0]+cmplx(0,1)/(1+sqrt(3))
 Basis[2]=Basis[0]+cmplx(sqrt(3)/2,1/2)/(1+sqrt(3))
 Basis[3]=Basis[1]+Cmplx(1/2,sqrt(3)/2)/(1+sqrt(3))
 Basis[4]=Basis[2]+Cmplx(1/2,sqrt(3)/2)/(1+sqrt(3))
 Basis[5]=Basis[4]+cmplx(0,1)/(1+sqrt(3))
elseif(cmpstr(input,"sSq")==0)
 a=4
 v1=cmplx(cos(pi/12),sin(pi/12))
```

```
  v2=cmplx(-sin(pi/12),cos(pi/12))
  Basis[0]=cmplx(cos(pi/12),sin(pi/12))
  Basis[1]=Basis[0]+cmplx(cos(pi/12),-sin(pi/12))
  Basis[2]=Basis[0]+cmplx(-sin(pi/12),-cos(pi/12))
  Basis[3]=Basis[2]+cmplx(cos(pi/12),-sin(pi/12))
 else
  DoAlert 0,"Wrong lattice definition"
  Abort
 endif
 Redimension/N=(a) Basis
 return a
end

//<==><==><==><==><==><==><==><==><==><==><==><==><==><==><==><==><==><==><==><==>

function Precession()
 NVar a1,a2,sym
 wave hologram,SLM2,Source,IntOut,Target,SPar,TPar,Grating,Lens,auxW
 Wave/C Ein,Eout,EoutNew,EinNew
 NVar NIt,ItCount
 SVar Name
 hologram=mod((x^2*Lens[0]/2+y^2*(1-Lens[0])/2)/Lens[1],2*pi)
 Ein=sqrt(Source)*exp(cmplx(0,hologram))
 for(ItCount=0;ItCount<NIt;ItCount+=1)
  FFT/Dest=Eout Ein
  IntOut=magsqr(Eout)
  variable IInt
  if(a2==0)
   EoutNew=sqrt(target)*exp(cmplx(0,atan2(Imag(Eout),Real(Eout))))
   WaveStats/Q IntOut
   IInt=V_sum
   Eout/=sqrt(IInt/SPar[4])
  elseif(a2==1)
   auxW=(((x-TPar[0])/r)^2+((y-TPar[1])/(e*r))^2<1)? (m*IntOut):((1-m)*IntOut)
   WaveStats/Q auxW
   IInt=V_sum
   IntOut/=IInt/SPar[4]
   EoutNew=(((x-TPar[0])/r)^2+((y-TPar[1])/(e*r))^2<1)? (m*sqrt(target)):(1-m)*sqrt(I
   EoutNew*=exp(cmplx(0,atan2(imag(Eout),real(Eout))))
  endif
  IFFT/C/Dest=EinNew EoutNew
```

```
  Ein=sqrt(Source)*exp(cmplx(0,atan2(Imag(EinNew),Real(EinNew))))
 endfor
 Name+=num2str(m)
end

//<==><==><==><==><==><==><==><==><==><==><==><==><==><==><==><==><==>

Function DiagonalShift()
 Wave/C Ein,Eout
 Wave Grating,IntOut,Hologram,SPar
 hologram=atan2(Imag(Ein),Real(Ein))/pi
end

//<==><==><==><==><==><==><==><==><==><==><==><==><==><==><==><==><==>

function CropPhase(old,new,T)
 wave old,new
 Variable T
 wave SLM2,SLM
 if(T==1)
  MatrixTranspose old
 endif
 Variable Xos,yOS
 Xos=SLM2[0]/2-SLM[0]/2
 Yos=SLM2[1]/2-SLM[1]/2
 new[][]=old[p+Xos][q+Yos]
end

//<==><==><==><==><==><==><==><==><==><==><==><==><==><==><==><==><==>

function Saving(wave2d,T)
 wave wave2d
 Variable T
 wave TPar
 NVar CP
 SVar SavingFolder,Name,SubFolder
 String aux1,auxName=Name,SvFldr
 Variable ii
 if(T==1)
  SvFldr=SavingFolder+SubFolder+"_T"
 else
```

```
  SvFldr=SavingFolder+SubFolder+"_N"
 endif
 NewPath/O/Q/C SaveHere,SvFldr
 ImageSave/O/D=40/T="PNG"/P=SaveHere Wave2d as Name+".png"
 Name=auxName
end
```

References

[1] Pasquale Cilibrizzi, Alexis Askitopoulos, Matteo Silva, Faebian Bastiman, Edmund Clarke, Joanna M. Zajac, Wolfgang Langbein, and Pavlos G. Lagoudakis. Polariton condensation in a strain-compensated planar microcavity with InGaAs quantum wells. *Applied Physics Letters*, 105(19):191118, November 2014.

[2] Natalia G. Berloff, Matteo Silva, Kirill Kalinin, Alexis Askitopoulos, Julian D. Toepfer, Pasquale Cilibrizzi, Wolfgang Langbein, and Pavlos G. Lagoudakis. Realizing the XY Hamiltonian in polariton simulators. *Nature Materials - accepted*, 2017.

[3] Matteo Silva, Kirill Kalinin, Pasquale Cilibrizzi, Alexis Askitopoulos, Wolfgang Langbein, Natalia G. Berloff, and Pavlos G. Lagoudakis. Heisenberg exchange coupling in polariton dyads. *under review at Physical Review B*, 2017.

[4] Kirill Kalinin, Matteo Silva, J.D. Toepfer, Wolfgang Langbein, Natalia G. Berloff, and Pavlos G. Lagoudakis. Giant vortices of controlled multiplicity in polariton lattices. *under review at Nature Communication*, 2017.

[5] J.D. Toepfer, Matteo Silva, Kirill Kalinin, Wolfgang Langbein, Natalia G. Berloff, and Pavlos G. Lagoudakis. Spin coupling in a polariton dyad. *in preparation*, 2017.

[6] K. Iga. Surface-emitting laser-its birth and generation of new optoelectronics field. *IEEE Journal of Selected Topics in Quantum Electronics*, 6(6):1201–1215, November 2000.

[7] C. Weisbuch, M. Nishioka, A. Ishikawa, and Y. Arakawa. Observation of the coupled exciton-photon mode splitting in a semiconductor quantum microcavity. *Physical Review Letters*, 69(23):3314–3317, December 1992.

[8] A. V. Kavokin, J.J. Baumberg, G. Malpuech, and F.P. Laussy. *Microcavities*. Oxford University Press, Oxford, 2007.

[9] J. Kasprzak, M. Richard, S. Kundermann, A. Baas, P. Jeambrun, J. M. J. Keeling, F. M. Marchetti, M. H. Szymańska, R. André, J. L. Staehli, V. Savona, P. B. Littlewood, B. Deveaud, and Le Si Dang. Bose–Einstein condensation of exciton polaritons. *Nature*, 443(7110):409–414, September 2006.

[10] S. Christopoulos, G. Baldassarri Höger von Högersthal, A. J. D. Grundy, P. G. Lagoudakis, A. V. Kavokin, J. J. Baumberg, G. Christmann, R. Butté, E. Feltin, J.-F. Carlin, and N. Grandjean. Room-Temperature Polariton Lasing in Semiconductor Microcavities. *Physical Review Letters*, 98(12):126405, March 2007.

[11] Christian Schneider, Arash Rahimi-Iman, Na Young Kim, Julian Fischer, Ivan G. Savenko, Matthias Amthor, Matthias Lermer, Adriana Wolf, Lukas Worschech, Vladimir D. Kulakovskii, Ivan A. Shelykh, Martin Kamp, Stephan Reitzenstein, Alfred Forchel, Yoshihisa Yamamoto, and Sven Höfling. An electrically pumped polariton laser. *Nature*, 497(7449):348–352, May 2013.

[12] K. G. Lagoudakis, B. Pietka, M. Wouters, R. André, and B. Deveaud-Plédran. Coherent Oscillations in an Exciton-Polariton Josephson Junction. *Physical Review Letters*, 105(12):120403, September 2010.

[13] Alberto Amo, Jérôme Lefrère, Simon Pigeon, Claire Adrados, Cristiano Ciuti, Iacopo Carusotto, Romuald Houdré, Elisabeth Giacobino, and Alberto Bramati. Superfluidity of polaritons in semiconductor microcavities. *Nature Physics*, 5(11):805–810, November 2009.

[14] H. Ohadi, R. L. Gregory, T. Freegarde, Y. G. Rubo, A. V. Kavokin, N. G. Berloff, and P. G. Lagoudakis. Nontrivial Phase Coupling in Polariton Multiplets. *Physical Review X*, 6(3):031032, August 2016.

[15] P. Cristofolini, A. Dreismann, G. Christmann, G. Franchetti, N. G. Berloff, P. Tsotsis, Z. Hatzopoulos, P. G. Savvidis, and J. J. Baumberg. Optical Superfluid Phase Transitions and Trapping of Polariton Condensates. *Physical Review Letters*, 110(18):186403, May 2013.

[16] Kerry J. Vahala. Optical microcavities. *Nature*, 424(6950):839–846, August 2003.

[17] W. Y. Liang. Excitons. *Physics Education*, 5(4):226, 1970.

[18] J. Frenkel. On the Transformation of Light into Heat in Solids. II. *Physical Review*, 37(10):1276–1294, May 1931.

[19] Gregory H. Wannier. The Structure of Electronic Excitation Levels in Insulating Crystals. *Physical Review*, 52(3):191–197, August 1937.

[20] N. F. Mott. Conduction in polar crystals. II. The conduction band and ultraviolet absorption of alkali-halide crystals. *Transactions of the Faraday Society*, 34(0):500–506, January 1938.

[21] Claude Cohen-Tannoudji, Bernard Diu, and Frank Laloe. *Quantum Mechanics, Volume 1: Vol 1.* Wiley VCH, New York, volume 1 ed. edition edition, June 1977.

[22] Claude Cohen-Tannoudji, Bernard Diu, and Frank Laloe. *Quantum Mechanics, Volume 2: Vol 2*. Wiley VCH, New York, NY, 2nd volume 2 ed. edition edition, June 1977.

[23] Mark Fox and Radu Ispasoiu. Quantum Wells, Superlattices, and Band-Gap Engineering. In Safa Kasap Prof and Peter Capper Dr, editors, *Springer Handbook of Electronic and Photonic Materials*, pages 1021–1040. Springer US, 2006.

[24] D. a. B. Miller, D. S. Chemla, D. J. Eilenberger, P. W. Smith, A. C. Gossard, and W. T. Tsang. Large room-temperature optical nonlinearity in GaAs/Ga1-x AlxAs multiple quantum well structures. *Applied Physics Letters*, 41(8):679–681, October 1982.

[25] Masaki Shinada and Satoru Sugano. Interband Optical Transitions in Extremely Anisotropic Semiconductors. I. Bound and Unbound Exciton Absorption. *Journal of the Physical Society of Japan*, 21(10):1936–1946, October 1966.

[26] A. V. Kavokin. Exciton oscillator strength in quantum wells: From localized to free resonant states. *Physical Review B*, 50(11):8000–8003, September 1994.

[27] Vincenzo Savona. Effect of interface disorder on quantum well excitons and microcavity polaritons. *Journal of Physics: Condensed Matter*, 19(29):295208, 2007.

[28] Hui Deng, Hartmut Haug, and Yoshihisa Yamamoto. Exciton-polariton Bose-Einstein condensation. *Reviews of Modern Physics*, 82(2):1489–1537, May 2010.

[29] M. S. Skolnick, T. A. Fisher, and D. M. Whittaker. Strong coupling phenomena in quantum microcavity structures. *Semiconductor Science and Technology*, 13(7):645, 1998.

[30] Jonathan R. Tischler, M. Scott Bradley, Qiang Zhang, Tolga Atay, Arto Nurmikko, and Vladimir Bulović. Solid state cavity QED: Strong coupling in organic thin films. *Organic Electronics*, 8(2):94–113, April 2007.

[31] J. J. Hopfield. Theory of the Contribution of Excitons to the Complex Dielectric Constant of Crystals. *Physical Review*, 112(5):1555–1567, December 1958.

[32] V. Savona, L. C. Andreani, P. Schwendimann, and A. Quattropani. Quantum well excitons in semiconductor microcavities: Unified treatment of weak and strong coupling regimes. *Solid State Communications*, 93(9):733–739, March 1995.

[33] A. I. Tartakovskii, M. S. Skolnick, D. N. Krizhanovskii, V. D. Kulakovskii, R. M. Stevenson, R. Butté, J. J. Baumberg, D. M. Whittaker, and J. S. Roberts. Stimulated Polariton Scattering in Semiconductor Microcavities: New Physics and Potential Applications. *Advanced Materials*, 13(22):1725–1730, November 2001.

[34] M. Z. Maialle, E. A. de Andrada e Silva, and L. J. Sham. Exciton spin dynamics in quantum wells. *Physical Review B*, 47(23):15776–15788, June 1993.

[35] Hui Deng, Gregor Weihs, David Snoke, Jacqueline Bloch, and Yoshihisa Yamamoto. Polariton lasing vs. photon lasing in a semiconductor microcavity. *Proceedings of the National Academy of Sciences*, 100(26):15318–15323, December 2003.

[36] F. Tassone, C. Piermarocchi, V. Savona, A. Quattropani, and P. Schwendimann. Bottleneck effects in the relaxation and photoluminescence of microcavity polaritons. *Physical Review B*, 56(12):7554–7563, September 1997.

[37] Bose. Plancks Gesetz und Lichtquantenhypothese. *Zeitschrift für Physik*, 26(1):178–181, December 1924.

[38] A. Einstein. Quantentheorie des einatomigen idealen Gases. *Sitzungsberichte der Preussischen Akademie der Wissenschaften, Physikalisch-mathematische Klasse*, 1924.

[39] M. H. Anderson, J. R. Ensher, M. R. Matthews, C. E. Wieman, and E. A. Cornell. Observation of Bose-Einstein Condensation in a Dilute Atomic Vapor. *Science*, 269(5221):198–201, July 1995.

[40] K. B. Davis, M. O. Mewes, M. R. Andrews, N. J. van Druten, D. S. Durfee, D. M. Kurn, and W. Ketterle. Bose-Einstein Condensation in a Gas of Sodium Atoms. *Physical Review Letters*, 75(22):3969–3973, November 1995.

[41] C. C. Bradley, C. A. Sackett, J. J. Tollett, and R. G. Hulet. Evidence of Bose-Einstein Condensation in an Atomic Gas with Attractive Interactions. *Physical Review Letters*, 75(9):1687–1690, August 1995.

[42] L. V. Butov, C. W. Lai, A. L. Ivanov, A. C. Gossard, and D. S. Chemla. Towards Bose–Einstein condensation of excitons in potential traps. *Nature*, 417(6884):47–52, May 2002.

[43] Le Si Dang, D. Heger, R. André, F. Bø euf, and R. Romestain. Stimulation of Polariton Photoluminescence in Semiconductor Microcavity. *Physical Review Letters*, 81(18):3920–3923, November 1998.

[44] Hui Deng, Gregor Weihs, Charles Santori, Jacqueline Bloch, and Yoshihisa Yamamoto. Condensation of Semiconductor Microcavity Exciton Polaritons. *Science*, 298(5591):199–202, October 2002.

[45] Feng Li, L. Orosz, O. Kamoun, S. Bouchoule, C. Brimont, P. Disseix, T. Guillet, X. Lafosse, M. Leroux, J. Leymarie, M. Mexis, M. Mihailovic, G. Patriarche, F. Réveret, D. Solnyshkov, J. Zuniga-Perez, and G. Malpuech. From Excitonic to Photonic Polariton Condensate in a ZnO-Based Microcavity. *Physical Review Letters*, 110(19):196406, May 2013.

[46] K. S. Daskalakis, S. A. Maier, R. Murray, and S. Kéna-Cohen. Nonlinear interactions in an organic polariton condensate. *Nature Materials*, 13(3):271–278, March 2014.

[47] Johannes D. Plumhof, Thilo Stöferle, Lijian Mai, Ullrich Scherf, and Rainer F. Mahrt. Room-temperature Bose–Einstein condensation of cavity exciton–polaritons in a polymer. *Nature Materials*, 13(3):247–252, March 2014.

[48] Tamsin Cookson, Kyriacos Georgiou, Anton Zasedatelev, Richard T. Grant, Tersilla Virgili, Marco Cavazzini, Francesco Galeotti, Caspar Clark, Natalia G. Berloff, David G. Lidzey, and Pavlos G. Lagoudakis. A Yellow Polariton Condensate in a Dye Filled Microcavity. *Advanced Optical Materials*, July 2017.

[49] W. Ketterle, D. S. Durfee, and D. M. Stamper-Kurn. Making, probing and understanding Bose-Einstein condensates. *arXiv:cond-mat/9904034*, April 1999. arXiv: cond-mat/9904034.

[50] Oliver Penrose and Lars Onsager. Bose-Einstein Condensation and Liquid Helium. *Physical Review*, 104(3):576–584, November 1956.

[51] A. Griffin, D. W. Snoke, and S. Stringari. *Bose-Einstein Condensation*. Cambridge University Press, July 1996. Google-Books-ID: suqJdr2pPIsC.

[52] C. N. Yang. Concept of Off-Diagonal Long-Range Order and the Quantum Phases of Liquid He and of Superconductors. *Reviews of Modern Physics*, 34(4):694–704, October 1962.

[53] G. Malpuech, Y. G. Rubo, F. P. Laussy, P. Bigenwald, and A. V. Kavokin. Polariton laser: thermodynamics and quantum kinetic theory. *Semiconductor Science and Technology*, 18(10):S395, 2003.

[54] D. S. Petrov, D. M. Gangardt, and G. V. Shlyapnikov. Low-dimensional trapped gases. *Journal de Physique IV (Proceedings)*, 116:5–44, October 2004.

[55] N. D. Mermin and H. Wagner. Absence of Ferromagnetism or Antiferromagnetism in One- or Two-Dimensional Isotropic Heisenberg Models. *Physical Review Letters*, 17(26):1307–1307, December 1966.

[56] P. C. Hohenberg. Existence of Long-Range Order in One and Two Dimensions. *Physical Review*, 158(2):383–386, June 1967.

[57] V.L. Berezinskii. Destruction of Long-range Order in One-dimensional and Two-dimensional Systems having a Continuous Symmetry Group I. Classical Systems. *Journal of Experimental and Theoretical Physics*, 32:493, March 1971.

[58] V.L. Berezinskii. Destruction of Long-range Order in One-dimensional and Two-dimensional Systems Possessing a Continuous Symmetry Group. II. Quantum Systems. *Journal of Experimental and Theoretical Physics*, 34:610, March 1972.

[59] Vanderlei Bagnato and Daniel Kleppner. Bose-Einstein condensation in low-dimensional traps. *Physical Review A*, 44(11):7439–7441, December 1991.

[60] D. S. Petrov, M. Holzmann, and G. V. Shlyapnikov. Bose-Einstein Condensation in Quasi-2d Trapped Gases. *Physical Review Letters*, 84(12):2551–2555, March 2000.

[61] J. M. Kosterlitz and D. J. Thouless. Ordering, metastability and phase transitions in two-dimensional systems. *Journal of Physics C: Solid State Physics*, 6(7):1181, 1973.

[62] L. Landau. Theory of the Superfluidity of Helium II. *Physical Review*, 60(4):356–358, August 1941.

[63] N. Bogoliubov. On the theory of superfluidity. *Journal of Physics*, 11(1):23, 1947.

[64] P. Kapitza. Viscosity of Liquid Helium below the λ-Point. *Nature*, 1938.

[65] J.F. Allen and A.D. Misener. Flow of Liquid Helium II. *Nature*, 1938.

[66] F London. The λ-Phenomenon of Liquid Helium and the Bose-Einstein Degeneracy. *Nature*, 1938.

[67] T. R. Sosnick, W. M. Snow, and P. E. Sokol. Deep-inelastic neutron scattering from liquid $ˆ{4}\mathrm{He}$. *Physical Review B*, 41(16):11185–11202, June 1990.

[68] Stefano Giorgini. Lecture Notes on Statistical Mechanics, February 2014.

[69] S. Utsunomiya, L. Tian, G. Roumpos, C. W. Lai, N. Kumada, T. Fujisawa, M. Kuwata-Gonokami, A. Löffler, S. Höfling, A. Forchel, and Y. Yamamoto. Observation of Bogoliubov excitations in exciton-polariton condensates. *Nature Physics*, 4(9):700–705, September 2008.

[70] A. Amo, D. Sanvitto, F. P. Laussy, D. Ballarini, E. del Valle, M. D. Martin, A. Lemaître, J. Bloch, D. N. Krizhanovskii, M. S. Skolnick, C. Tejedor, and L. Viña. Collective fluid dynamics of a polariton condensate in a semiconductor microcavity. *Nature*, 457(7227):291–295, January 2009.

[71] K. G. Lagoudakis, M. Wouters, M. Richard, A. Baas, I. Carusotto, R. André, Le Si Dang, and B. Deveaud-Plédran. Quantized vortices in an exciton–polariton condensate. *Nature Physics*, 4(9):706–710, September 2008.

[72] K. G. Lagoudakis, T. Ostatnický, A. V. Kavokin, Y. G. Rubo, R. André, and B. Deveaud-Plédran. Observation of Half-Quantum Vortices in an Exciton-Polariton Condensate. *Science*, 326(5955):974–976, November 2009.

[73] Georgios Roumpos, Michael D. Fraser, Andreas Löffler, Sven Höfling, Alfred Forchel, and Yoshihisa Yamamoto. Single vortex-antivortex pair in an exciton-polariton condensate. *Nature Physics*, 7(2):129–133, February 2011.

[74] Gaël Nardin, Gabriele Grosso, Yoan Léger, Barbara Pi?tka, François Morier-Genoud, and Benoît Deveaud-Plédran. Hydrodynamic nucleation of quantized vortex pairs in a polariton quantum fluid. *Nature Physics*, 7(8):635–641, August 2011.

[75] D. Sanvitto, F. M. Marchetti, M. H. Szymańska, G. Tosi, M. Baudisch, F. P. Laussy, D. N. Krizhanovskii, M. S. Skolnick, L. Marrucci, A. Lemaître, J. Bloch, C. Tejedor, and L. Viña. Persistent currents and quantized vortices in a polariton superfluid. *Nature Physics*, 6(7):527–533, July 2010.

[76] D. N. Krizhanovskii, D. M. Whittaker, R. A. Bradley, K. Guda, D. Sarkar, D. Sanvitto, L. Vina, E. Cerda, P. Santos, K. Biermann, R. Hey, and M. S. Skolnick. Effect of Interactions on Vortices in a Nonequilibrium Polariton Condensate. *Physical Review Letters*, 104(12):126402, March 2010.

[77] G. Tosi, G. Christmann, N. G. Berloff, P. Tsotsis, T. Gao, Z. Hatzopoulos, P. G. Savvidis, and J. J. Baumberg. Geometrically locked vortex lattices in semiconductor quantum fluids. *Nature Communications*, 3:ncomms2255, December 2012.

[78] T. Boulier, E. Cancellieri, N. D. Sangouard, Q. Glorieux, A. V. Kavokin, D. M. Whittaker, E. Giacobino, and A. Bramati. Injection of Orbital Angular Momentum and Storage of Quantized Vortices in Polariton Superfluids. *Physical Review Letters*, 116(11):116402, March 2016.

[79] Tim Byrnes, Na Young Kim, and Yoshihisa Yamamoto. Exciton-polariton condensates. *Nature Physics*, 10(11):803–813, November 2014.

[80] A. Imamoglu, R. J. Ram, S. Pau, and Y. Yamamoto. Nonequilibrium condensates and lasers without inversion: Exciton-polariton lasers. *Physical Review A*, 53(6):4250–4253, June 1996.

[81] J. Kasprzak, D. D. Solnyshkov, R. André, Le Si Dang, and G. Malpuech. Formation of an Exciton Polariton Condensate: Thermodynamic versus Kinetic Regimes. *Physical Review Letters*, 101(14):146404, October 2008.

[82] Yongbao Sun, Patrick Wen, Yoseob Yoon, Gangqiang Liu, Mark Steger, Loren N. Pfeiffer, Ken West, David W. Snoke, and Keith A. Nelson. Bose-Einstein Condensation of Long-Lifetime Polaritons in Thermal Equilibrium. *Physical Review Letters*, 118(1):016602, January 2017.

[83] Michiel Wouters and Iacopo Carusotto. Excitations in a Nonequilibrium Bose-Einstein Condensate of Exciton Polaritons. *Physical Review Letters*, 99(14):140402, October 2007.

[84] Jonathan Keeling and Natalia G. Berloff. Spontaneous Rotating Vortex Lattices in a Pumped Decaying Condensate. *Physical Review Letters*, 100(25):250401, June 2008.

[85] N. G. Berloff and J. Keeling. Universality in Modelling Non-equilibrium Pattern Formation in Polariton Condensates. In *Physics of Quantum Fluids*, Springer Series in Solid-State Sciences, pages 19–38. Springer, Berlin, Heidelberg, 2013. DOI: 10.1007/978-3-642-37569-9_2.

[86] Michiel Wouters, Iacopo Carusotto, and Cristiano Ciuti. Spatial and spectral shape of inhomogeneous nonequilibrium exciton-polariton condensates. *Physical Review B*, 77(11):115340, March 2008.

[87] Princeton Instruments. IntelliCal Spectral Calibration System.

[88] L. Burger. *Novel implementation of a phase-only spatial light modulator for laser beam shaping*. PhD thesis, Stellenbosch University, 2016.

[89] Deng-Ke Yang. *Fundamentals of Liquid Crystal Devices*. John Wiley & Sons, December 2014.

[90] Hartmann Römer. *Theoretical Optics: An Introduction*. John Wiley & Sons, March 2006.

[91] HOLOEYE Photonics AG. PLUTO Phase Only Spatial Light Modulator (Reflective).

[92] HOLOEYE Photonics AG. LC 2012 Spatial Light Modulator (transmissive).

[93] Bahaa E. A. Saleh and Malvin Carl Teich. *Fundamentals of Photonics*. Wiley-Interscience, Hoboken, N.J, 2 edizione edition, April 2007.

[94] J. R. Fienup. Reconstruction of an object from the modulus of its Fourier transform. *Optics Letters*, 3(1):27–29, July 1978.

[95] J. R. Fienup. Phase retrieval algorithms: a comparison. *Applied Optics*, 21(15):2758–2769, August 1982.

[96] Veit Elser. Phase retrieval by iterated projections. *JOSA A*, 20(1):40–55, January 2003.

[97] Wim Coene, Guido Janssen, Marc Op de Beeck, and Dirk Van Dyck. Phase retrieval through focus variation for ultra-resolution in field-emission transmission electron microscopy. *Physical Review Letters*, 69(26):3743–3746, December 1992.

[98] Franz Pfeiffer, Timm Weitkamp, Oliver Bunk, and Christian David. Phase retrieval and differential phase-contrast imaging with low-brilliance X-ray sources. *Nature Physics*, 2(4):258–261, April 2006.

[99] Robert A. Gonsalves. Phase Retrieval And Diversity In Adaptive Optics. *Optical Engineering*, 21(5):215829–215829–, 1982.

[100] Michael A. Seldowitz, Jan P. Allebach, and Donald W. Sweeney. Synthesis of digital holograms by direct binary search. *Applied Optics*, 26(14):2788–2798, July 1987.

[101] R.W. Gerchberg W.O. Saxton. A practical algorithm for the determination of phase from image and diffraction plane pictures. *Optik*, 35:237–246, 1972.

[102] J. R. Fienup. Iterative Method Applied To Image Reconstruction And To Computer-Generated Holograms. In *Applications of Digital Image Processing III*, volume 0207, pages 2–13, 1979.

[103] D. Prongué, H. P. Herzig, R. Dändliker, and M. T. Gale. Optimized kinoform structures for highly efficient fan-out elements. *Applied Optics*, 31(26):5706–5711, September 1992.

[104] Victor Arrizón, Markus Testorf, Stefan Sinzinger, and Jürgen Jahns. Iterative optimization of phase-only diffractive optical elements based on a lenslet array. *JOSA A*, 17(12):2157–2164, December 2000.

[105] Matthew Pasienski and Brian DeMarco. A high-accuracy algorithm for designing arbitrary holographic atom traps. *Optics Express*, 16(3):2176–2190, February 2008.

[106] Alexander L. Gaunt and Zoran Hadzibabic. Robust Digital Holography For Ultracold Atom Trapping. *Scientific Reports*, 2:721, October 2012.

[107] Hui Pang, Jiazhou Wang, Axiu Cao, and Qiling Deng. High-accuracy method for holographic image projection with suppressed speckle noise. *Optics Express*, 24(20):22766–22776, October 2016.

[108] R. Bowman, V. D'Ambrosio, E. Rubino, O. Jedrkiewicz, P. Di Trapani, and M. J. Padgett. Optimisation of a low cost SLM for diffraction efficiency and ghost order suppression. *The European Physical Journal Special Topics*, 199(1):149–158, November 2011.

[109] Stephan Reichelt, Ralf Häussler, Gerald Fütterer, Norbert Leister, Hiromi Kato, Naru Usukura, and Yuuichi Kanbayashi. Full-range, complex spatial light modulator for real-time holography. *Optics Letters*, 37(11):1955–1957, June 2012.

[110] Stephan Reichelt and Norbert Leister. Computational hologram synthesis and representation on spatial light modulators for real-time 3d holographic imaging. *Journal of Physics: Conference Series*, 415(1):012038, 2013.

[111] Jonathan Leach, Kurt Wulff, Gavin Sinclair, Pamela Jordan, Johannes Courtial, Laura Thomson, Graham Gibson, Kayode Karunwi, Jon Cooper, Zsolt John

Laczik, and Miles Padgett. Interactive approach to optical tweezers control. *Applied Optics*, 45(5):897–903, February 2006.

[112] Gabriel Milewski, David Engström, and Jörgen Bengtsson. Diffractive optical elements designed for highly precise far-field generation in the presence of artifacts typical for pixelated spatial light modulators. *Applied Optics*, 46(1):95–105, January 2007.

[113] H. Nyquist. Certain Topics in Telegraph Transmission Theory. *Transactions of the American Institute of Electrical Engineers*, 47(2):617–644, April 1928.

[114] C. E. Shannon. Communication in the presence of noise. *Proceedings of the IEEE*, 72(9):1192–1201, September 1984.

[115] R. Clark Jones. A New Calculus for the Treatment of Optical SystemsI. Description and Discussion of the Calculus. *JOSA*, 31(7):488–493, July 1941.

[116] Bahaa E. A. Saleh and Kanghua Lu. Theory and design of the liquid crystal TV as an optical spatial phase modulator. *Optical Engineering*, 29(3):240–246, 1990.

[117] I. Moreno, P. Velásquez, C. R. Fernández-Pousa, M. M. Sánchez-López, and F. Mateos. Jones matrix method for predicting and optimizing the optical modulation properties of a liquid-crystal display. *Journal of Applied Physics*, 94(6):3697–3702, August 2003.

[118] Julian D. Toepfer. *Engineering Polariton Graphs*. PhD thesis, Karlsruhe Institute of Technology, 2016.

[119] Vicente Durán, Jesús Lancis, Enrique Tajahuerce, and Zbigniew Jaroszewicz. Equivalent retarder-rotator approach to on-state twisted nematic liquid crystal displays. *Journal of Applied Physics*, 99(11):113101, June 2006.

[120] B. Richards and E. Wolf. Electromagnetic Diffraction in Optical Systems. II. Structure of the Image Field in an Aplanatic System. *Proceedings of the Royal Society of London A: Mathematical, Physical and Engineering Sciences*, 253(1274):358–379, December 1959.

[121] I. Shelykh, K. V. Kavokin, A. V. Kavokin, G. Malpuech, P. Bigenwald, H. Deng, G. Weihs, and Y. Yamamoto. Semiconductor microcavity as a spin-dependent optoelectronic device. *Physical Review B*, 70(3):035320, July 2004.

[122] Eugene Hecht. *Optics*. Addison-Wesley, Reading, Mass, 4 edition edition, August 2001.

[123] Ioffe Physico-Technical Institute. New Semiconductor Materials. Characteristics and Properties.

[124] Joanna M. Zajac, Wolfgang Langbein, Maxime Hugues, and Mark Hopkinson. Polariton states bound to defects in GaAs/AlAs planar microcavities. *Physical Review B*, 85(16):165309, April 2012.

[125] M. Gurioli, F. Bogani, D. S. Wiersma, Ph. Roussignol, G. Cassabois, G. Khitrova, and H. Gibbs. Experimental study of disorder in a semiconductor microcavity. *Physical Review B*, 64(16):165309, October 2001.

[126] Wolfgang Langbein and Jørn M. Hvam. Elastic Scattering Dynamics of Cavity Polaritons: Evidence for Time-Energy Uncertainty and Polariton Localization. *Physical Review Letters*, 88(4):047401, January 2002.

[127] Wolfgang Langbein. Energy and momentum broadening of planar microcavity polaritons measured by resonant light scattering. *Journal of Physics: Condensed Matter*, 16(35):S3645, 2004.

[128] Marco Abbarchi, Carole Diederichs, Ludovic Largeau, Vincenzo Ardizzone, Olivia Mauguin, Timothee Lecomte, Aristide Lemaitre, Jacqueline Bloch, Philippe Roussignol, and Jerome Tignon. Discretized disorder in planar semiconductor microcavities: Mosaicity effect on resonant Rayleigh scattering and optical parametric oscillation. *Physical Review B*, 85(4):045316, January 2012.

[129] L. Tinkler, P. M. Walker, E. Clarke, D. N. Krizhanovskii, F. Bastiman, M. Durska, and M. S. Skolnick. Design and characterization of high optical quality InGaAs/GaAs/AlGaAs-based polariton microcavities. *Applied Physics Letters*, 106(2):021109, January 2015.

[130] C. Ouellet-Plamondon, G. Sallen, F. Jabeen, D. Y. Oberli, and B. Deveaud. Multiple polariton modes originating from the coupling of quantum wells in planar microcavity. *Physical Review B*, 92(7):075313, August 2015.

[131] Joanna M. Zajac, Edmund Clarke, and Wolfgang Langbein. Suppression of cross-hatched polariton disorder in GaAs/AlAs microcavities by strain compensation. *Applied Physics Letters*, 101(4):041114, July 2012.

[132] R. Houdré, J. L. Gibernon, P. Pellandini, R. P. Stanley, U. Oesterle, C. Weisbuch, J. O'Gorman, B. Roycroft, and M. Ilegems. Saturation of the strong-coupling regime in a semiconductor microcavity: Free-carrier bleaching of cavity polaritons. *Physical Review B*, 52(11):7810–7813, September 1995.

[133] Leonid V. Butov. Solid-state physics: A polariton laser. *Nature*, 447(7144):540–541, May 2007.

[134] L. V. Butov and A. V. Kavokin. The behaviour of exciton-polaritons. *Nature Photonics*, 6(1):2–2, January 2012.

[135] Benoít Deveaud-Plédran. The behaviour of exciton-polaritons. *Nature Photonics*, 6(4):205–205, April 2012.

[136] Daniele Bajoni, Pascale Senellart, Aristide Lemaître, and Jacqueline Bloch. Photon lasing in $\textbackslashtextbackslashmathrm{GaAs}$ microcavity: Similarities with a polariton condensate. *Physical Review B*, 76(20):201305, November 2007.

[137] A. Askitopoulos, H. Ohadi, A. V. Kavokin, Z. Hatzopoulos, P. G. Savvidis, and P. G. Lagoudakis. Polariton condensation in an optically induced two-dimensional potential. *Physical Review B*, 88(4):041308, July 2013.

[138] Elena Kammann, Hamid Ohadi, Maria Maragkou, Alexey V. Kavokin, and Pavlos G. Lagoudakis. Crossover from photon to exciton-polariton lasing. *New Journal of Physics*, 14(10):105003, 2012.

[139] Maurice G. A. Bernard and Georges Duraffourg. Laser Conditions in Semiconductors. *physica status solidi (b)*, 1(7):699–703, January 1961.

[140] P. Cilibrizzi, H. Ohadi, T. Ostatnicky, A. Askitopoulos, W. Langbein, and P. Lagoudakis. Linear Wave Dynamics Explains Observations Attributed to Dark Solitons in a Polariton Quantum Fluid. *Physical Review Letters*, 113(10):103901, September 2014.

[141] Niles A. Pierce and Erik Winfree. Protein Design is NP-hard. *Protein Engineering*, 15(10):779–782, October 2002.

[142] Steven N. Durlauf. How can statistical mechanics contribute to social science? *Proceedings of the National Academy of Sciences of the United States of America*, 96(19):10582–10584, September 1999.

[143] Raul Rojas. *Neural Networks: A Systematic Introduction*. Springer Science & Business Media, June 2013.

[144] Onn Shehory and Sarit Kraus. Methods for task allocation via agent coalition formation. *Artificial Intelligence*, 101(1):165–200, May 1998.

[145] Luca M. Ghiringhelli, Jan Vybiral, Sergey V. Levchenko, Claudia Draxl, and Matthias Scheffler. Big Data of Materials Science: Critical Role of the Descriptor. *Physical Review Letters*, 114(10):105503, March 2015.

[146] Leon Balents. Spin liquids in frustrated magnets. *Nature*, 464(7286):199–208, March 2010.

[147] Richard P. Feynman. Simulating physics with computers. *International Journal of Theoretical Physics*, 21(6-7):467–488, June 1982.

[148] Tomi H. Johnson, Stephen R. Clark, and Dieter Jaksch. What is a quantum simulator? *EPJ Quantum Technology*, 1(1):10, July 2014.

[149] Gemma De las Cuevas and Toby S. Cubitt. Simple universal models capture all classical spin physics. *Science*, 351(6278):1180–1183, March 2016.

[150] M. W. Johnson, M. H. S. Amin, S. Gildert, T. Lanting, F. Hamze, N. Dickson, R. Harris, A. J. Berkley, J. Johansson, P. Bunyk, E. M. Chapple, C. Enderud, J. P. Hilton, K. Karimi, E. Ladizinsky, N. Ladizinsky, T. Oh, I. Perminov, C. Rich, M. C. Thom, E. Tolkacheva, C. J. S. Truncik, S. Uchaikin, J. Wang, B. Wilson, and G. Rose. Quantum annealing with manufactured spins. *Nature*, 473(7346):194–198, May 2011.

[151] J. Struck, C. Ölschläger, R. Le Targat, P. Soltan-Panahi, A. Eckardt, M. Lewenstein, P. Windpassinger, and K. Sengstock. Quantum Simulation of Frustrated Classical Magnetism in Triangular Optical Lattices. *Science*, 333(6045):996–999, August 2011.

[152] Micha Nixon, Eitan Ronen, Asher A. Friesem, and Nir Davidson. Observing Geometric Frustration with Thousands of Coupled Lasers. *Physical Review Letters*, 110(18):184102, May 2013.

[153] Shoko Utsunomiya, Kenta Takata, and Yoshihisa Yamamoto. Mapping of Ising models onto injection-locked laser systems. *Optics Express*, 19(19):18091–18108, September 2011.

[154] Alireza Marandi, Zhe Wang, Kenta Takata, Robert L. Byer, and Yoshihisa Yamamoto. Network of time-multiplexed optical parametric oscillators as a coherent Ising machine. *Nature Photonics*, 8(12):937–942, December 2014.

[155] Hiromasa Sakaguchi, Koji Ogata, Tetsu Isomura, Shoko Utsunomiya, Yoshihisa Yamamoto, and Kazuyuki Aihara. Boltzmann Sampling by Degenerate Optical Parametric Oscillator Network for Structure-Based Virtual Screening. *Entropy*, 18(10):365, October 2016.

[156] Takahiro Inagaki, Yoshitaka Haribara, Koji Igarashi, Tomohiro Sonobe, Shuhei Tamate, Toshimori Honjo, Alireza Marandi, Peter L. McMahon, Takeshi Umeki, Koji Enbutsu, Osamu Tadanaga, Hirokazu Takenouchi, Kazuyuki Aihara, Ken-ichi Kawarabayashi, Kyo Inoue, Shoko Utsunomiya, and Hiroki Takesue. A coherent Ising machine for 2000-node optimization problems. *Science*, page aah4243, October 2016.

[157] K. Kim, M.-S. Chang, S. Korenblit, R. Islam, E. E. Edwards, J. K. Freericks, G.-D. Lin, L.-M. Duan, and C. Monroe. Quantum simulation of frustrated Ising spins with trapped ions. *Nature*, 465(7298):590–593, June 2010.

[158] Imran Mahboob, Hajime Okamoto, and Hiroshi Yamaguchi. An electromechanical Ising Hamiltonian. *Science Advances*, 2(6):e1600236, June 2016.

[159] Pallab Bhattacharya, Thomas Frost, Saniya Deshpande, Md Zunaid Baten, Arnab Hazari, and Ayan Das. Room Temperature Electrically Injected Polariton Laser. *Physical Review Letters*, 112(23):236802, June 2014.

[160] Álvaro Cuevas, Blanca Silva, Juan Camilo López Carreño, Milena de Giorgi, Carlos Sánchez Muñoz, Antonio Fieramosca, Daniel Gustavo Suárez Forero, Filippo Cardano, Lorenzo Marrucci, Vittorianna Tasco, Giorgio Biasiol, Elena del Valle, Lorenzo Dominici, Dario Ballarini, Giuseppe Gigli, Paolo Mataloni, Fabrice P. Laussy, Fabio Sciarrino, and Daniele Sanvitto. Entangling one polariton with a photon: effect of interactions on a single-polariton quantum state. *arXiv:1609.01244 [cond-mat, physics:physics, physics:quant-ph]*, September 2016. arXiv: 1609.01244.

[161] Michael Rubinstein, Boris Shraiman, and David R. Nelson. Two-dimensional XY magnets with random Dzyaloshinskii-Moriya interactions. *Physical Review B*, 27(3):1800–1811, February 1983.

[162] Zohar Nussinov and Jeroen van den Brink. Compass models: Theory and physical motivations. *Reviews of Modern Physics*, 87(1):1–59, January 2015.

[163] Robert Dall, Michael D. Fraser, Anton S. Desyatnikov, Guangyao Li, Sebastian Brodbeck, Martin Kamp, Christian Schneider, Sven Höfling, and Elena A. Ostrovskaya. Creation of Orbital Angular Momentum States with Chiral Polaritonic Lenses. *Physical Review Letters*, 113(20):200404, November 2014.

[164] E. J. Yarmchuk, M. J. V. Gordon, and R. E. Packard. Observation of Stationary Vortex Arrays in Rotating Superfluid Helium. *Physical Review Letters*, 43(3):214–217, July 1979.

[165] A. A. Abrikosov. The magnetic properties of superconducting alloys. *Journal of Physics and Chemistry of Solids*, 2(3):199–208, January 1957.

[166] Pål Erik Goa, Harald Hauglin, Michael Baziljevich, Eugene Il'yashenko, Peter L. Gammel, and Tom H. Johansen. Real-time magneto-optical imaging of vortices in superconducting NbSe 2. *Superconductor Science and Technology*, 14(9):729, 2001.

[167] K. W. Madison, F. Chevy, W. Wohlleben, and J. Dalibard. Vortex Formation in a Stirred Bose-Einstein Condensate. *Physical Review Letters*, 84(5):806–809, January 2000.

[168] C. J. Pethick and H. Smith. *Bose-Einstein Condensation in Dilute Gases*. Cambridge University Press, 2002. Google-Books-ID: iBk0G3_5iIQC.

[169] Emil Lundh. Multiply quantized vortices in trapped Bose-Einstein condensates. *Physical Review A*, 65(4):043604, March 2002.

[170] Vincent Bretin, Sabine Stock, Yannick Seurin, and Jean Dalibard. Fast Rotation of a Bose-Einstein Condensate. *Physical Review Letters*, 92(5):050403, February 2004.

[171] R. Blaauwgeers, V. B. Eltsov, M. Krusius, J. J. Ruohio, R. Schanen, and G. E. Volovik. Double-quantum vortex in superfluid 3he-A. *Nature*, 404(6777):471–473, March 2000.

[172] A. Kanda, B. J. Baelus, F. M. Peeters, K. Kadowaki, and Y. Ootuka. Experimental Evidence for Giant Vortex States in a Mesoscopic Superconducting Disk. *Physical Review Letters*, 93(25):257002, December 2004.

[173] Dragomir N. Neshev, Tristram J. Alexander, Elena A. Ostrovskaya, Yuri S. Kivshar, Hector Martin, Igor Makasyuk, and Zhigang Chen. Observation of Discrete Vortex Solitons in Optically Induced Photonic Lattices. *Physical Review Letters*, 92(12):123903, March 2004.

[174] Jason W. Fleischer, Guy Bartal, Oren Cohen, Ofer Manela, Mordechai Segev, Jared Hudock, and Demetrios N. Christodoulides. Observation of Vortex-Ring "Discrete" Solitons in 2d Photonic Lattices. *Physical Review Letters*, 92(12):123904, March 2004.

[175] B. A. Malomed and P. G. Kevrekidis. Discrete vortex solitons. *Physical Review E*, 64(2):026601, July 2001.

[176] Bernd Terhalle, Tobias Richter, Anton S. Desyatnikov, Dragomir N. Neshev, Wieslaw Krolikowski, Friedemann Kaiser, Cornelia Denz, and Yuri S. Kivshar. Observation of Multivortex Solitons in Photonic Lattices. *Physical Review Letters*, 101(1):013903, July 2008.

[177] Pal V, Trandonsky C, Chriki R, Barach G, Friesem Aa, and Davidson N. Phase locking of even and odd number of lasers on a ring geometry: effects of topological-charge. *Optics Express*, 23(10):13041–13050, May 2015.

[178] Shuhei Tamate, Yoshihisa Yamamoto, Alireza Marandi, Peter McMahon, and Shoko Utsunomiya. Simulating the classical XY model with a laser network. *arXiv:1608.00358 [physics, physics:quant-ph]*, August 2016. arXiv: 1608.00358.

[179] Vishwa Pal, Chene Tradonsky, Ronen Chriki, Asher A. Friesem, and Nir Davidson. Observing Dissipative Topological Defects with Coupled Lasers. *Physical Review Letters*, 119(1):013902, July 2017.

[180] R. Idrissi Kaitouni, O. El Daïf, A. Baas, M. Richard, T. Paraiso, P. Lugan, T. Guillet, F. Morier-Genoud, J. D. Ganière, J. L. Staehli, V. Savona, and B. Deveaud.

Engineering the spatial confinement of exciton polaritons in semiconductors. *Physical Review B*, 74(15):155311, October 2006.

[181] Karol Winkler, Julian Fischer, Anne Schade, Matthias Amthor, Robert Dall, Jonas Geßler, Monika Emmerling, Elena A. Ostrovskaya, Martin Kamp, Christian Schneider, and Sven Höfling. A polariton condensate in a photonic crystal potential landscape. *New Journal of Physics*, 17(2):023001, 2015.

[182] M. Abbarchi, A. Amo, V. G. Sala, D. D. Solnyshkov, H. Flayac, L. Ferrier, I. Sagnes, E. Galopin, A. Lemaître, G. Malpuech, and J. Bloch. Macroscopic quantum self-trapping and Josephson oscillations of exciton polaritons. *Nature Physics*, 9(5):275–279, May 2013.

[183] V. G. Sala, D. D. Solnyshkov, I. Carusotto, T. Jacqmin, A. Lemaître, H. Terças, A. Nalitov, M. Abbarchi, E. Galopin, I. Sagnes, J. Bloch, G. Malpuech, and A. Amo. Spin-Orbit Coupling for Photons and Polaritons in Microstructures. *Physical Review X*, 5(1):011034, March 2015.

[184] C. W. Lai, N. Y. Kim, S. Utsunomiya, G. Roumpos, H. Deng, M. D. Fraser, T. Byrnes, P. Recher, N. Kumada, T. Fujisawa, and Y. Yamamoto. Coherent zero-state and π-state in an exciton–polariton condensate array. *Nature*, 450(7169):529–532, November 2007.

[185] Na Young Kim, Kenichiro Kusudo, Congjun Wu, Naoyuki Masumoto, Andreas Löffler, Sven Höfling, Norio Kumada, Lukas Worschech, Alfred Forchel, and Yoshihisa Yamamoto. Dynamical d-wave condensation of exciton-polaritons in a two-dimensional square-lattice potential. *Nature Physics*, 7(9):681–686, September 2011.

[186] Naoyuki Masumoto, Na Young Kim, Tim Byrnes, Kenichiro Kusudo, Andreas Löffler, Sven Höfling, Alfred Forchel, and Yoshihisa Yamamoto. Exciton–polariton condensates with flat bands in a two-dimensional kagome lattice. *New Journal of Physics*, 14(6):065002, 2012.

[187] N. Y. Kim, K. Kusudo, A. Löffler, S. Höfling, A. Forchel, and Y. Yamamoto. Exciton–polariton condensates near the Dirac point in a triangular lattice. *New Journal of Physics*, 15(3):035032, 2013.

[188] Kenichiro Kusudo, Na Young Kim, Andreas Löffler, Sven Höfling, Alfred Forchel, and Yoshihisa Yamamoto. Stochastic formation of polariton condensates in two degenerate orbital states. *Physical Review B*, 87(21):214503, June 2013.

[189] H. Ohadi, Y. del Valle-Inclan Redondo, A. Dreismann, Y. G. Rubo, F. Pinsker, S. I. Tsintzos, Z. Hatzopoulos, P. G. Savvidis, and J. J. Baumberg. Tunable Magnetic Alignment between Trapped Exciton-Polariton Condensates. *Physical Review Letters*, 116(10):106403, March 2016.

[190] H. Ohadi, A. J. Ramsay, H. Sigurdsson, Y. del Valle-Inclan Redondo, S. I. Tsintzos, Z. Hatzopoulos, T. C. H. Liew, I. A. Shelykh, Y. G. Rubo, P. G. Savvidis, and J. J. Baumberg. Spin Order and Phase Transitions in Chains of Polariton Condensates. *Physical Review Letters*, 119(6):067401, August 2017.

[191] I. M. Georgescu, S. Ashhab, and Franco Nori. Quantum simulation. *Reviews of Modern Physics*, 86(1):153–185, March 2014.

[192] J. Kasprzak, R. André, Le Si Dang, I. A. Shelykh, A. V. Kavokin, Yuri G. Rubo, K. V. Kavokin, and G. Malpuech. Build up and pinning of linear polarization in the Bose condensates of exciton polaritons. *Physical Review B*, 75(4):045326, January 2007.

[193] I. Shelykh, G. Malpuech, K. V. Kavokin, A. V. Kavokin, and P. Bigenwald. Spin dynamics of interacting exciton polaritons in microcavities. *Physical Review B*, 70(11):115301, September 2004.

[194] J. J. Baumberg, A. V. Kavokin, S. Christopoulos, A. J. D. Grundy, R. Butté, G. Christmann, D. D. Solnyshkov, G. Malpuech, G. Baldassarri Höger von Högersthal, E. Feltin, J.-F. Carlin, and N. Grandjean. Spontaneous Polarization Buildup in a Room-Temperature Polariton Laser. *Physical Review Letters*, 101(13):136409, September 2008.

[195] H. Ohadi, E. Kammann, T. C. H. Liew, K. G. Lagoudakis, A. V. Kavokin, and P. G. Lagoudakis. Spontaneous Symmetry Breaking in a Polariton and Photon Laser. *Physical Review Letters*, 109(1):016404, July 2012.

[196] C. Ciuti, V. Savona, C. Piermarocchi, A. Quattropani, and P. Schwendimann. Role of the exchange of carriers in elastic exciton-exciton scattering in quantum wells. *Physical Review B*, 58(12):7926–7933, September 1998.

[197] Fabrice P. Laussy, Ivan A. Shelykh, Guillaume Malpuech, and Alexey Kavokin. Effects of Bose-Einstein condensation of exciton polaritons in microcavities on the polarization of emitted light. *Physical Review B*, 73(3):035315, January 2006.

[198] P. G. Savvidis, J. J. Baumberg, R. M. Stevenson, M. S. Skolnick, D. M. Whittaker, and J. S. Roberts. Angle-Resonant Stimulated Polariton Amplifier. *Physical Review Letters*, 84(7):1547–1550, February 2000.

[199] Axel Conrad, Tanja Hindrichs, Hussein Morsy, and Ingo Wegener. Solution of the knight's Hamiltonian path problem on chessboards. *Discrete Applied Mathematics*, 50(2):125–134, May 1994.